# Analysis Of Global Carbon Cycle Extremes, Their Compound Climate Drivers, And Implications For Terrestrial Carbon Cycle

A Dissertation Presented
by

**Bharat Sharma**

to

**The Department of Civil and Environmental Engineering**

in partial fulfillment of the requirements
for the degree of

**Doctor of Philosophy**

in

**Interdisciplinary Engineering**

**Northeastern University**
**Boston, Massachusetts**

September 2022

*To my family.*

# Contents

# List of Figures

# List of Tables

# List of Acronyms

**ESMs** Earth System Models

**GHGs** Greenhouse gases

**GPP** Gross Primary Productivity

**LULCC** Land Use and Land Cover Changes

**MAC** Modulated Annual Cycles

**NBP** Net Biospheric Productivity

**NEP** Net Ecosystem Productivity

**NPP** Net Primary Productivity

**PR** Precipitation

**RA** Autotrophic Respiration

**RH** Hetrothophic Respiration

**SM** Soil Moisture

**SSA** Singular Spectral Analysis

**TAS** Average Surface Temperature

**TCE** Time Continuous Extreme

**TER** Total Ecosystem Respirations

# Acknowledgments

I wish to thank those who have supported me during the various stages of my Ph.D. The support and courage I have received from my wife Pritika Sharma, my parents Nidhia Ram Sharma and Manju Sharma, and my brother Akshit Sharma has kept me going during the difficult times. I am extremely grateful to my Ph.D. advisor, Prof. Auroop R. Ganguly for the training and for providing me the platform to pursue an experiential Ph.D. at Oak Ridge National Laboratory (ORNL). I thank my Northeastern committee members Prof. Edward Beighley and Asst. Prof. Samuel Munoz for their valuable feedback.

I am extremely grateful to Dr. Forrest M. Hoffman and Dr. Jitendra Kumar from ORNL for their efforts and support during my internship GO! (Graduate Opportunities) program at ORNL. I would like to thank my fellow SDS lab members for their support: Ashis Kumar Pal, Jack Watson, Dr. Mary (Lizzy) Warner, Dr. Kate Duffy, Dr. Kevin Clark, Dr. Nishant Yadav, Puja Das, Dr. Thomas J. Vandal, and Dr. Udit Bhatia.

I would like to acknowledge the sponsors, Reducing Uncertainties in Biogeochemical Interactions through Synthesis and Computation (RUBISCO) Science Focus Area which is sponsored by the US Department of Energy Office of Science, Deans Fellowship (Northeastern University), and the US Department of Defense's Research Program, Strategic Environmental Research and Development Program (SERDP).

# Abstract of the Dissertation

## Analysis Of Global Carbon Cycle Extremes, Their Compound Climate Drivers, And Implications For Terrestrial Carbon Cycle

by
Bharat Sharma
Doctor of Philosophy in Computational and Earth System Sciences
Northeastern University, September 2022
Dr. Auroop R. Ganguly, Advisor

Human-induced fossil fuel emissions and land use and land cover change (LULCC), through biogeochemical and biogeophysical processes, alter the climate and modify carbon fluxes such as gross primary production (GPP) and net biospheric production (NBP). Rising surface temperatures - mainly driven by rising atmospheric carbon dioxide concentration - could lead to enhanced evaporation, reduced soil moisture availability, and more frequent droughts and heatwaves. The spatiotemporal co-occurrences of such events further drive extreme anomalies in vegetation productivity and net land carbon storage; thus, increasing the uncertainty of terrestrial ecosystems to act as a net carbon sink. In this dissertation, I quantify the carbon cycle extremes under climate and LULCC forcings, from 1850 to 2300, and attribute them to antecedent single and compound climate drivers at global, and regional scales. Earth System Models suggest that LULCC magnifies the intensity, frequency, and extent of carbon cycle extremes, resulting in a net reduction in expected photosynthetic activity by 10%. Under a business-as-usual carbon emissions scenario, about 70% of the regions will experience a growing number of negative extremes in NBP than positive NBP extremes toward the end of 2100. At high latitudes, the positive feedback of temperature and NBP weakens toward the end of the 21st century as the frequency of co-occurrences of high temperatures and negative NBP extremes increases. The disagreements in the characteristics of the interannual variability and extremes in GPP among observations and the models are significant and require an effort from the scientific community to address these uncertainties. More than half of total carbon cycle extremes are driven by the compound effect of dry, hot, and fire events. The single most dominant climate driver of carbon cycle extremes is soil moisture anomalies at both global and regional scales. Fire emerges as the second dominant driver. The number of temperature-driven extremes in the tropics significantly increases over time. Approaches developed in this dissertation

will help quantify extreme events in the dependent variables and their attribution to the interactive effect of multiple features at different spatio-temporal scales.

# Chapter 1

# Introduction

## 1.1 Motivation

Human activities are transforming the earth's atmosphere, ocean, and land surfaces at a scale and magnitude not previously seen during the past several thousand years of human history. The rising concentration of greenhouse gases (GHGs) such as water vapor, ozone, carbon dioxide, methane, and nitrous oxide are primary drivers of global warming and climate change. Carbon dioxide ($CO_2$), a major driver of climate change, comes mainly from the changes induced by land use and land cover changes (11% i.e. deforestation, increased agriculture, urbanization, etc.) and fossil fuel emissions (89%) [1, 2, 3]. $CO_2$ in the atmosphere directly impacts both vegetation dynamics and global warming, which in turn are interdependent and together influence planetary sustainability. Continued growth in the global population, drives the demand for fossil fuels, crops, and wood; which in turn has led to rise in carbon emissions and atmospheric $CO_2$ concentration over time. Terrestrial biosphere act as the largest sink of atmospheric carbon, absorbing about 30% of the global $CO_2$ emissions [1]. While terrestrial biosphere absorbs more carbon emissions than it releases into the atmosphere, there are large uncertainties about its ability to continue to act as major carbon sink in the future.

The changes in the terrestrial carbon cycle affects the climate through exchange of water, energy, mineral aerosols, $CO_2$, and other atmospheric gases [4, 5]. Dynamic terrestrial vegetation modify these exchanges and alter surface energy fluxes, hydrologic and biogeochemical cycles. Thus, changes in the land use and land cover (LULCC) through natural and human activities can alter the regional and global climate. LULCC also increases the interannual variability in the climate and carbon fluxes causing a further increase in the anomalous losses (and gains).

Any major climate perturbations or extreme events, such as droughts and heatwaves, have the potential to alter the strength of terrestrial carbon uptake and affect the total carbon budget [6]. Recent studies [7, 8, 9] have suggested that the frequency, intensity, and duration of climate extremes are projected to increase during the 21$^{st}$ century. For example, the 2003 drought and heatwave in Europe reduced plant productivity by 30% which was equivalent to four years of net carbon uptake of atmospheric $CO_2$ [10]. A recent study using the observationally-constrained and process-based model data [10] estimated an increase of about 10% in negative extremes in GPP during the period 2000–2016 compared to 1982–1998. These extremes were mainly due to warm droughts in particular over the northern temperate grasslands and croplands. These projected changes in climate extremes are consistent with observed trends. Such trends raise concerns of whether the structural and systematic changes in the climate-carbon feedback has already occurred at global and regional scales.

The terrestrial carbon cycle extremes can be better understood by detecting and analyzing the large anomalies in carbon fluxes (such as Gross Primary Productivity (GPP), Net Ecosystem Productivity (NEP), Net Biospheric Productivity (NBP), etc.) globally, Identification and attribution of associated anomalies in climate drivers and disturbance processes can provide further insights in the drivers of extremes in carbon cycle. The overarching goal of this dissertation research was to investigate the roles of anthropogenic emissions and land use change in modifying the frequency, intensity and the extent of terrestrial carbon cycle extremes. Chapters 2 through 4 address the following key questions:

- What was the impact of increasing anthropogenic $CO_2$ emissions on the anomalies in carbon cycle?
- What were the climatic drivers of large anomalous losses in terrestrial carbon uptake?
- How would land use and land cover change affect the climate drivers and carbon cycle (extremes) drivers in the terrestrial ecosystems?
- What were the (un)certainties in the quantification of characteristics of carbon cycle extremes and their drivers among Earth system models and observations?

The results from this research aim to inform the policymakers to take strong actions in the field of mitigation adaptation due to climate change, which was identified as the 3rd major risk according to the World Economic Forum Global Risk Survey (2017-18).

## 1.2 Climate-Carbon Cycle Feedbacks

The main determinant of the climate of the 21st century is the atmospheric $CO_2$ concentration [11]. Many studies have found that atmosphere–land and atmosphere–ocean fluxes of $CO_2$ are sensitive to climate [12, 13, 14]. Climate change is driven by rising atmospheric $CO_2$ concentration and climate change in turn is affected by $CO_2$; thus atmospheric $CO_2$ concentration, the climate, and the carbon cycle form a feedback loop [11]. Friedlingstein et al. (2006) quantified the effect of climate-induced changes in the global carbon budget due to an increase of atmospheric $CO_2$ as

$$\Delta {C^c}_A = \frac{1}{1-g} \Delta {C^u}_A \tag{1.1}$$

where $\Delta {C^c}_A$ is the change in atmospheric $CO_2$ in the coupled run, $\Delta {C^u}_A$ is the change in atmospheric $CO_2$ in the uncoupled run, and g is the gain of the climate-carbon feedback [15]. To isolate the influences of climate and $CO_2$ on land and ocean carbon uptake, Friedlingstein et al. 2003 defined the change in land and ocean carbon storage as

$$\Delta {C^c}_L = \beta_L \Delta {C^c}_A + \gamma_L \Delta T^c \tag{1.2}$$

$$\Delta {C^c}_O = \beta_O \Delta {C^c}_A + \gamma_O \Delta T^c \tag{1.3}$$

where $\Delta {C^c}_L$ and $\Delta {C^c}_O$ are the change in land and ocean carbon storage in the coupled simulations arising from an increase of $\Delta {C^c}_A$ atmospheric $CO_2$ concentration and $\Delta T^c$ increase in temperature. $\beta_L$ and $\beta_O$ are the land and ocean carbon sensitivity to atmospheric $CO_2$, $\gamma_L$ and $\gamma_O$ are the land and ocean carbon sensitivity to climate change. Therefore, the changes in same land and ocean carbon storage for uncoupled simulations are defined as

$$\Delta {C^u}_L = \beta_L \Delta {C^u}_A \tag{1.4}$$

$$\Delta {C^u}_O = \beta_O \Delta {C^u}_A \tag{1.5}$$

The effect of change in atmospheric $CO_2$ on global mean temperature can be approximated as

$$\Delta T^c = \alpha \Delta {C^c}_A \tag{1.6}$$

where $\alpha$ is the linear transient climate sensitivity to $CO_2$.

Using the equations 1.1, 1.2, 1.3, and 1.6, gain in climate-carbon feedback can be related to the sensitivity coefficients of land and ocean carbon cycle as

$$g = \frac{-\alpha(\gamma_L + \gamma_O)}{1 + \beta_L + \beta_O} \tag{1.7}$$

Hence, the gain of carbon cycle is larger for higher effective climate sensitivities and for more negative values of $\gamma_L$ and $\gamma_O$. Climate–carbon gain is weaker if land and ocean uptake positively respond to rising $CO_2$, i.e., for larger values of $\beta_L$ and $\beta_O$. This analysis neglects nonlinear aspects of climate-carbon feedback; however the insights from this insights are valuable to characterize model responses.

Friedlingstein et al. (2006) characterized these sensitivity parameters for 11 coupled climate-carbon cycle models for Coupled Climate-Carbon Cycle Model Intercomparison Project ($C^4$MIP). They found an unanimous agreement among the models that climate change will cause a decline in efficiency of the earth system to absorb perturbations in anthropogenic carbon. The higher atmospheric levels of $CO_2$ led to an additional climate warming. All models simulations suggested a negative sensitivity for the land and ocean carbon cycle to future climate.

## 1.3 Structure of the thesis

Table 1.1: Publications from this Dissertation.

| **Publications** | **Chapter** |
|---|---|
| Sharma, Bharat, Kumar, J., Collier, N., Ganguly, A. R., & Hoffman, F. M. (2022). Quantifying Carbon Cycle Extremes and Attributing Their Causes Under Climate and Land Use & Land Cover Change from 1850 to 2300. Journal of Geophysical Research: Biogeosciences, 127, e2021JG006738. https://doi.org/10.1029/2021JG006738 | Chapter 2 |
| Sharma, Bharat, Kumar, J., Ganguly, A. R., and Hoffman, F. M. , in review (2022)<br>Carbon Cycle Extremes Accelerate Weakening of the Land Carbon Sink in the Late 21st Century. Biogeosciences Discussions, preprint, https://doi.org/10.5194/bg-2022-178. | Chapter 3 |
| Sharma, Bharat, Kumar, J., Ganguly, A. R., and Hoffman, F. M. (2022).<br>Investigating Variability in the Intensity, Direction, and Spatial Distribution of Carbon Cycle Extremes and Attribution to Climate Drivers Using Observations and CMIP6 Earth System Models.<br>*Manuscript in Preparation* | Chapter 4 |

Chapter 1 presents the overarching motivation and objectives of the dissertation research and outlines the structure of the dissertation.

Chapter 2 presents the analysis of extremes in GPP fluxes from 1850 to 2300 under two simulated scenarios from CESM1BGC model. Both simulations were forced with historical, RCP8.5, and ECP8.5 trajectories of atmospheric $CO_2$ concentration. One model simulation was forced with dynamic Land Use and Land Cover Change (LULCC) scenario, while in the other the plant functional types were kept constant at 1850 levels. It defines the anomalies and extremes in carbon cycle fluxes and climate drivers. Chapter develops methodology to detect the anomalies and extremes in carbon cycle fluxes and climate drivers, define threshold trajectories and temporally continuous extreme (TCE) events. It also describes the methodology for attribution of individual and compound climate drivers of carbon cycle extremes. Chapter discusses the changing patterns of GPP extremes, interannual variability in GPP, and climate drivers including case studies for several regions in the Amazon. The climatic conditions that trigger an extreme event and conditions that cause persistent TCEs were also discussed.

Net Biospheric production (NBP), the total downward flux of carbon from the atmosphere to the land, represents the net carbon uptake after accounting for carbon losses from plant respiration, heterotrophic respiration, fire, and harvest [5] and is a critical measure of land carbon storage. Hence, NBP represents the changes in net carbon uptake and terrestrial carbon sink. Chapter 3 presents the global and regional analysis of extremes in NBP using the CMIP6 CESM2 simulation forced with historical and SSP585 scenario. Characteristics of carbon cycle extremes and their climate drivers were analyzed at regional scales across 26 regions across the globe. Chapter also presents discussions of patterns observed in temperature sensitivity and changes in carbon cycle extremes in carbon rich tropical and high latitude ecosystems that were expected to experience significant changes towards the end of the 21st century.

Chapter 4 leverages multiple observational datasets and multiple Earth System Models to present an intercomparison of the characteristics of GPP, interannual variability and extremes. These comparisons were performed at the global and regional scales.

# Chapter 2

# Quantifying Carbon Cycle Extremes and Attributing Their Causes Under Climate and Land Use & Land Cover Change from 1850 to 2300

## 2.1 Introduction

Human activities are altering the Earth's atmosphere, ocean, and land surfaces at a scale and magnitude not seen throughout the past multiple thousands of years. The rising concentration of greenhouse gases (GHGs) such as water vapor, ozone, carbon dioxide, methane, and nitrous oxide are primary drivers of global warming and climate change. As a result of continued growth in the global population, the demand for fossil fuels, crops, and wood is increasing. Enhanced emissions through use of fossil fuels [3] and land use and land cover change (LULCC) increases the atmospheric concentration of carbon dioxide ($CO_2$). Rising $CO_2$ emissions have led to increased climate variability and frequency of climate extremes, which have a large impact on terrestrial gross primary productivity (GPP) and GPP extremes [16, 17, 6, 18, 19, 20]. While climate extremes are relatively easy to measure, their impact on terrestrial vegetation is less detectable [21]. Since terrestrial ecosystems absorb a quarter of anthropogenic $CO_2$ emissions [3], large changes in vegetation productivity could alter the global carbon budget. Hence, it is crucial to investigate extreme anomalies in terrestrial carbon cycle and estimate their impacts on the terrestrial carbon sink under rising $CO_2$ emissions and

LULCC scenarios.

Prior studies [22, 6, 5] have found that the combined effect of $CO_2$ fertilization, increasing temperature, nitrogen deposition, and lengthening of growing seasons lead to increased vegetation productivity and strengthening of carbon sinks with a negative feedback to climate change. However, coupled carbon-climate models have large uncertainties in future projections of ecosystem responses and feedback strength [23, 6, 18, 19]. Hoffman et al. (2014) [23] found persistent atmospheric $CO_2$ biases in Coupled Model Intercomparison Project 5 (CMIP5) models because of uncertainties in biological and physical processes related to carbon accumulation. While most Earth system model-based climate change studies analyze projections till year 2100, these projections may miss physical-biogeochemical feedbacks that arise later from the cumulative effects of climate warming [24]. The negative sensitivity of terrestrial carbon cycle to rising temperature will likely have increasing adverse implications on carbon cycle extremes over time [25, 18]. Understanding the direction and strength of these feedbacks is essential for estimating long-term $CO_2$ concentrations and predicting and mitigating the impact and extent of climate change. These limitations could alter the assessment of the rate of increase of atmospheric $CO_2$ and intensity of associated feedbacks with the terrestrial biosphere.

While the effects of increased warming due to greenhouse gases are spatially extensive, the LULCC effects are more regional [26]. The land-use history reconstruction used in this study estimated the proportion of land surface impacted by human activities to be 60% of total vegetated area, mainly due to conversions from primary vegetation to managed vegetation by 2100 [27]. The conversion of land from natural to managed ecosystems reduces the carbon sink and its capacity to uptake anthropogenic $CO_2$ and influences climate by modifying biogeophysical and biogeochemical processes [4]. Changes in the plant functional type (PFT) at any grid cell modifies the distribution of above and below ground carbon [28], response to light and energy [29], distribution of soil organic matter and nutrients [30]. Human activities, such as the conversion of forests and grasslands to agricultural land and urbanization, alter net radiation, sensible and latent heat partitioning, biogeochemical cycles, and the hydrologic cycle. Reduction of temperate vegetation cover by deforestation increases the albedo of the surface which decreases the net radiation that drives surface cooling and reduces evapotranspiration that may result in declines in precipitation; but tropical deforestation for pastures decreases the total atmospheric column heating and atmospheric vertical motion which leads to a warmer and drier climate [4, 5]. Since interannual variability (IAV) in GPP is strongly influenced by interannual variations in radiation, temperature, and precipitation [19], the impact of LULCC in addition to $CO_2$ on carbon cycle extremes will likely increase over time.

Recent studies have investigated the characteristics of extreme anomalies in GPP due to climate change until the year 2100 [21, 18, 31, 6] and a few concluded that losses in carbon uptake due to negative extremes in GPP are compensated by increased $CO_2$ fertilization [21, 6]. However, to our knowledge, no study has examined the extreme anomalies in carbon cycle beyond 2100 and the role of human LULCC in modifying carbon cycle extremes.

Rising $CO_2$ and LULCC impact many components of the terrestrial carbon cycle, such as total ecosystem carbon, net biome productivity, net ecosystem productivity, net primary productivity, and GPP. The overarching goal of this study is to investigate the role of $CO_2$ and LULCC in modifying the characteristics of extremes in GPP, referred to as carbon cycle extremes in this paper, and attribute changes to individual and compound effects of climate drivers. We hypothesize that 1) rising $CO_2$ emissions will lead to larger increases in the intensity, frequency and duration of negative carbon cycle extremes than positive extremes; and 2) LULCC activities in addition to $CO_2$ emissions will further increase GPP interannual variability and magnitude of carbon cycle extremes though total GPP will reduce. We performed analysis to 1) examine the magnitude, duration, frequency and spatial distribution of negative and positive carbon cycle extremes; 2) investigate the lagged response of antecedent climate drivers (and their compound effect) that drive carbon cycle extremes; 3) analyze the climate conditions that trigger long duration temporally continuous extremes; and 4) inspect regional changes in climate-carbon feedbacks for the Central and South American tropics.

## 2.2 Data

We used simulations of the Community Earth System Model (version 1) with biogeochemistry enabled, CESM1(BGC), at approximately $1^\circ \times 1^\circ$ resolution to analyze climate-driven extreme anomalies in total photosynthetic activity. CESM1(BGC) is a fully coupled global climate model composed of land, atmosphere, and ocean components [32, 33]. The atmospheric $CO_2$ forcing time series consisted of the historical (1850–2005), Representative Concentration Pathway 8.5 (RCP 8.5; 2006–2100), and Extended Concentration Pathway (ECP 8.5; 2101–2300) mole fractions, which increased from 285 ppm in 1850 to 1962 ppm in 2300 (Figure 2.1(a)). Analysis of the Coupled Model Intercomparison Project 5 (CMIP5) models using the International Land Model Benchmarking (ILAMB) [34] show (Table A1) that CESM1(BGC) is one of the best performing model in terms of overall and IAV benchmark scores when compared to observational benchmarks.

We analyzed terrestrial carbon cycle extremes (or GPP extremes) using two simulations, namely, *with* and *without LULCC*. In the simulation *without LULCC*, the land cover was fixed at pre-industrial (year 1850) values. In the *with LULCC* simulation, transient land cover was prescribed over the historical and RCP 8.5 period (1850–2100) ([27]) and consists of the prescribed spatial distribution of PFTs ([33]). Land-use conversion is assumed to stop at the year 2100, and the distribution of PFTs remains constant at year 2100 level for the period 2100 – 2300, while wood harvest is maintained at a constant rate over that period [35]. The reactive nitrogen deposition followed the spatially variable time series from 1850 to 2100 [36] and was subsequently held constant from 2100 to 2300. Biogeochemical processes on land and in the ocean respond to the historical and prescribed RCP 8.5 and ECP 8.5 atmospheric $CO_2$ concentration forcing (Figure 2.1(a)). Increasing $CO_2$ fertilization, water-use efficiency, and lengthening of growing seasons enhance total photosynthesis and gross primary production (GPP). These processes will be further altered by the changes in PFT distribution under *with LULCC*. Figure 2.1(c) shows the 5 year moving average of global annually integrated GPP for simulations *with* and *without LULCC*, both forced with the same atmospheric $CO_2$ concentration trajectory (Figure 2.1(a)). The magnitude of the average GPP *with LULCC* is less than the average GPP *without LULCC* potentially due to the conversion of primary vegetation to managed vegetation.

## 2.3 Methods

A significant deviation from the mean value is called an extreme. Extreme events in GPP signify large variations in photosynthetic activity, with positive extremes representing increases in carbon uptake, while negative extremes being indicative of loss of carbon uptake [21]. While extremes in climate have been extensively studied [6, 37, 38, 18, 31], few studies have focused on extremes in GPP and their underlying drivers [21, 39, 31]. In this study, we identify extremes in global carbon uptake by computing percentile-based thresholds [40]. Described in detail in Section 4.2.3, a positive (or negative) extreme in GPP is defined as anomalies in GPP that are greater (or less) than a selected percentile-based threshold of GPP anomalies. The thresholds were computed by selecting $1^{st}$ and $99^{th}$ percentile anomalies in GPP, calculated at every land grid cell for each consecutive 25 years from the year 1850 through 2300. The GPP extreme events are then defined as values of GPP anomalies above $q$ (positive extremes) or below $-q$ (negative extremes). The schematic Figure 2.2 illustrates the steps to compute GPP extremes.

Extremes in GPP could also be categorized as isolated vs temporally continuous extreme events. The isolated and temporally continuous extremes in GPP are analogous to hot days and heatwaves. Extreme events in GPP that are continuous in time represent a significant cumulative

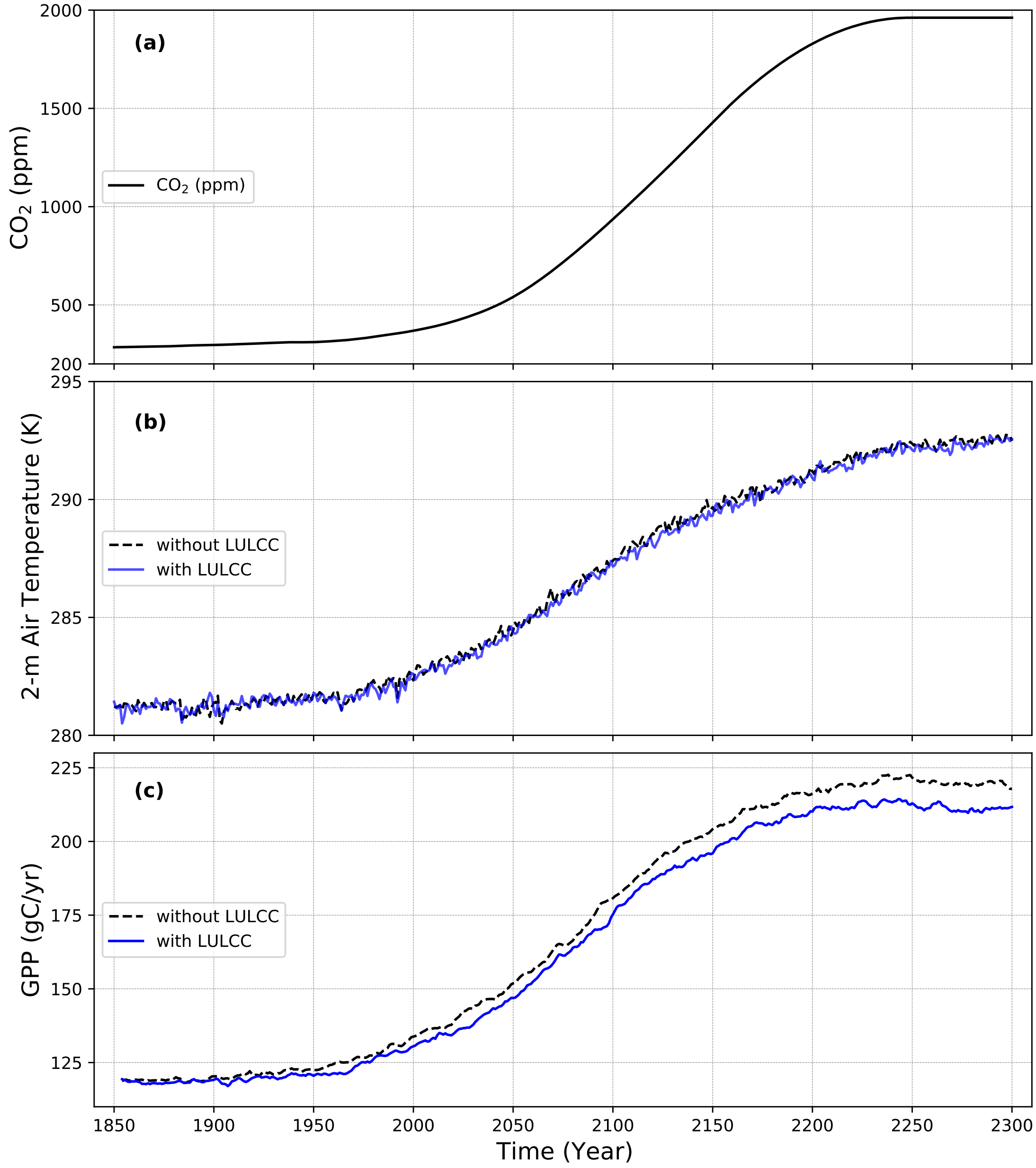

Figure 2.1: The (a) prescribed trajectory for atmospheric carbon dioxide ($CO_2$) forcing, (b) 5-year running mean of annual 2 m air temperature, and (c) 5-year running mean of total annual gross primary production (GPP) for the historical, RCP 8.5 and ECP 8.5 simulations.

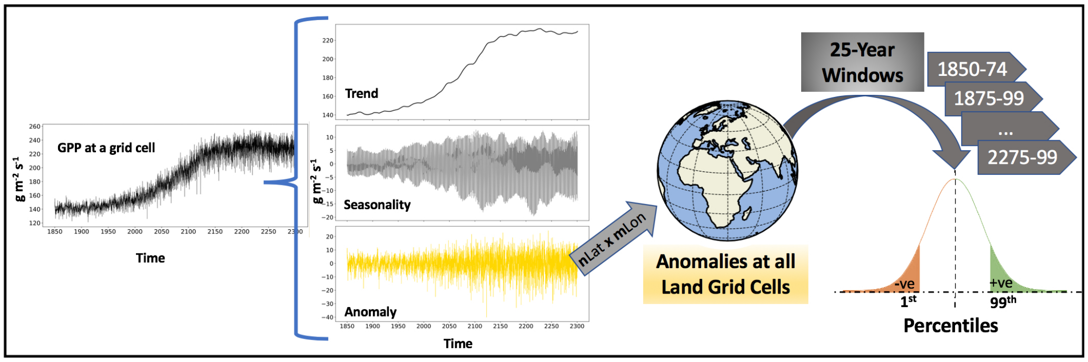

Figure 2.2: Schematic diagram for calculating thresholds in gross primary production (GPP). The anomalies are calculated at every grid cell by subtracting the nonlinear trend and modulated annual cycle from the GPP time series. The anomalies of every land grid cell ($nLat \times nLon$) for consecutive 25 year time windows were chosen to calculate probability distribution function of GPP anomalies. The 1st and 99th percentile values represent the global GPP threshold values for negative and positive extremes in GPP.

impact on carbon uptake. Akin to the definition of temporally continuous heatwaves by [41], we define a temporally continuous extreme (TCE) event (Figure A1) in GPP as (a) three or longer months (equal to a season length) of GPP extreme anomaly occurring consecutively, (b) and are considered as single continuous event through any gaps of two months or shorter in duration (assuming that ecological recovery is unlikely in less than a season) beyond three months. A GPP TCE event that occur after a season, i.e., three months or more, is considered a separated TCE. Section 4.2.4 illustrates the method for attribution of GPP TCEs to individual and compound effects of climate drivers.

### 2.3.1 Identification and Detection of GPP Extreme Events

The time series of GPP at any grid cell consists of a trend, seasonality, and anomalies (Figure 2.2) components. We used singular spectrum analysis (SSA), a non-parametric spectral estimation method based on embedding a time series in vector space [42], to extract signals with specific frequencies. The trend in GPP at any grid cell captures long term change in mean GPP, which is influenced by long term changes in climate drivers, atmospheric $CO_2$ concentration, and LULCC. Since El Niño-Southern Oscillation (ENSO), and to a lesser extent other large-scale drivers of climate variability, enhance the variability in terrestrial photosynthesis, the nonlinear trend at each grid cell was calculated by adding all the frequencies of 10 years and longer. Hence, carbon cycle extremes in our study include the GPP anomalies induced by ENSO which is one of the largest modes of climate variability and peaks about every three to seven years [43] and exerts strong regional effects on the terrestrial carbon cycle [44]. The seasonality in GPP follows a periodic cycle of 12 months. The conventional way to compute the annual cycle is to determine the mean climatology over a period, however, the climatology does not reflect the intrinsic nonlinearity of the climate-carbon feedback, especially under external forcing [45] because of the increased modulation of the annual cycle in GPP under business-as-usual rising $CO_2$ emissions. We calculated the modulated annual cycle, which allows the annual cycle to change from year to year and consists of signals with a frequency of 12 months and its harmonics. The anomalies at each grid cell were calculated by subtracting the trend and modulated annual cycle from the GPP time series (Figure 2.2). Hence, GPP anomalies comprised of the high-frequency signals ($<$12 months) and the interannual variability ($>$12 months and $<$10 years). We examined the probability distribution function (PDF) of GPP anomalies for all land grid cells for every 25-year time window from 1850 through 2300. While the left tail of the PDF of GPP anomalies represents large losses in carbon uptake, the right tail portrays large gains in carbon uptake. We chose the $1^{\text{st}}$ and $99^{\text{th}}$ percentile of all GPP anomalies as thresholds in the 25-year time windows to identify large losses and gains in carbon uptake.

The percentile-based thresholds ($1^{\text{st}}$ and $99^{\text{th}}$) for every 25-year time window yield the negative ($Th-$) and positive ($Th+$) threshold trajectories of GPP anomalies. The extreme anomalies in GPP range from 425 GgC/month for the period 1850–74 to 840 GgC/month for 2275–99, as shown in Figure 2.3. Since GPP anomalies are a subset of GPP, increasing $CO_2$ fertilization, water use efficiency, and lengthening of growing season lead to increases in GPP (Figure 2.1(c)) and the thresholds of GPP anomalies. The simulations *with* and *without LULCC*, show higher magnitudes of $Th-$ than $Th+$, indicating that negative anomalies in GPP are stronger than positive for the same percentile. Also, the values of the thresholds for simulation *with LULCC* were higher than *without LULCC*. To enable the comparison of simulations *with* and *without LULCC*, we selected one threshold trajectory, *without LULCC* $TH+$ ($q$), to apply for calculations of all positive and negative extremes in the current study. Thus, the positive GPP extremes are defined as GPP anomalies greater than $q$ and negative GPP extremes are the GPP anomalies less than $-q$ for both simulations, *with* and *without LULCC*.

Integral of negative (or positive) GPP extremes over land grid cells represents the total global loss (or gain) in carbon uptake per month. The time series of frequency and extent (area) under GPP extremes was computed by integrating the count and area of grid cells under GPP extremes.

Table 2.1: Climate Drivers Considered for Attribution to GPP Extremes

| Symbol | Units | Description |
|---|---|---|
| $Prcp$ | mm $s^{-1}$ | Atmospheric rain + snow |
| $P{-}ET$ | mm $s^{-1}$ | Precipitation minus Evapotranspiration |
| $Soilmoist$ | mm | Soil moisture in top 1-m depth |
| $T_{\mathrm{max}}$ | K | Monthly maximum daily temperature |
| $T_{\mathrm{sa}}$ | K | Monthly mean daily temperature |
| $T_{\mathrm{min}}$ | K | Monthly minimum daily temperature |
| $Fire$ | gC $m^{-2}$ $s^{-1}$ | Total column level carbon loss due to fire |

### 2.3.2 Attribution to Climate Drivers

Human activities, through fossil fuel emissions and land cover changes, modify the climate and climate-carbon feedbacks. To attribute significant changes in carbon uptake and GPP to climate drivers, we computed linear regression of temporally continuous GPP extremes with anomalies in atmospheric precipitation ($Prcp$, composed of atmospheric rain and snow), precipitation minus evapotranspiration ($P - ET$), soil moisture ($Soilmoist$, up to 1-m depth), monthly maximum daily temperature ($T_{\mathrm{max}}$), monthly minimum daily temperature ($T_{\mathrm{min}}$), monthly mean daily temperature ($T_{\mathrm{sa}}$), and fire ($Fire$, total column level carbon loss due to fire) (Table 2.1).

The impact of climate drivers on GPP often has a lagged response because the terrestrial ecosystem has ingrained plasticity to buffer and push back effects of climate change [46]. The controls of different climate drivers on GPP and its extremes is also dependent on location, timing, soil type and moisture, and vulnerability of land cover type [18]. Therefore, at every location of GPP TCEs, we used linear regression to compute the correlation of TCEs with the cumulative lagged response of anomalies of every climate driver at time-lags of 0 to 12 months, for every 25 year time window from 1850 to 2300. However, lagged responses beyond four months were insignificant and thus we only report on one, two, and three lags. Anomalies from past months were included in the computation of lagged correlations. For instance, to compute a climate-carbon lag response of 3 months, the GPP extreme anomalies at month $t$ were correlated with the average of climate driver anomalies at $t - 3$, $t - 2$, and $t - 1$ months. We also investigated the GPP TCEs driven by triggers (climate drivers during onset of TCEs) and persistent climate drivers (considering entire duration of TCEs). We identified the most dominant climate driver at any grid cell under simulations *with* and *without LULCC*, as the climate driver with the highest absolute correlation coefficient (significance value, $p < 0.05$). The percent global distributions of dominant drivers for every time window were computed to inspect the changing patterns of dominant drivers at various lags and over time.

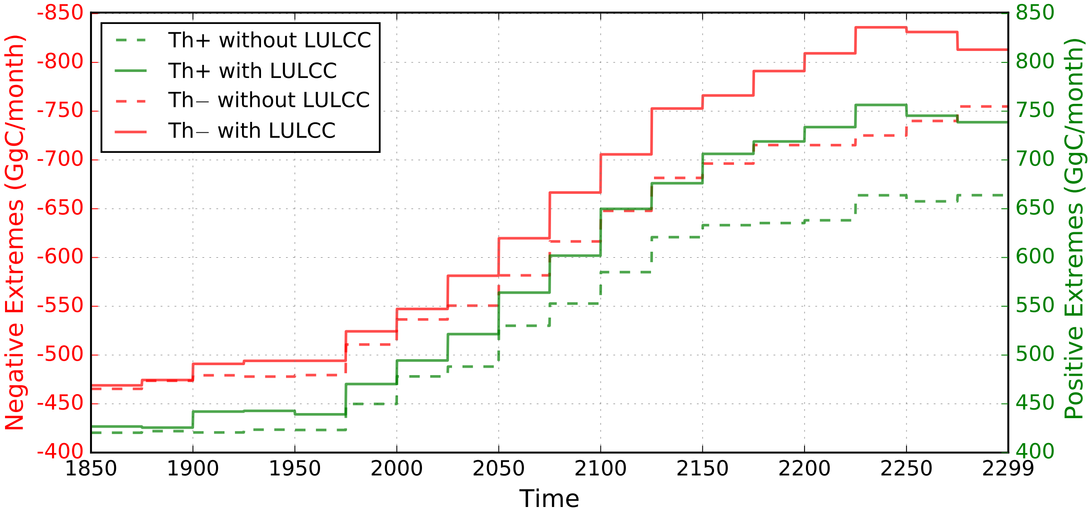

Figure 2.3: Thresholds of GPP extreme events with and without LULCC from 1850–2299. The figure shows increasing thresholds of positive and negative GPP extreme events based on 99th and 1st percentile. The percentiles are calculated for global GPP anomalies for every time window (of 25 years) from 1850–2299. The red color represents negative thresholds or Th− and green represents Th+. The solid and dashed lines represent the simulations with and without LULCC respectively.

A GPP TCE event could be driven by one or a combination of climate drivers. The study of compound events consisting of multiple different climate drivers leading to a GPP extreme improves our understanding of interactive effects of climate drivers [47]. While the climate extremes and carbon extremes often do not occur concurrently, the compound effects of climate drivers that are not climate extremes can nevertheless impact the carbon cycle [48]. We studied the compound effects of water ($Prcp$, $P - ET$, and $Soilmoist$)-, temperature ($T_{\max}$, $T_{\mathrm{sa}}$, and $T_{\min}$)- and fire ($Fire$)-driven TCEs in GPP.

## 2.4 Results

### 2.4.1 Detection and Identification of GPP Extremes

The 1$^{\mathrm{st}}$ and 99$^{\mathrm{th}}$ percentiles of the PDF of GPP anomalies for all land grid cells in 25-year time windows were used to compute the threshold trajectories for*with* and *without LULCC* simulations. Figure 2.3 shows trajectories of positive and negative GPP extremes for simulations *with* and *without LULCC*. The rising atmospheric $CO_2$ concentrations and increasing $CO_2$ fertilization, water use efficiency and lengthening of growing seasons [5, 33] lead to an increase in the global GPP and GPP anomalies. Consequently, $Th+$ and $Th-$ increased in both simulations; for the simulation *without LULCC* $Th+$ increased from 420 GgC/month during 1850–1874 to 664 GgC/month during 2275–2299; the corresponding values for $Th+$ *with LULCC* were 426 and 739 GgC/month, for $Th-$ *without LULCC* were $-465$ and $-755$ GgC/month, and for $Th-$ *with LULCC* were $-469$ and $-813$ GgC/month. The increasing magnitude of thresholds for GPP extremes over time highlights the intensification of GPP extremes over time. For the same percentile, the magnitude of negative thresholds were larger compared to positive thresholds. Hence, negative anomalies in GPP or losses in carbon uptake were much larger than gains in carbon uptake, primarily due to negative impact of increasing anthropogenic $CO_2$ and LULCC on carbon cycle anomalies. Higher thresholds for the simulation *with LULCC* despite lower GPP (Figure 2.1(c)) compared to the simulation *without LULCC*, highlights that increasing magnitude of GPP anomalies were likely due to LULCC and wood harvest. Higher anomalies GPP is potentially due to large reductions in the area of tree PFTs of primary vegetation (forests) in the RCP 8.5 LULCC scenario, $-3.5 \times 10^6$ km$^2$ from 1850 to 2100. The decrease in primary vegetation is associated with large increases in crop and grass areas, leading to a reduction of ecosystem carbon of $-49$ PgC from 1850 to 2100. The global wood harvest carbon flux increased to 4.2 PgC year$^{-1}$ [33] in the year 2100, and then was kept at a constant harvest rate from 2100 to 2300. The legacy effects of human land cover change and continued wood harvest becomes more visible beyond 2100 when the difference in annual GPP of both simulations widens (Figure 2.1(c)). As a result of enhanced variability in GPP *with LULCC*, we saw a larger magnitude of negative and positive thresholds for the simulation *with LULCC* (Figure 2.3).

The global time series of the intensity of losses and gains in carbon uptake, calculated by integrating negative and positive extremes in GPP, are shown in Figures 2.4(a) and 2.4(b) for simulations *without* and *with LULCC*, respectively. Compared to the simulation *without LULCC*, the total additional loss of global carbon uptake due to LULCC was $-46.53$ PgC for period 1850–2100 and $-141.76$ PgC for 2101–2300. The respective difference in total global GPP (*with LULCC* minus *without LULCC*) was $-676$ PgC for 1850–2100 and $-1416$ PgC for 2101–2300; and relative to the total global GPP, the additional losses in total carbon uptake due to LULCC increased from 6.9% (1850–2100) to 10% (2100–2300). Hence, LULCC impacts global carbon cycle by reducing the total global GPP and increasing losses in carbon uptake during GPP extremes. The rates of increase in the intensity of positive extremes in GPP for the simulation *without LULCC* were 529 and 377 MgC/month for the periods 1850–2100 and 2101–2299, respectively, and for the simulation *with LULCC* were 863 and 692 MgC/month, respectively. The corresponding rates

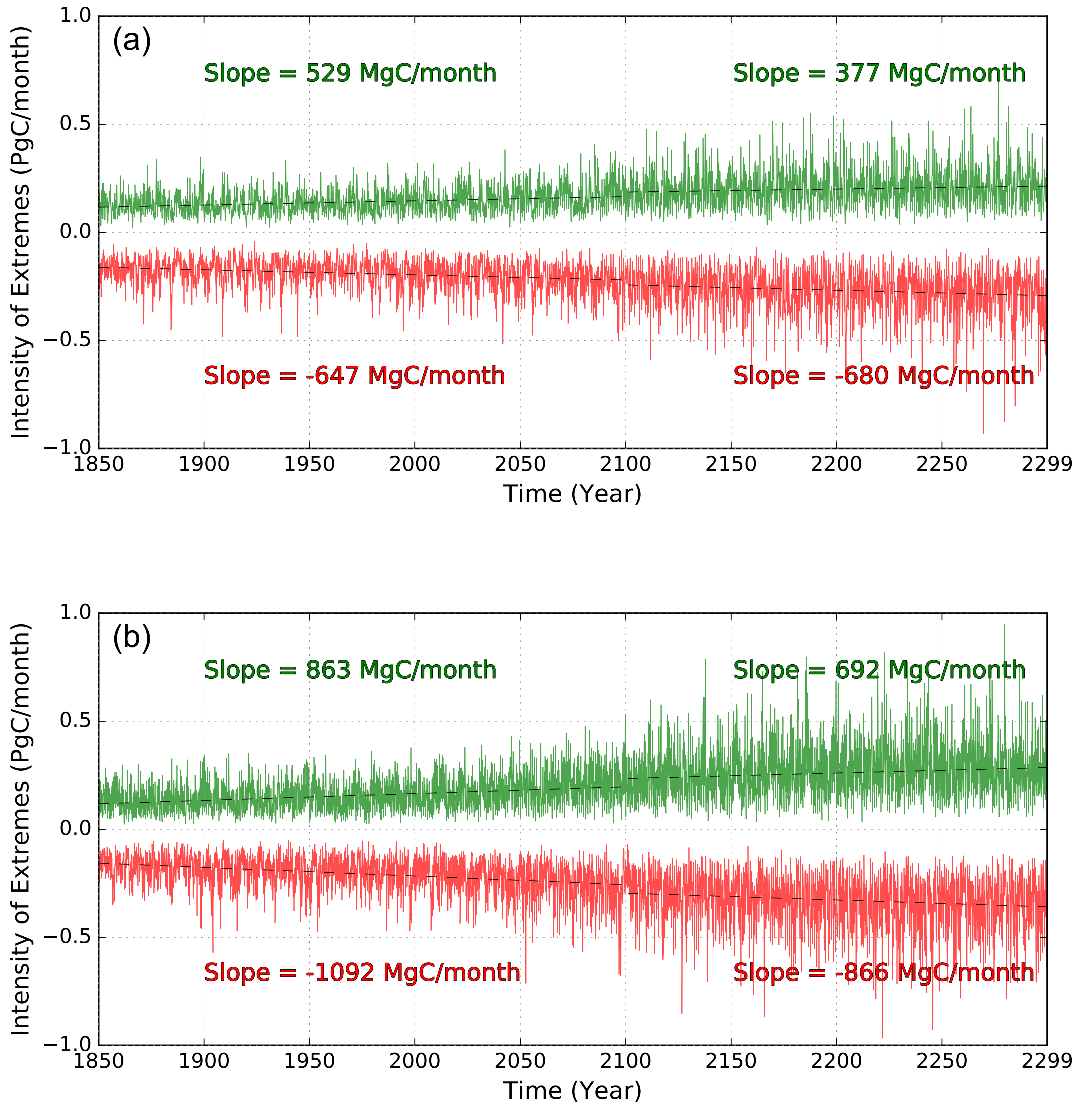

Figure 2.4: Monthly time series of intensity of global GPP extreme events for the simulation without LULCC (a) and with LULCC (b) from 1850–2299. The positive GPP extremes, GPP anomalies $> q$, are represented in green color and the negative extremes, GPP anomalies $< -q$, are shown in red color. The rate of increase of positive GPP extremes without LULCC are 529 MgC/month from 1850–2099 and 377 MgC/month from 2100–2299 (a). The corresponding rates for the growth of negative extremes are $-647$ MgC/month and $-680$ MgC (a). The rate of increase of positive GPP extremes with LULCC are 863 MgC/month from 1850–2099 and 692 MgC/month from 2100–2299 (b). The corresponding rates for the growth of negative extremes are $-1092$ MgC/month and $-866$ MgC (b).

of increase in the intensity of negative extremes in GPP for the simulation *without LULCC* were $-647$ and $-680$ MgC/month, respectively, and for the simulation *with LULCC* were $-1092$ and $-866$ MgC/month, respectively. The changes in the rates of the intensity of positive extremes in GPP for the simulation *with LULCC* were analogous to the simulation *without LULCC*. However, the intensity of negative extremes in GPP for the simulation *with LULCC* shows a decrease beyond 2100, possibly due to non-increment of wood harvest rate and a constant PFT distribution at the year 2100 values for the period from 2100 through 2300 which decreases the relative variability in GPP after 2100. The larger intensity of negative extremes in GPP for the simulation *with LULCC* than *without LULCC* could result from increased wood harvest and land conversions to agriculture, pastures, and urban areas. The rate of increase in the intensity of positive extremes in GPP was higher in the simulation *with LULCC* than *without LULCC* probably due to large re-growth of secondary forests in the regions of the Eastern U.S., Europe, Africa, and South America [27]. In the simulation *with LULCC*, by the year 2100 under RCP 8.5, the LULCC transitions resulted in high-density croplands in the U.S., Europe, and South East Asia; high-density pastures in the Western U.S., Eurasia, South Africa, and Australia [27]. Primary forests were present in high northern latitudes and parts of Amazonia. Hence, LULCC forcing coupled with $CO_2$ forcing under RCP 8.5 and ECP 8.5 intensified both losses and gains in carbon uptake during extremes in GPP, with net losses in carbon uptake dominating the net climate-carbon response.

The rate of increase of intensities of positive and negative extremes in GPP was stronger for the simulation *with LULCC*, although the total GPP was less than the simulation *without LULCC* (Figure 2.1(c)). Stronger intensities of GPP extremes *with LULCC* were due to the larger interannual variability (IAV) in GPP *with LULCC* compared to *without LULCC* (Figure 2.5). LULCC alters the climate by modifying the biogeochemical and biogeophysical processes, which further affects the carbon cycle. For example, in semiarid climates, loss of vegetation cover increases the surface albedo, which increases the reflected solar radiation and cools the surface climate that weakens the boundary layer, reducing the probability of precipitation that creates the dry climate and reduces plant productivity. Biogeochemical processes include uptake of carbon during photosynthesis at an increased atmospheric concentration of $CO_2$ and loss of carbon during respiration in a warmer climate. Biogeophysical and biogeochemical processes do not occur in isolation and depend on the hydrologic cycle [5]. With increases in atmospheric $CO_2$ concentration, the climate becomes warmer and increases the intensity of precipitation and accompanying precipitation extremes [38, 49]. Clearing of land and deforestation has led to and will lead to cooling in high latitudes, warming in tropics, and uncertain changes in mid-latitudes [50]. As a result, human LULCC increases the

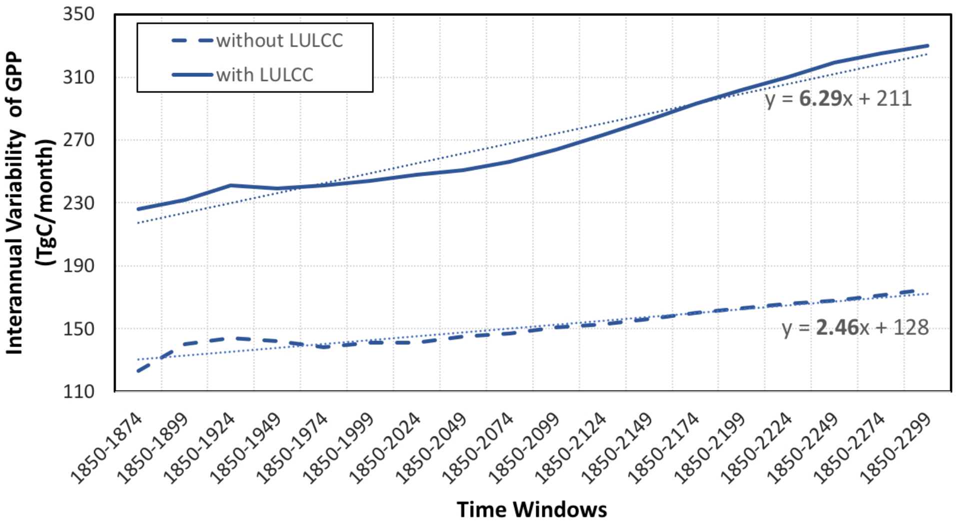

Figure 2.5: Global interannual variability (IAV) of GPP with and without LULCC. The unit of IAV is $10^{12}$ gC. The IAV is calculated from 1850 as the base year to 25 year increments, as shown on the $x$-axis. The solid line represents the IAV of GPP with LULCC and dashed line represents the IAV without LULCC. The linear fits represented by dotted lines show rates of increase of IAV of GPP with LULCC, which is higher by a factor of 2.5 compared to the simulation without LULCC.

regional heterogeneity in vegetation that alters the climate drivers [19], further increasing the global interannual variability and anomalies of GPP as well as the spatially heterogeneous distribution of GPP extremes. Therefore, the effect of both $CO_2$ and LULCC forcing, represented in *with LULCC*, increases the variability of biogeochemical and biogeophysical feedbacks, thus resulting in increased IAV of GPP in *with LULCC* than *without LULCC*.

The regional atmospheric circulation and climate change lead to spatial variations in the distribution of GPP extremes and the intensities of GPP extremes. Since the definition of GPP extremes is based on the threshold trajectory of $1^{st}$ percentile global anomalies of GPP for consecutive 25-year time windows in the simulation *without LULCC* (Figure 2.3), the total number of grid cells under positive GPP extremes were constant at around 64,000 (for every 25-year time windows) while they vary for all other scenarios. The total number of grid cells and area affected by negative extremes in GPP for the simulation *with LULCC* were largest, possibly because of increased negative feedback of climate variability on the carbon cycle due to the cumulative $CO_2$ and LULCC forcing. Relative to the frequency of positive extremes in GPP for the year 1850 (*without LULCC*), the frequency of positive extremes (*with LULCC*) increased by 17% and 28% for the periods 1850–2100 and 2101–2300 respectively; and the respective growth rates of negative extremes (*with LULCC*) were 13% and 19%. For *with LULCC*, growth rates for the area affected by positive GPP extremes were 16% and 28%, and for negative GPP extremes at 12% and 20% during 1850–2100 and 2101–2300 respectively. Higher growth rates of frequency and area-affected by positive extremes in GPP were probably due to increases in secondary forest cover; however the losses in the expected carbon uptake due to LULCC were larger than gains.

### 2.4.2 Attribution to Climate Drivers

The attribution of climate-driven extremes in GPP were performed for GPP TCE events, which are time-continuous GPP extremes meeting the criteria described in section 3.2. Variability in terrestrial carbon cycle intensified the climate-driven GPP TCEs under the combined forcing of human-induced LULCC and anthropogenic $CO_2$ emissions. The mean duration (Figure 2.6(a)) and standard deviation (Figure A2) of negative and positive TCEs in GPP for the simulation *with LULCC* were greater than the simulation *without LULCC*. In addition, the duration of TCEs lengthened over time, with more long-duration TCEs and fewer short-duration TCEs as time progressed. Figure 2.6(b) shows the density plot of the count of negative TCEs in GPP vs. the total duration of GPP TCEs in 25-year windows for the simulation *with LULCC*. The increasing mean duration of the negative

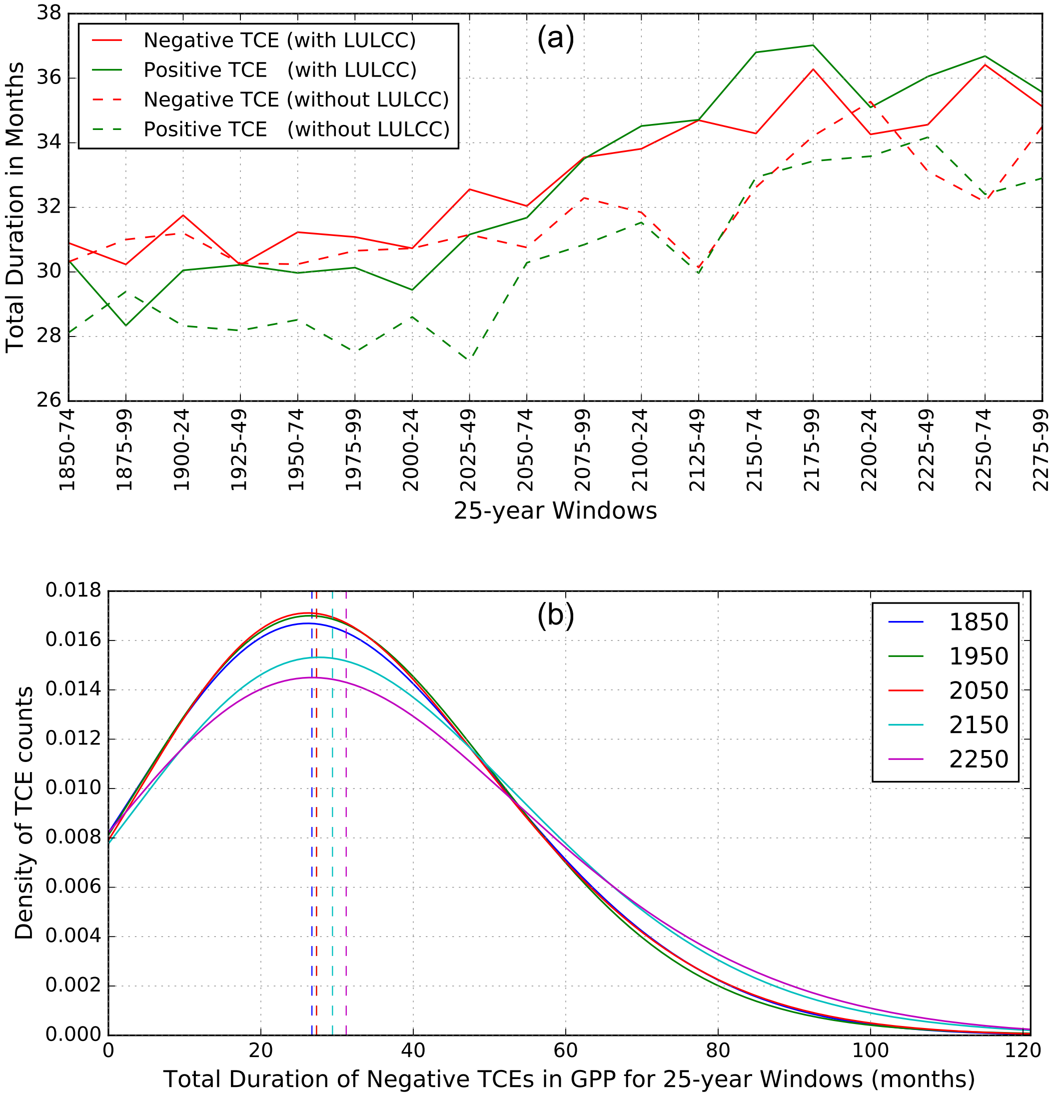

Figure 2.6: The mean duration of positive (shown in green) and negative (shown in red) TCEs for both the simulations, with (solid lines) and without (dashed lines) LULCC, for 25-year periods (a). The probability density of counts of total number of months under a negative TCEs in 25 years or 300 months (as shown in $x$-axis) for 25-year windows starting at the years 1850, 1950, 2050, 2150 and 2250 with LULCC (b). The dashed vertical lines shows the shifting of mean duration of negative TCEs to right, highlighting that the TCEs are getting longer over time.

TCEs in GPP in the future likely causes a larger reduction in the carbon uptake, which has significant implications for carbon storage and the carbon budget, and it can negate the positive feedback of increasing $CO_2$ fertilization under RCP 8.5 and ECP 8.5 $CO_2$ scenarios.

Extremes in carbon cycle and climate extremes often do not occur simultaneously [48]. In this study, we first detect temporally continuous extremes (TCEs) in GPP and then attribute the climate drivers using linear regression. Pearson's correlation coefficients and corresponding significance values ($p$-values) were computed between every climate driver and extreme anomalies in GPP during TCEs. The dominant climate driver at every land grid cell was defined by the maximum absolute correlation coefficient of climate drivers ($p < 0.05$). To consider the response of the ecosystem to prevailing climatic conditions, linear regressions were performed at multiple lags between extreme anomalies in GPP and climate driver anomalies. Figure 2.7 (and Figure A3) show the percent distribution of dominant climate drivers for every 25-year time window for both simulations, *with LULCC* and *without LULCC*, respectively, at lags of 1, 2, and 3 months. The relationship of water availability (soil moisture) with TCEs in GPP was globally dominant during most time windows (Figure 2.7). Reduction in soil moisture leads to an anomalous reduction in photosynthesis [18]. Soil moisture is the most dominant driver of negative carbon cycle extremes, highlighting a strong positive correlation of plant productivity with soil moisture, as shown in Figure A4(b). Temperature ($T_{\max}$ and $T_{\text{sa}}$) and $Fire$ have a negative correlation with TCEs in GPP (spatial distribution shown in Figures A4(d) and A4(e)), where an anomalous increase in these drivers leads to loss in carbon uptake. $T_{\max}$ was dominant at a lag of 2 months through 2100, but $Fire$ shows dominance at higher lags, especially beyond 2100 in the simulation *without LULCC*. The percent count of dominant temperature drivers, $T_{\max}$ and $T_{\text{sa}}$, increased over time, especially after 2100. Hence, carbon extremes driven by hot conditions will have the largest increase in a warming climate, especially after 2100. The lagged response of anomalously hot air temperatures and lack of soil moisture creates hot and dry conditions suitable for fire events. Fire events driven by hot and dry conditions increase at a higher rate at all lags in the simulation *with LULCC* than the simulation *without LULCC*. After 2100 in the simulation *with LULCC*, fire stands out as the dominant driver at all lags, highlighting that the human-induced LULCC will make ecosystems more vulnerable to fire events. The results of our study are consistent with the findings of Williams et al. (2014) [51] and Zscheischler et al. (2014) [21], suggesting that the declines in GPP with warm temperature extremes are due to dependence of GPP on soil moisture, and to the strong negative correlation between soil moisture and temperature. The rising temperature under global warming will create a warmer environment in the future, increasing the risk associated with heatwaves and their impacts on

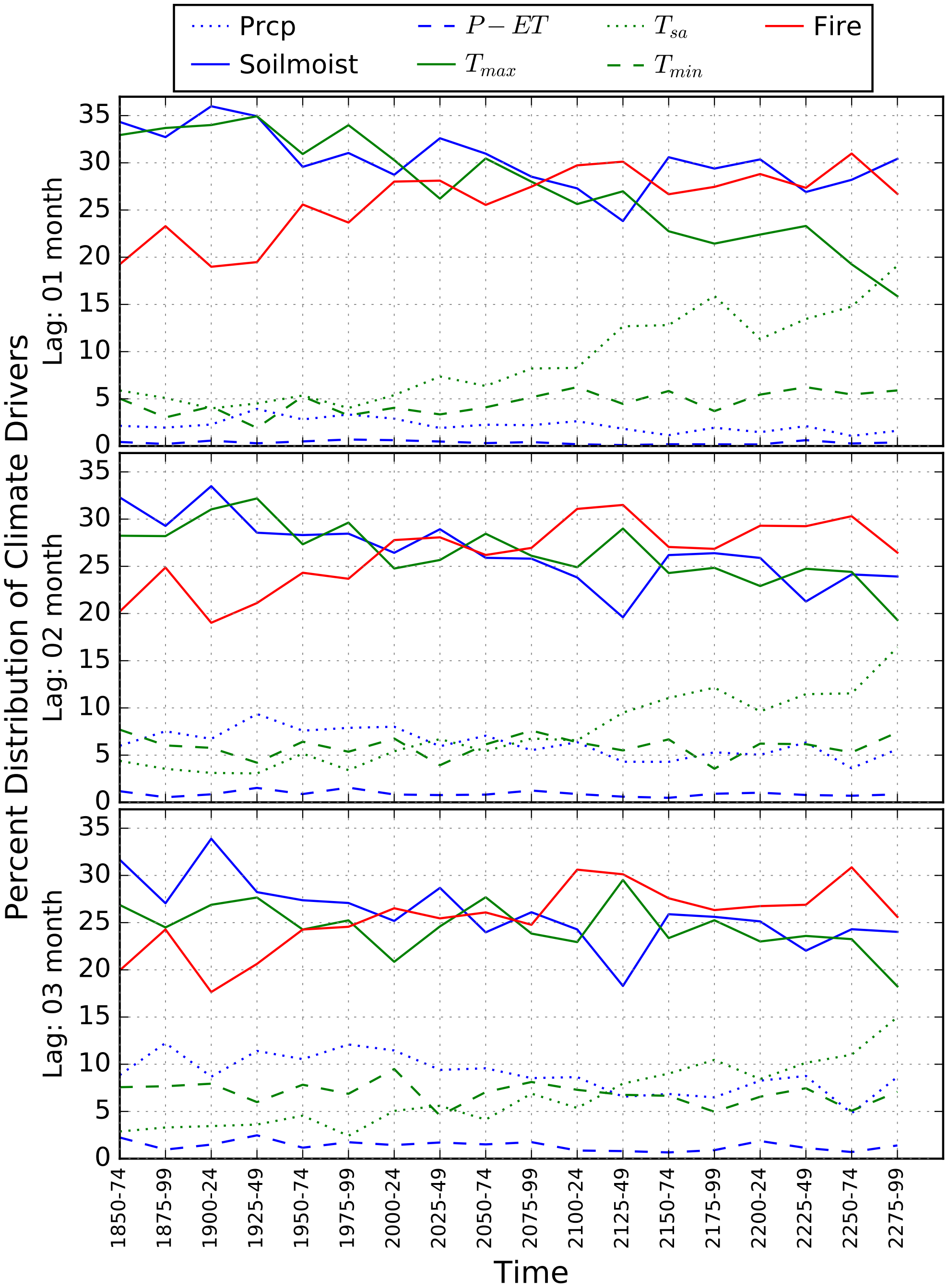

Figure 2.7: Percent distribution of global dominant climate drivers with LULCC for every time window from 1850–2299. For a particular lag month (1, 2, 3, etc.), a climate driver with highest correlation coefficient ($p < 0.05$) with carbon cycle TCEs at any grid cell is called a dominant climate driver.

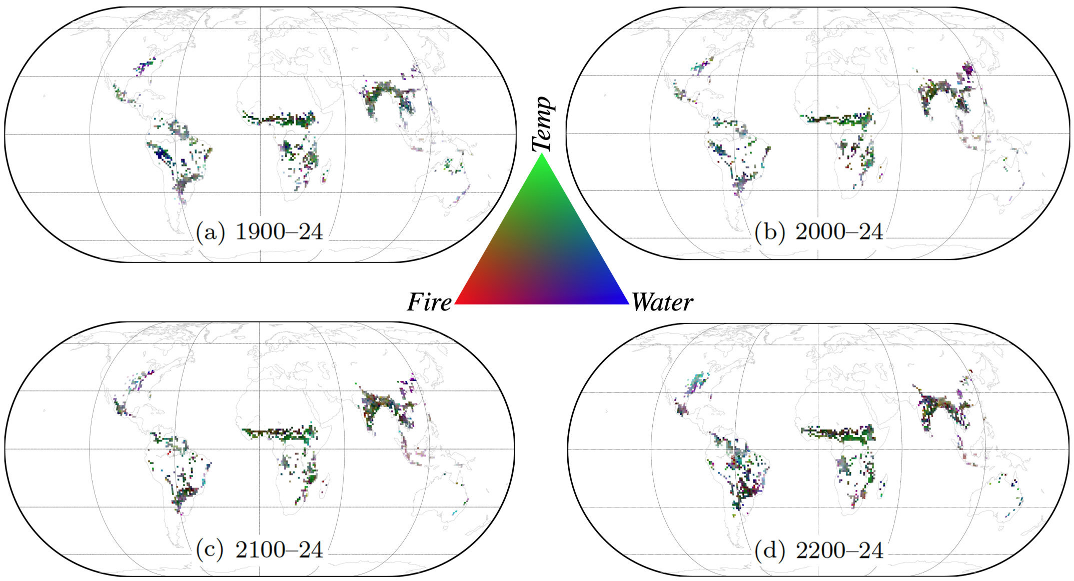

Figure 2.8: Spatial distribution of climate drivers causing negative TCEs in GPP for simulation with LULCC for four 25-year time windows, (a) 1900–24, (b) 2000–24, (c) 2100–24, and (d) 2200–24. The climate drivers are pooled in three colors, red, green, and blue. Red ($Fire$) is for loss of carbon due to fire, green ($Temp$) represents monthly maximum, mean, and minimum daily temperatures ($T_{\max}$, $T_{\text{sa}}$, $T_{\min}$ respectively), Blue ($Water$) includes monthly means of soil moisture, precipitation and $P-E$ (precipitation minus evapotranspiration). The results shown here are at 1 month lag.

the ecosystem. A decline in precipitation and soil moisture compounded with warm temperature may cause an unprecedented increase in loss of carbon uptake and potentially reduce the terrestrial carbon sink.

The combined effect of climate drivers often has a larger impact on extremes in carbon cycle than the simple addition of individual climate drivers [47, 21, 18, 31]. To capture the compound effect of climate drivers (Table 2.1) on GPP TCE events, the climate drivers were grouped under fire, temperature, and water-driven extremes (Section 4.2.4). Figures 2.8 and A5 show the spatial distribution of climate drivers at a lag of one month for simulations *with* and *without LULCC*, respectively. We observed an increase in the number of TCEs in GPP and changes in the spatial distribution of GPP TCEs and climate drivers for time periods 1900–24, 2000–24, 2100–24, and 2200–24 in the simulation *with LULCC* (Figure 2.8). Most locations experienced TCE events due to the combined effects of all the climate drivers.

We computed all combinations of water (dry or wet), temperature (hot or cold), and fire-

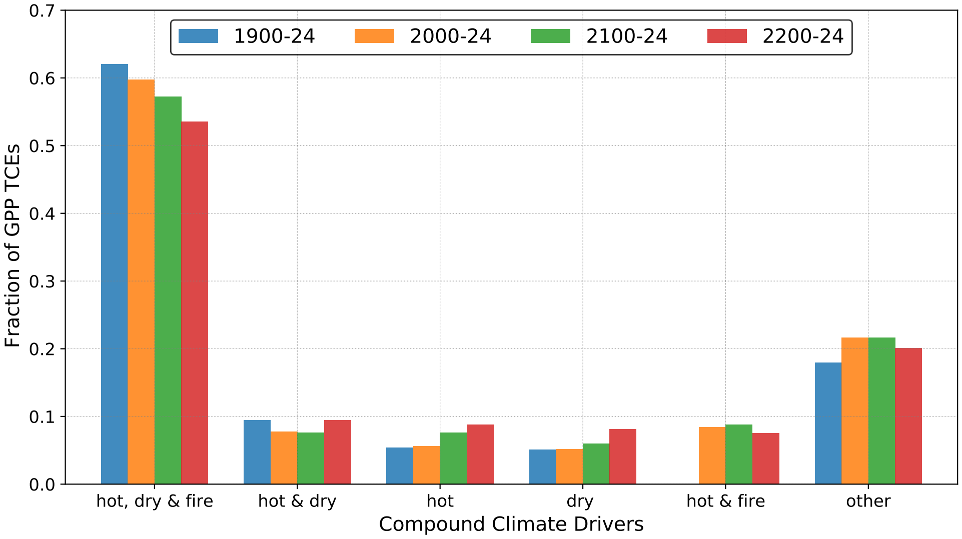

Figure 2.9: Attribution of temporally continuous extreme events in GPP to compound effect of climate drivers for the simulation with LULCC at lag of 1 month for 25-year time windows, (a) 1900–24, (b) 2000–24, (c) 2100–24, and (d) 2200–24. The fractions are mutually exclusive, i.e., events driven by *hot and dry* climate is not counted in either *hot* or *dry* climate driven events. Any location could be affected by one or compound climatic conditions. For example, a carbon cycle extreme could be driven by any combination of hot or cold, dry or wet, and with or without fire. We only show the combination of driving climate drivers that have total fraction of more than 0.05. The combined effect of hot and dry climate accompanied by fire leads to most negative TCE events in GPP.

driven climatic conditions that cause GPP TCEs. For brevity, we report results for one 25-year time window one per century. The fractions (larger than 0.05) of total negative TCEs in GPP driven by mutually exclusive climate conditions are shown in Figure 2.9. More than half of the total TCEs in GPP occurred when the environmental conditions are hot and dry, resulting in fire events and account for large reductions in GPP (Figure 2.8 and 2.9). Similar to other studies [21, 18], a stronger correlation between warm and dry climate has a substantial impact on the terrestrial carbon cycle. The increased fraction of TCEs attributed to hot climate over time is possibly due to combined attribution of $T_{\mathrm{max}}$ and $T_{\mathrm{sa}}$, as shown in Figure 2.7. Figure A6 represents the total fraction of TCEs in GPP driven by mutually inclusive climatic conditions. As global warming increases the temperature of the planet, ecosystems will become more vulnerable to the hot and dry climate and at increasing risk of fire events (Figure 2.9).

Here we highlight the temporal changes in the distribution of carbon cycle extremes and their climate drivers for the simulation *with LULCC*. East Asia experiences a large number of TCEs during the 21$^{\text{st}}$ century (Figure 2.8) driven by dry climate and fire, which however declines in the 22$^{\text{nd}}$ due to an increase in precipitation and available soil moisture. The Savannas near Congo in Africa display an increased vulnerability of vegetation to fire and hot temperatures. The impact of LULCC in Savannas is prominent after 2100 (Figures A5(d) and 2.8(d)) when the pattern of dominant drivers change from temperature-driven (green color) to a compound effect of increase in dry, hot, and fire conditions (gray color). The contiguous United States (CONUS) experiences more GPP TCEs, especially in the 23rd century (Figure 2.8(d)), driven by hot temperature and water limitation (highlighted in cyan color). Indonesia and its neighboring islands show increasing GPP TCEs attributed to a combination of hot temperatures and fire. The number of negative TCEs in South America are approximately the same for periods in Figures 2.8(a), 2.8(b) and 2.8(c) except for the period 2200–24 (Figure 2.8(d) when the extremes show a large increase. During 2200–24, South America shows a drastic increase in negative TCEs that is attributed primarily to dry, hot, and fire conditions (represented by gray color). Africa experiences an increase in the number of GPP TCEs attributed to hot climate, and, in the far future (2101–2300), witnesses an increased frequency of fire events. Australia's east coast also exhibits an increase in GPP TCEs because of water limitation, dry climate, and they are accompanied by fires in the far future. The South and Southeast Asia (composed of India, Myanmar, Thailand, and Cambodia) experiences an increase in TCEs in GPP over time. These Asian regions where primary forest were converted to cropland [27], saw an increase in fire-driven extreme events in GPP, highlighting a rising vulnerability to fire events due to LULCC.

## 2.5 Discussion

### 2.5.1 Regional Analysis of Climate Change Impact on Climate Drivers and Negative Carbon Cycle Extremes

Most climate models show an increase in the interannual variability of land–atmosphere $CO_2$ exchange over time [52]. The increasing atmospheric $CO_2$ concentration influences climate through its radiative effect (i.e., Greenhouse effect) and indirectly through physiological effect (reduced plant transpiration) [53]. The increasing radiative effects cause changes in circulation, impacting precipitation, soil moisture, and global scale water cycle. Increase in precipitation and $CO_2$ fertilization and reduction in stomatal conductance could lead to an increase in GPP; however, droughts, heatwaves and fires curtail plant photosynthesis [54]. Under climate change, while most regions experience an increase in mean GPP, some regions exhibit a decline.

Reduction in growth rate of expected terrestrial carbon uptake below carbon emissions could lead to weakening of carbon sink capacity (Figure A7). Increase in total GPP and IAV in GPP over time contribute to the increase in magnitude of negative carbon cycle extremes, defined here as negative extremes in GPP. However, some regions experience weakening of negative carbon cycle extremes often due to decline in total GPP, and reduction in IAV of GPP and climate drivers (Figure A8). Driven by large scale circulation changes, increasing temperature and decreasing precipitation and soil moisture in Central America (CAM) lead to forest mortality, decline in GPP and weakening of negative carbon cycle extremes. The decrease in precipitation in the Northern South American Tropics (NSA) and Central Amazon Basin (CAB) and increase in precipitation in the Southwest Amazon Basin (SAB) is due to plant physiologic response. Langenbrunner et al. (2019) [55] investigated this phenomenon in the regions of the Amazon and the Andes and found that under increased atmospheric $CO_2$, stomatal conductance decreases, reducing water loss through transpiration, which decreases the convective activity and causes a reduction in rainfall over the Amazon Basin (CAB, NSA) and increases moisture advection by low-level westward jets towards the Andes, leading to increases in the rainfall over the Andes (SAB). Reducing variability and increasing precipitation over SAB increase available soil moisture increasing regional GPP, however with reduced IAV, resulting in weakening of negative carbon cycle extremes. Although CAB witnesses a decline in precipitation it demonstrates an increase in GPP likely due to slight reduction in soil moisture and large $CO_2$ fertilization effect which compensates for the reduction in soil moisture. Hence, in CAB both GPP and IAV in GPP increases over time causing strengthening of negative carbon cycle extremes. These regional patterns of changes in GPP, negative carbon cycle extremes, and climate drivers are seen across the globe. For example, the regional changes in Northern Guinea, Southern Guinea, Central Guinea and Indonesia resemble the processes in CAM, SAB, CAB and CAM, respectively. Additional feedbacks due to LULCC – as tropical forests are replaced with crops or grasslands that transpire less than forests, further reducing rainfall over the Amazon – causes hotter and drier climate with an increasing risk of fire and larger losses of carbon uptake (Figures A9 and A10).

Our robust attribution analysis based on successive time windows captures the changes in the anomalies of climate drivers and carbon cycle. During 1900–24 and 2000–24, most of the negative TCEs in GPP that occurred in SAB (Figure 2.8), were due to water limitation (highlighted by the blue color in the RGB maps). With increased water availability in SAB [55], the effects of heat associated with temperature increases are mitigated and the number of negative carbon cycle extremes reduces. The decrease in precipitation in NSA led to a reduction in soil moisture, resulting in a hot and dry climate, thus making the vegetation prone to fire at high temperatures (the compound effect is highlighted by the gray color). The reduced GPP in NSA over time further leads to a fewer number of negative carbon cycle extremes (Figure 2.8). Large IAV and anomalies in GPP in CAB lead to increased concentration of negative TCEs in GPP driven possibly due to combined effect of increased hot, dry, and fire events (shown in gray color).

### 2.5.2 Drivers and Triggers of Carbon Cycle Extremes

A grid cell could experience any number of extreme events of any length during successive 25 year time windows from 1850 through 2300. Our methodology helps identify long temporally continuous extremes which represent large magnitude carbon extremes and have higher significant regression coefficient. We use this methodology to identify the prevailing climatic conditions that act as triggers for an extreme and the conditions that cause an extreme to persist. We demonstrate the findings from Chaco Province in Argentina where the major plant functional type is broadleaf deciduous tree (43%).

Under the simulation *without LULCC* and the time period 2000–24, the total number of positive TCE events in GPP were seven with a total duration of 53 months, which were greater than the total five negative TCEs in GPP with a total duration of 40 months (Table A2). The total gain in carbon uptake was 35.17 TgC, which was greater than the total loss in carbon uptake of −28.15 TgC, resulting in a net gain in carbon during TCE events. Under the simulation *with LULCC*, during the same period of 2000–24 the total number of negative GPP TCEs (6 events, 57 months) were greater than positive TCEs (5 events, 35 months). Thus, the total loss in carbon uptake ($-35.86$ TgC) *with LULCC* was higher than the gain in carbon uptake (23.87 TgC). While this region had a net gain in carbon uptake of 7.02 TgC for the simulation *without LULCC*, and it had a net loss in carbon uptake of $-11.99$ TgC for the simulation *with LULCC*. The increase in negative extremes in GPP with net losses in carbon uptake demonstrates the role of human-induced LULCC in negatively affecting carbon uptake capacity.

We performed a qualitative investigation of every negative and positive TCEs in GPP (Figure A11) using normalized time series of GPP, GPP anomalies and anomalies of major climate drivers ($Prcp$, $Soilmoist$, $T_{\max}$, and $Fire$). Most positive TCEs in GPP were driven by increase in precipitation, followed by rise in soil moisture and decline in $T_{\max}$. Most negative extremes in GPP were driven by decline in precipitation and rising $T_{\max}$, which cause high evapotranspiration and loss of soil moisture, eventually creating dry and hot conditions that cause fire events. Some of the negative extremes in these regions were also found to be driven by hot and dry events without fire.

To identify the triggers of carbon cycle extremes, we define the onset period of GPP TCEs as first-quarter of every TCE. The regression onset period of GPP TCEs and anomalies of climate drivers were computed with consideration of the lagged response of climate drivers on GPP TCEs. The lagged soil moisture anomalies were highly correlated ($p < 0.01$) with entire duration of TCE events (persistence, Table A3), and the lagged precipitation anomalies were highly correlated with the onset (trigger, Table A4) of TCE events in the Chaco Province.

For the simulation with $CO_2$ only forcing (i.e. *without LULCC*) during time period 2000–24, the correlation coefficient, for the whole duration of GPP TCEs, was highest for soil moisture anomalies at a lag of 1 month. The precipitation anomalies had high positive correlations with GPP TCEs (i.e., reduction in precipitation was correlated with a decrease in GPP) at lags of 3 and 4 months. $T_{\max}$ and $Fire$ had large negative correlations with GPP anomalies (i.e., increase in temperature correlates with a decrease in GPP or increase in carbon uptake loss) at a lag of 2 months. Hence, for a negative GPP TCE event, the compound effect of a decline in precipitation followed by increase in temperature caused a reduction of soil moisture, resulting in hot and dry conditions, increasing the probability of occurrence of fire and causing a long negative TCE event ($Prcp > T_{\max} > Soilmoist >$ TCE). For the same region under simulation *with LULCC*, the dominant trigger was $T_{\max}$ (Table A5) followed by precipitation. Therefore, human-induced LULCC coupled with increasing $CO_2$ levels tends to enhance the vulnerability and loss in vegetation due to hot and non-dry climate conditions, resulting in more negative extremes in GPP. The analysis illustrates the strength of our methodology in identifying the evolution of carbon cycle extremes for multiple conditions and at fine resolution.

### 2.5.3 Limitations of CESM1(BGC)

The ILAMB benchmarking scores [34] of the carbon fluxes and climate drivers indicate that CESM1(BGC) is among the best CMIP5 models (Table A1). However, the Community Land Model version 4 (CLM4), the land model used in the CESM1(BGC) [28], had some limitations which could potentially impact some of our findings. The simulated GPP by CLM4 had a positive bias across the globe compared to FLUXNET eddy covariance tower estimates due to lack of colimitation of GPP to canopy scaling and parameterization of leaf photosynthesis kinetics [29]. With improvements in the model parameterizations of radiative transfer, leaf photosynthesis and stomatal conductance, canopy scaling of leaf processes, inclusion of multilayer canopy model, and updated maximum rate of electron transfer parameters [29, 56], the positive bias in GPP was reduced. With inclusion of vertically resolved CN model in CLM4.5 [30], the positive bias in GPP was further improved and terrestrial carbon storage increased consistently with observations. In the current study focused on the patterns of carbon cycle extremes, the positive bias of GPP was likely captured by trend and removed for calculation of GPP anomalies. However, any associated increase in the IAV of GPP corresponding to positive bias of GPP would increase the magnitude of GPP anomalies and both negative and positive GPP extremes. Thus, there is a potential to overestimate the magnitude of both negative and positive GPP extremes but the relative comparison is insightful and most likely not affected by this limitation of CLM4.

CLM4 lacks representation of dynamic crop, thus the cooling effects in irrigated lands, changes in the sensible and latent heat, and soil carbon change are not well represented in CLM4.0 but were improved in the CLM5.0 [57]. The simulated climate-carbon feedbacks in CLM4 assume an instantaneous response of plant physiological processes to changes in temperature [58]. With inclusion of temperature acclimation, though the ecosystem carbon storage pool grew (mostly in higher latitudes), the effect on photosynthesis of tropical regions was minimal. Since most of the detected extremes in the tropical forest and other high biomass regions, the lack of representation of agriculture and temperature acclimation on GPP are not expected to have significant effect on the analysis of extremes.

## 2.6 Conclusions

Using the fully-coupled Earth system model, CESM1(BGC), we analyzed the development of extreme events in GPP and attributed those carbon cycle extremes to climate drivers from the year 1850 through 2300 for simulations *with* and *without LULCC*. The changes in land cover directly modify the biogeophysical and biogeochemical feedbacks of terrestrial vegetation and indirectly through the physiological responses of vegetation on climate drivers, leading to increase in interannual variability in GPP and higher magnitude of GPP anomalies. Relative to the simulation *without LULCC*, the simulation *with LULCC* exhibited increased variability in GPP and higher intensity, duration, extent, and frequency of extremes in GPP. These characteristics were greater for negative extremes in GPP than positive extremes, implying larger than expected losses in carbon uptake than carbon gains. Although the total GPP for the simulation *with LULCC* was less than the total GPP *without LULCC*, the simulation *with LULCC* showed a sharper decline of carbon uptake of $-6.9\%$ in the near future (1850–2100) and $-10\%$ in the far future (2100–2300) with respect to total GPP *without LULCC*.

Increasing atmospheric $CO_2$ concentrations drive growth in vegetation photosynthesis or GPP due to carbon fertilization, and reduction in stomatal conductance. Due to circulation changes, a few regions witness a decrease in precipitation, creating a drier climate that when supplemented with warmer temperatures lead to decline in GPP, such as the regions of the eastern Amazon and Central America. Reducing magnitudes of GPP over time and analogous decreases in the interannual variability of GPP produce weakening of negative carbon cycle or GPP extremes in the Amazon. Moreover, the weakening of other negative carbon cycle extremes could be a result of less variable and benign climatic conditions for vegetation productivity, as seen around the Andes. Hence, it is imperative to inspect trends in GPP and negative carbon cycle extremes simultaneously to understand the nature of changes in extremes and their implications at regional scales.

We found that the duration of GPP TCEs increased with higher $CO_2$ concentration.The duration and impact of negative TCEs in GPP are enhanced when human-induced LULCC was considered, resulting in increased loss in carbon uptake. We illustrated this with the case study of the Chaco Province in Argentina that had a net gain in carbon uptake (7.02 TgC) during 2000–24 in the simulation *without LULCC* and while a net loss in carbon uptake ($-11.99$ TgC) in the simulation *with LULCC*.

The dominant climate driver was soil moisture that had highest correlations with GPP extremes ($p < 0.05$) and the correlations were mostly positive, indicating that anomalous decrease in soil moisture or drier climate conditions cause anomalous reductions in GPP. Other major individual drivers were hot temperatures and fire. Fire was a dominant climate driver, especially after 2100 in the simulation *with LULCC*, highlighting the increased vulnerability of ecosystems to fire events due to the impact of human activities on ecosystems. We also found that the decline in precipitation triggers a negative carbon cycle TCE event, but the reduction in soil moisture or water limitation was the dominant driver for those negative carbon cycle TCE events to persist. The compound effects of climate drivers were also analyzed, and an increasing number of regions under carbon cycle extremes were attributed to hot and dry conditions. The largest fraction of negative carbon cycle extremes were driven by the compound effects of hot, dry, and fire events. Warmer conditions under climate change increases the risk of occurrence of fire events and their impacts on the carbon cycle and extremes of the future.

This study presents a detailed analysis of detection and identification of carbon cycle extreme events, how these extremes evolve from 1850 through 2300, and how human-induced LULCC alters them using a fully coupled Earth system model forced with the RCP 8.5 and ECP 8.5 $CO_2$ concentration scenarios. It also attributes the climate drivers of such extremes in carbon cycle, and analyzes the changing patterns and dominance of climate drivers, under *with* and *without LULCC* scenarios. Study provides new insights into the contribution of human activities in altering carbon cycle extremes and the vulnerability of terrestrial vegetation and associated ecosystem services that could present increasing risks to human lives, wildlife, and food security.

# Chapter 3

# Carbon Cycle Extremes Accelerate Weakening of the Land Carbon Sink in the Late 21st Century

## 3.1 Introduction

Rising anthropogenic carbon dioxide ($CO_2$) emissions are leading to increases in Earth's surface temperature and climate variability as well as intensification of climate extremes. Terrestrial ecosystems have historically taken up a little over one-quarter of these emissions via carbon accumulation in forest biomass and soils [2] and helped constrain increasing atmospheric $CO_2$ concentrations. The increase in the net terrestrial carbon sink is a result of reduced deforestation, enhanced vegetation growth driven by $CO_2$ fertilization, and lengthening of growing seasons in high latitudes. The growing terrestrial carbon sink provides a negative feedback to climate change; however, exacerbating environmental changes and climate extremes, such as droughts, heatwaves and fires, have the potential to reduce regional carbon stocks and moderate carbon uptake [6, 59]. Net biospheric production (NBP), the total downward flux of carbon from the atmosphere to the land, represents the net carbon uptake after accounting for carbon losses from plant respiration, heterotrophic respiration, fire, and harvest [5] and is a critical measure of land carbon storage. Climate-driven large anomalies in NBP could impact the structure, composition, and function of terrestrial ecosystems [18]. To improve our understanding of the climate–carbon cycle feedbacks, especially during such large carbon anomalies, we investigated the changing magnitude, frequency, and spatial distribution of NBP extremes over decadal time periods and identify the influential climate anomalies that potentially drive large NBP extremes at regional and global scales.

Terrestrial carbon cycle processes, such as photosynthesis, respiration and elemental cycling control the structure, composition and function of terrestrial ecosystems. In the past few decades, the global terrestrial carbon cycle has taken up 25–35% of the $CO_2$ emissions from anthropogenic activities such as fossil fuel consumption, deforestation and other land use changes [60]. With rising atmospheric $CO_2$, the carbon uptake by both the land and the ocean has also increased but with significantly greater variability over land [2]. The interannual variability in land carbon uptake is strongly influenced by climate extremes, and it is primarily responsible for the interannual variation in the atmospheric $CO_2$ growth rate [60].

Climate extremes are part of Earth's climatic variability, affecting terrestrial vegetation and modifying ecosystem-atmosphere feedbacks [61]. Recent studies have investigated the influence of rising temperatures on climate extremes and terrestrial ecosystems [61, 62, 18, 47, 59]. Observations and climate models suggest that climate change has increased the severity and occurrence of the hottest month, hottest day, and driest and wettest periods [62]. Heavy precipitation or lack thereof could have a negative feedback on the carbon cycle via soil water-logging or drought stress, respectively [6]. A few studies have investigated the impact of climate extremes on the carbon cycle and found that hot and dry extremes reduce land carbon uptake, especially in low latitudes and arid/semi-arid regions [48, 18]. Attribution studies infer that the compound effect of multiple climate drivers has a larger effect on the carbon cycle and its extremes [59, 47, 48, 18, 6] than any individual climate driver. Most attribution methods focus on analyzing the response of the carbon cycle to climate, aggregated over annual, sub-annual, and seasonal scales; however, the responses may vary over shorter time scales, including daily to monthly.

The variability in climate–carbon cycle feedbacks is dependent on geographical location, among other factors. Grose et al. (2020) reported that while Australia is expected to experience an overall reduction in precipitation by 2100, the spatial distribution of precipitation varies since a few regions are expected to get more and others will receive less precipitation [63]. Ault et al. (2020) etfound that despite the overall increase in precipitation and water-use efficiency globally, the available soil moisture may be reduced across many regions due to increased evapotranspiration from higher temperatures, exceeding the supply from precipitation [64]. The regions that see a decrease in supply and increase in demand for water are sensitive even to relatively small increases in temperature. These feedbacks will increase the severity of droughts, and ENSOs may further amplify the effect [64]. Net primary production (NPP) sensitivity to temperature is negative above

15°C and positive below 10°C [48], which means warming will cause a reduction in carbon uptake in the tropics and extra-tropics and an increase in carbon uptake at higher latitudes. However, with increasing average surface temperatures, the NPP sensitivity could become negative over time in high latitude regions.

Rising atmospheric $CO_2$ levels and climate change could have implications for biological [18] and ecological systems since the severity and occurrence of climate extremes, such as heatwaves, droughts, and fires, are likely to strengthen in the future. These systems are more sensitive to climate and carbon extremes than to gradual changes in climate. The increasing frequency and magnitude of climate extremes could reduce carbon uptake in tropical vegetation, reduce crop yields [65], and negate the expected increase in carbon uptake [6]. In this study we investigated the extremes in NBP and their climate drivers from Earth system model simulations for the period 1850–2100 across several regions around the globe. The objectives of this research were to 1) quantify the magnitude, frequency, and spatial distribution of NBP extremes, 2) attribute individual and compound climate drivers of NBP extremes at multiple time lags, and 3) investigate the changes in climate–carbon cycle feedbacks at regional scales.

## 3.2 Methods

### 3.2.1 Data

We used the Community Earth System Model (version 2) (CESM2) simulations at $1^\circ \times 1^\circ$ spatial and monthly temporal resolution to analyze the carbon cycle extreme events in net biospheric production. The CESM2 is a fully coupled global Earth system model composed of atmosphere, ocean, land, sea ice and land ice components. The simulations analyzed here were forced with atmospheric greenhouse gas concentrations, aerosols and land use change for the historical (1850–2014) and Shared Socioeconomic Pathway 8.5 (SSP5-8.5; 2015–2100) scenario, wherein atmospheric $CO_2$ mole fraction rises from about 280 ppm in 1850 to 1150 ppm in 2100 [66]. While $CO_2$ forcing causes temperatures to increase, changes in aerosols and land use have a slight cooling effect [67], resulting in an overall increase of about 8°C in mean air temperature over the global land surface during 1850–2100.

### 3.2.2 Definition and Calculation of Extreme Events

The Intergovernmental Panel on Climate Change (IPCC) [40] defines extremes of a variable as the subset of values in the tails of the probability distribution function (PDF) of anomalies. Based on the global PDF of NBP anomalies, we selected a threshold value of $q = 5$, such that total positive and negative extremes constitute $5\%$ of all NBP anomalies (Figure B1). The negative and positive extremes in NBP were comprised of NBP anomalies smaller than $-q$ and larger than $q$, respectively. While the total number of NBP extremes was constant (i.e., $5\%$ of all NBP anomalies) for any time period, the count and intensity among positive and negative extremes vary, depending on the nature of the PDF of NBP anomalies.

We computed extremes for every 25-year period from 1850 through 2100 to analyze the changing characteristics of NBP extremes at regional to global scales. For regional analysis, we used the 26 regions defined in the IPCC Special Report on Managing the Risks of Extreme Events and Disasters to Advance Climate Change Adaptation [40], hereafter referred to as the SREX regions (Figure B2). We analyzed the characteristics of NBP extremes during carbon uptake periods, when photosynthesis dominates NBP, and land is a net sink of carbon (NBP $> 0$), and carbon release periods, when NBP is dominated by respiration and disturbance processes, and land is a net source of carbon (NBP $< 0$) [16].

The anomalies in NBP were calculated by removing the modulated annual cycle and nonlinear trend from the time series of NBP at every grid cell. We calculated the modulated annual cycle and nonlinear trend of NBP using singular spectrum analysis, which is a non-parametric spectral estimation method that decomposes a time series into independent and interpretable components of predefined periodicities [42]. The conventional way of computing annual cycle or climatology does not capture the intrinsic non-linearity of the climate–carbon feedback [45]. The modulated annual cycle, composed of signals with return periods of 12 months and its harmonics, is able to capture the varying modulation of the seasonality of NBP under rising atmospheric $CO_2$ concentrations. The nonlinear trend is comprised of return periods of 10 years and longer, such that the anomalies in the ecosystem and climate drivers capture the effects of ENSO, which has a large impact on climate and the carbon cycle [68, 64]. Thus, NBP anomalies consist of intra-annual variability, represented by high-frequency signals ($<$12 months), and the interannual variability ($>$12 months and $<$10 years).

### 3.2.3 Attribution to Climate Drivers

While most studies traditionally attribute carbon cycle impacts to changes in climate at seasonal to annual time scales, many carbon cycle responses to climate variability occur at shorter, daily to monthly, time scales [18]. Some recent studies have performed attribution by comparing the median of the climate driver distribution in a large space-time dimension [68, 31], which may not capture the variability at regional to grid cell scales. Using linear regression of time-continuous NBP extremes that represent the large intra-annual and interannual variation in NBP with climate anomalies, we quantified the dominance (regression coefficient) and response (sign of the regression coefficient) of climate drivers on large NBP extremes. The NBP extreme events could either occur contiguously over time and space, or be isolated from other events. Long duration time-continuous extreme events have a larger impact on the terrestrial ecosystem than time-separated isolated extreme events. As described by Sharma et al. (2022), we define time-continuous extreme (TCE) events such that they fulfill the following conditions [59], (i) they must consist of isolated extremes that are continuous for at least one season (i.e., 3 months) and (ii) any number of isolated or contiguous extremes can be a part of a TCE event if the gap between such extremes is less than one season in length (i.e., up to 2 months). We assume that extreme events separated by gaps greater than or equal to one season length are separate TCE events.

Human activities, such as fossil fuel emissions and land use changes, modify biogeochemical and biogeophysical processes, which alter the climate through climate–carbon feedbacks. Large anomalous changes in climate drivers have a strong impact on carbon uptake and biospheric productivity. Here, we attributed NBP TCEs to climate drivers, namely, precipitation (“Prcp”), soil moisture (“SM”), monthly average daily temperature (“TAS”), and biomass loss from carbon flux into the atmosphere due to fire (“Fire”). As the terrestrial vegetation has ingrained plasticity to buffer and push back effects of climate change [46], the impacts of changes in climate drivers are often associated with lagged responses. Moreover, the strength of the impact of climate on NBP is dependent on location, timing, and land cover type [18]. Linear regressions of TCEs in NBP and anomalies of every climate driver were identified at all affected land grid cells for lags from one to four months. We assumed that the higher the Pearson Correlation coefficient ($\rho$) of a climate driver with NBP extremes, the larger is its impact on NBP at that location. The attribution based on $\rho$ is used only for those grid cells for which the significance value $p < 0.05$. The grid cells with at least two negative and positive NBP TCEs each often yielded high correlation coefficients with high significance values ($p < 0.05$); thus, this constraint was applied for attribution to climate drivers.

The instantaneous impact (when lag equals zero months) of driver anomalies ($dri_t$) on NBP TCEs ($nbp_t$) is computed using Equation 3.1, where $N$ represents the number of months in TCEs at any grid cell. Attribution based on the lagged response of driver anomalies on NBP TCEs was computed using Equation 3.2, where $L$ represents the number of lagged months. For lags greater than one month, we computed the correlation of the average of climate driver anomalies, $\frac{dri_{t-l}}{L}$ for every time-step in the driver anomalies, with *nbp*$_t$. The resulting $\rho$ captures the average response of antecedent climatic conditions up to *L* months in advance that drive NBP TCEs.

for lag = 0:

$$\rho = corr(dri_t, nbp_t) \ \mid \ t\epsilon N \tag{3.1}$$

for lag $>$0:

$$\rho = corr(\sum_{l=1}^{l=L} \left(\frac{dri_{t-l}}{L}\right), nbp_t) \ \mid \ t\epsilon N \tag{3.2}$$

The direction and strength of the impact of various climate drivers on plant productivity and the carbon sink vary with space and time. Increased temperatures could lead to increased respiration and losses in NBP in the tropics and mid-latitudes, but an increase in temperature could conversely lead to higher photosynthetic activity and greater uptake at higher latitudes. A moderate reduction in precipitation may not severely impact vegetation productivity, but if accompanied by a heatwave, it could lead to large losses in NBP. We analyzed the dominant climate drivers across SREX regions for every 25-year period from 1850 to 2100 to understand the changing characteristics of large spatio-temporal extremes and their drivers across time and space.

Anomalous climate drivers causing NBP extremes may or may not qualify as climate extremes by themselves. A recent study found that the periods of extreme climate and NBP often do not occur at the same time, and the compound effect of non-extreme climate drivers could produce an extreme in NPP [48]. Occurrence of a NBP extreme is also likely driven by the compound effect of multiple climate divers, we identified co-occurring anomalous climatic conditions during and antecedent to NBP extremes to improve our understanding of the interactive compound effect of drivers on the carbon cycle. Since the dominance of climate drivers are usually quantified by a correlation coefficient range of 0.5–0.7 [69], we imposed a limit of correlation coefficients $\rho > 0.6$ and significance values $p < 0.05$ on co-occurring individual climate drivers to qualify as individual or compound drivers of NBP extremes. These constraints yield a smaller number of extremes that are attributable to climate drivers with high confidence.

## 3.3 Results and Discussion

### 3.3.1 Characteristics of NBP Extremes

The $5^{\text{th}}$ percentile NBP anomalies computed for every 25-year period from 1850 to 2100 rendered threshold trajectories that increase from 140 GgC/month to 220 GgC/month (Figure 3.1(a)). This 1.5 times increase in threshold values demonstrates the increasing magnitude of anomalies and interannual variability of NBP across the globe. The corresponding time series of intensity of losses and gains in biome productivity were calculated by integrating the negative (NBP anomalies $< -q$) and positive (NBP anomalies $> q$) extreme anomalies. The rate of increase in the magnitude of negative extremes ($-834$ MgC/month) was larger than that of the positive extremes (804 MgC/month) (Figure 3.1(b)), which implies that over time the net losses in carbon storage during NBP extremes increases.

The changes in NBP are driven by spatial and temporal variations in climate drivers and anthropogenic forcing. During 1850–1874, 24 out of 26 regions were dominated by carbon release and the total NBP was negative (Figure B3). From 1850 through the 1960s, the land experienced a net $CO_2$ loss to the atmosphere likely driven by deforestation, fire and land-use change activities [2] (Figure B9). After the year 1960, the continued increase in fossil fuel emissions raised the atmospheric $CO_2$ concentration despite declining rates of deforestation. Increasing $CO_2$ fertilization, water-use efficiency, and the lengthening of growing seasons enhanced vegetation growth and raised NBP with the largest increases in the tropics and northern high latitudes (Figure B4). After 2070, the total NBP reached its peaks and started to decline (Figure B3) as ecosystem respiration exceeded total photosynthetic activity. Tropical regions have the largest magnitude of NBP; however, the rate of increase of NBP declined after 2050 and the region of Sahara (SAH) showed an early drop in total NBP after the year 2050. Longer dry spells and intense rains due to changing precipitation patterns in Mediterranean and subtropical ecosystems are likely to cause higher tree mortality [18]. Hot temperatures and reduced activity of RuBisCO hindering carboxylation are possible factors that will likely cause a net decrease in NBP in the region of SAH and make it a net carbon source after 2050. During 2050–74 and 2075–99, low-latitude regions exhibit the highest regional NBP; however, many areas in the tropics exhibited a declining growth rate of regional NBP (Figure B4).

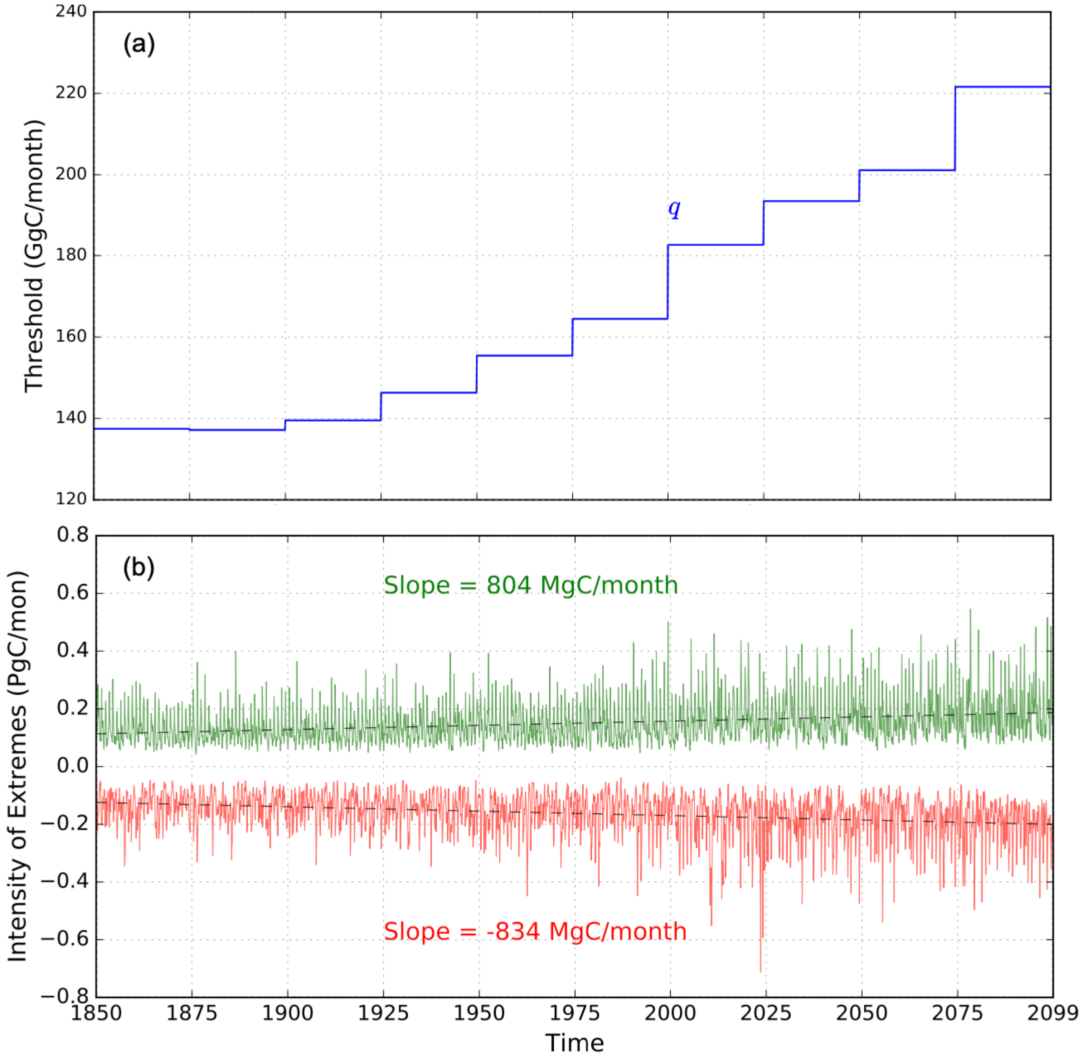

Figure 3.1: (a) The 5$^{\text{th}}$ percentile threshold, $q$, of NBP anomalies. The negative extremes in NBP are those NBP anomalies that are $< -q$ and positive extremes are $> q$. (b) The intensity of positive and negative extremes in NBP in CESM2 are represent by green and red color, respectively. The rate of increase of positive and negative extremes in NBP are 804 and $-834$ MgC per month, respectively.

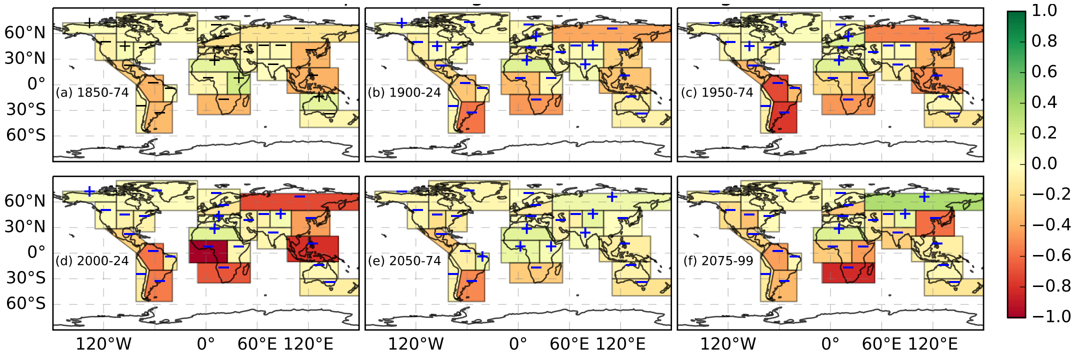

Figure 3.2: The sum of positive and negative carbon cycle extremes is referred as Net Uptake Change during NBP extremes. The figure shows the changing spatial distribution of net uptake change (PgC) during the following periods: (a) 1850–74, (b) 1900–24, (c) 1950–74, (d) 2000-24, (e) 2050–74, and (f) 2075–99. A net gain in carbon uptake is represented by a green color and a '+' sign, and a net decrease is represented by a red color and a '−' sign. For most regions, the magnitude of negative NBP extremes or losses in carbon uptake are higher than positive NBP extremes or gains in carbon uptake.

As anomalous changes in climate vary over space and time, extremes in NBP also respond to the interactive effects of climate drivers and exhibit spatial and temporal variation. Figure 3.2 shows the net total sum of both positive and negative extremes in NBP in SREX regions integrated for all 25-year periods (1850–74, 1900–24, 1950–74, 2000–24, 2050–74, and 2075–99). Most regions exhibited net losses in biospheric productivity during extremes, e.g., South Africa (SAF) has always been dominated by negative NBP extremes. The large magnitude of net carbon uptake changes during the period 2000–24 was likely driven by a change in LULCC forcing from decadal to annual during 2000–2015 and then back to decadal for 2015 onward. The change in resolution of LULCC forcing possibly caused higher climate variability due to biogeophysical feedbacks and subsequently led to increased carbon cycle variability and extremes. 23 out of 26 SREX regions experienced an overall loss in biospheric productivity during extremes near the end of the 21$^{st}$ century (Figure 3.2). The distribution of the total magnitude and count of negative TCEs during 2075–99 across all the SREX regions followed a similar pattern, i.e., more frequent extremes were accompanied by larger carbon losses (Figure 3.3(a)). The largest losses in carbon uptake during TCEs were in tropical regions, e.g., East Asia (EAS), Amazon (AMZ), and SAF, with −3, −3, and −2.25 PgC carbon losses, respectively, during 2075–99. These regions also witnessed the highest number of negative

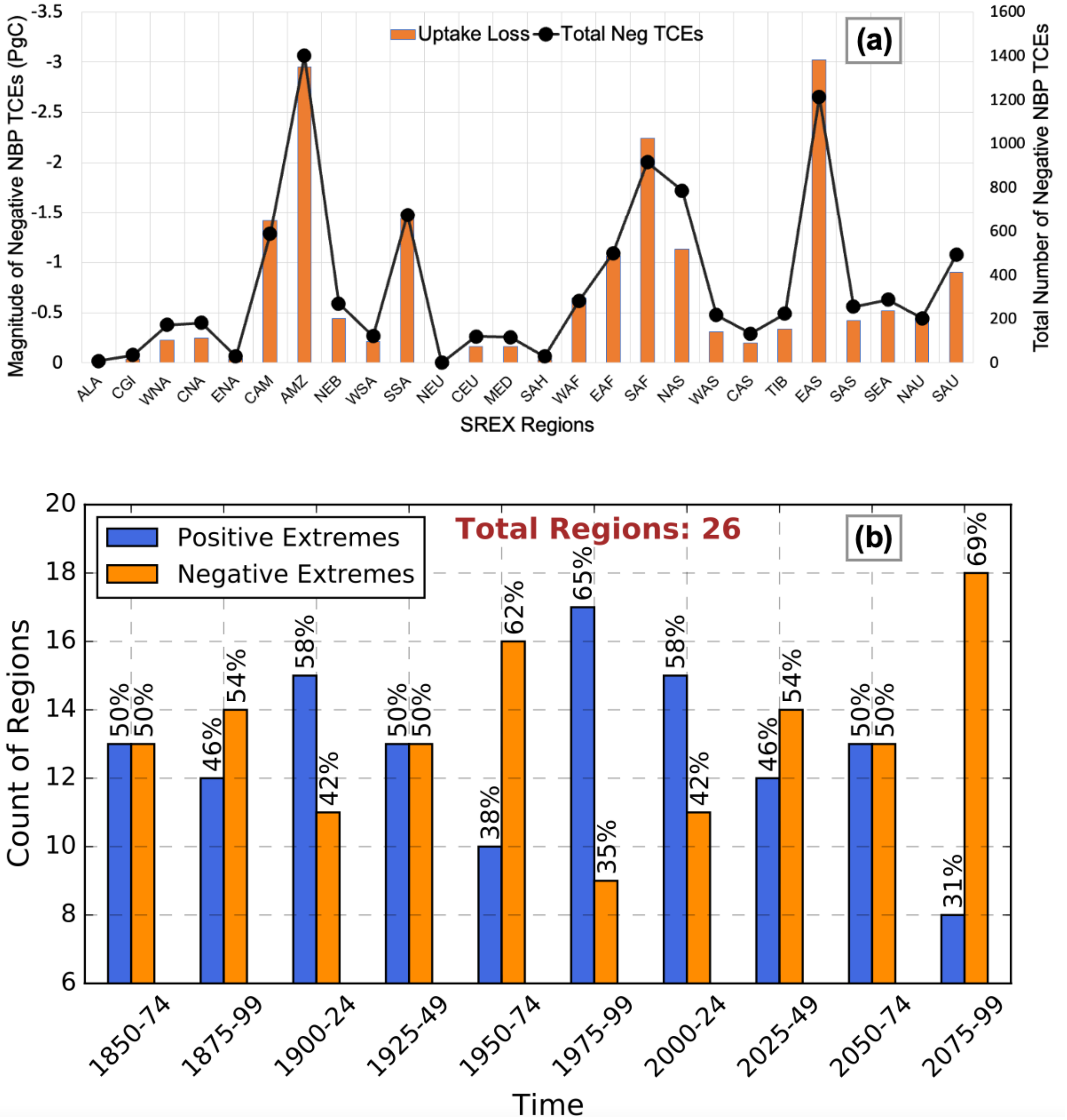

Figure 3.3: (a) Total magnitude of negative carbon cycle extremes or loss is carbon uptake during TCEs across SREX regions plotted as a bar graph (left $y$-axis). The total number of negative TCE events (right $y$-axis) plotted as line graph. The largest portion of carbon uptake loss is in the tropical SREX regions of the Amazon (AMZ), East Asia (EAS), and South Africa (SAF) for the period 2075–99. (b) Count ($y$-axis) of the regions dominated by either positive or negative NBP extremes. Relative to a total of 26 SREX-regions, the percent count of positive or negative NBP extremes is represented at the top of the bars.

NBP TCEs at 1270, 1410, 950, respectively. The magnitude of carbon losses and the number of negative NBP TCEs were highest in tropical regions. The magnitude and number of negative TCEs were very low for the high latitude regions of Alaska (ALA), Canada and Greenland (CGI), Eastern North America (ENA), Northern Europe (NEU), Central Europe (CEU), and the dry regions of the Mediterranean (MED) and Sahara (SAH). Although the number of NBP TCEs in NAS were more than in Southeastern South America (SSA) and Central America (CAM), the magnitude of NBP TCEs in NAS were low due to lower regional NBP. Since the extremes were calculated based on global anomalies, the largest impacts on terrestrial carbon uptake are expected in the regions of AMZ, EAS, and SAF, which have the largest concentrations of live biomass.

The magnitude and the total number of regions dominated by negative extremes in NBP are expected to gradually increase in the 21st century (Figure 3.3(b)). Most of the increase in the frequency of negative extremes in NBP are expected in ENA, South Asia (SAS), SAF, and CAM (Figure B5). The increase in the magnitude (23 out of 26 or 88% of all regions) and frequency (18 out of 26 or 70% of all regions) of negative NBP TCEs in most SREX regions during 2075–99 is a matter of concern since the total global NBP peaked at around 2070 and subsequently declines in the model (Figure B3). The negative NBP TCEs dominate in eight out of the nine tropical regions, which store the largest standing carbon biomass and represent the largest portion of carbon uptake loss during negative NBP extremes. A large magnitude of extreme events in the NBP could potentially lead to a state of low and decreasing carbon sink capacity that could further lead to a positive feedback on climate warming. The strengthening of negative extremes relative to positive extremes in NBP represents a net decline of terrestrial carbon sink capacity into the future (Figure B3). The positive feedback of warming and climate driven losses in carbon uptake raise concerns about the implications of reducing terrestrial uptake capacity on food security, global warming, and ecosystem functioning. Moreover, the sensitivity of vegetation responses is higher for climate and carbon extremes than for gradual changes because of larger response strength and shorter response times [18].

### 3.3.2 Attribution to Climate Drivers

The increase in climate variability and extremes driven by rising $CO_2$ emissions influences the terrestrial carbon cycle [61, 6, 59]. The control of climate drivers on NBP extremes is dependent on the regional interannual variability of climatic conditions and vegetation composition. The percent of total number of grid cells that show soil moisture as a dominant driver of NBP TCEs were about 40 to 50% from 1850 to 2100 across multiple lags, which means that the near term and long term impact of soil moisture were highest among all other drivers (Figure B6). The positive response of soil moisture anomalies on NBP TCEs indicates that a decline in soil moisture causes a reduction in NBP and vice-versa. Likewise, the dominant climate driver across the 26 SREX regions was also soil moisture and it exhibited a positive response relationship with NBP TCEs (Figure 3.4). However, the proportion of the total number of grid cells dominated by precipitation doubled (10 to 20%) when the lag was increased from 1 to 3 months. This implies that antecedent declines in precipitation limit carbon uptake more than a recent decline in precipitation and possibly causes a decline in soil moisture. Moreover, the plants with deep roots are less impacted with short-term reduction in precipitation than prolonged droughts, which are caused by soil moisture limitation. By the end of the 21st century, the model indicates that 70% of the total number of NBP extremes will be water-driven, i.e., due to soil moisture and precipitation. Our results are consistent with recent studies [70, 48] that concluded that the most important factor limiting vegetation growth is water stress, which is caused mainly by low soil moisture. Lack of soil moisture for extended periods could result in drought events, causing a larger reduction in ecosystem productivity and a smaller reduction in terrestrial respiration.

The second most dominant driver of NBP TCEs was fire, which has a positive response on NBP TCEs (Figure B6). Fire is an important Earth system process that is dependent on vegetation, climate, and anthropogenic activities. CESM2 incorporated a process-based fire model, which contains three components, namely, fire occurrence, fire spread, and fire impact [71]. The interannual variability of agricultural fires is largely dependent on fuel load and harvesting; deforestation fires included fires due to natural a nd anthropogenic ignitions, caused by deforestation, land-use change, and dry climate. Peat fires usually occur in the late dry season and are strongly controlled by climate. The current version of the fire model reasonably simulates burned area, fire seasonality, fire interannual variability, and fire emissions [71]. As fires are controlled by soil moisture, temperature, and wind, the attribution of NBP extremes to fires could also include the NBP extremes that are driven by inadequate soil moisture and hot temperatures. Therefore, the total number of fire events could be larger, and recovery after such fire driven extremes could be much longer.

Hot temperatures that persist for long periods induce heatwaves, which tend to reduce ecosystem production and enhanced terrestrial respiration, causing a large reduction in NBP [48]. Leaf photosynthesis depends on the RuBisCO-limited rate of carboxylation, which is inversely proportional to the $Q_{10}$ function of temperature in the model [67]. Hubau et al. (2020) found that with increasing temperatures and droughts, tree growth was reduced and could offset earlier productivity gains [25]. Conversely, warm temperatures in the northern high latitudes cause an

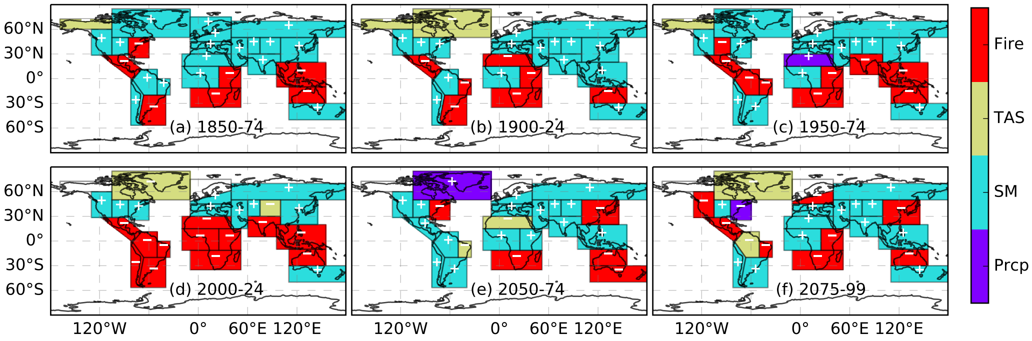

Figure 3.4: Spatial distribution of dominant climate drivers across SREX regions. The color in every SREX region represents the most climate driver causing carbon cycle extremes at 1 month lag for following periods: (a) 1850–74, (b) 1900–24, (c) 1950–74, (d) 2000-24, (e) 2050–74, and (f) 2075–99. The positive (‘+’) and negative (‘−’) sign within a region represents the correlation relationship of NBP extremes with every dominant climate drivers.

increase in carbon uptake due to reduced snow cover and optimal temperature for photosynthesis. Increased warming at northern high latitudes could lead to hot temperature-related hazards and alter temperature–carbon interactions, which is discussed in Section 3.3.5.

Rising $CO_2$ emissions drive high temperature in the tropics and have the potential to hinder photosynthesis and vegetation growth, further discussed in Section 3.3.4. The changes in atmospheric circulation patterns might also influence the precipitation cycle, resulting in longer dry spells and increased fire risks with stomatal closure [18, 55]. The second-largest negative NBP extremes were experienced by arid and semi-arid regions with mostly grasslands (Figure 3.3(a)). Several studies conclude that soil moisture causes an increase in dry days and have a significant negative effect on the carbon cycle driven by increasing droughts in arid, semi-arid, and dry temperate regions [18, 68, 48]. The regions of South Africa, Central America, and Northern Australia witness the largest NBP extremes driven by fire. Extremes in the Amazon region were dominated by fire, soil moisture, and temperature in the 21$^{st}$ century. Reduction of fuel load by changing vegetation composition could likely be the reason for fewer fire-dominated regions later in the 21$^{st}$ century.

### 3.3.3 Compound Effect of Climate Drivers

The interactive effect of multiple climate drivers could lead to devastating ecological consequences as compound extremes often have a larger impact on the carbon cycle than the aggregate

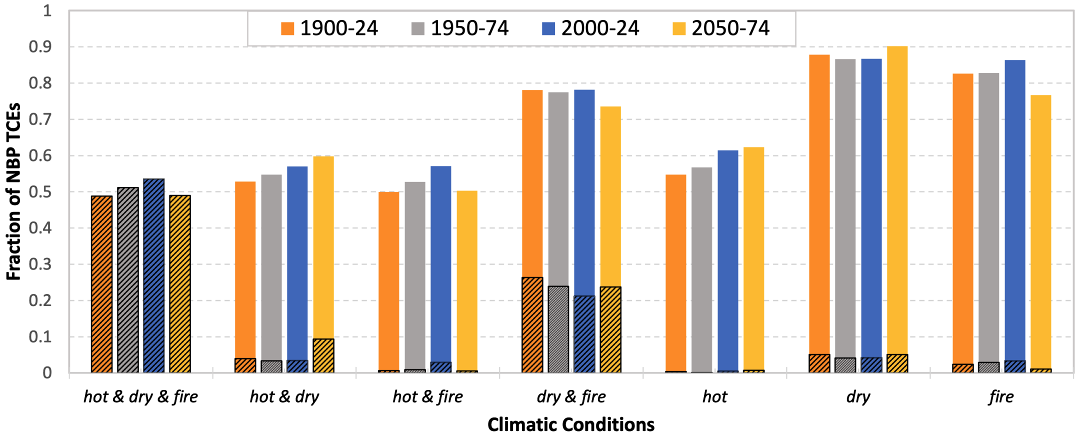

Figure 3.5: Fractional distribution of carbon cycle time-continuous extremes (TCEs) driven by compound climate drivers at lag of 1 month. The unhatched and hatched bars represent the mutually inclusive and exclusive compound and individual climate drivers, respectively. The exclusive climate drivers are always less than or equal to mutually inclusive drivers. The different colored bar represents following periods: 1900–24, 1950–74, 2000–24, and 2050–74 (*from left to right bar*). Most carbon cycle extremes are driven by interactive effect of climate drivers.

response of individual climate drivers [47, 65, 48]. We used three broad classes of climate drivers, namely, moisture (dry vs. wet), temperature (hot vs. cold), and fire to study their compound effect. At most grid cells, NBP extremes were either positively correlated with anomalous precipitation and/or soil moisture, and/or negatively correlated with temperature and/or fire. Figure 3.5 shows the compound climate drivers, both mutually exclusive and inclusive, that control NBP extremes over time. Mutually exclusive drivers are those climatic conditions that do not occur at the same time to cause an extreme event. When the drivers of an extreme are overlapping they are called mutually inclusive. For example, if an extreme is driven by both *hot* and *dry* conditions, the mutually exclusive climate driver is only *hot & dry* and the mutually inclusive drivers are *hot*, *dry*, and *hot & dry*.

The largest fraction, about 50%, of total NBP TCEs were attributed to the combined effect of *hot* & *dry* & *fire* events (Figure 3.5). This implies that every other large extreme event associated with anomalous loss in biospheric productivity was driven by the interactive effect of water limitation, hot days (heat waves), both of which together could trigger fire and rapid loss of carbon. The second strongest exclusive compound driver was *dry* & *fire*, causing about 25% of extremes. With increasing climate warming, the number of NBP extremes driven by hot and dry climatic conditions have increased, with about 10% extremes driven exclusively by *hot* & *dry* events during 2050–74.

Although the negative impact of water limitation (*dry*) on NBP extremes was the highest (driving inclusively about 90% of all NBP extremes), rising atmospheric $CO_2$ concentration and climate change led to an increasing number, 54% during 1900–24 to 62% during 2050–74, of NBP extremes driven inclusively by *hot* climatic conditions (Figure 3.5). For the same periods, extremes driven inclusively by *hot* & *dry* rose by 8%.

The effect of rising temperature on vegetation growth and carbon uptake is dependent on the geographical location. Pan et al. (2019) found that net ecosystem production had a negative sensitivity to warming across 81% of the global vegetated land area during 2007–18 and only the higher latitudes and Tibetan Plateau (TIB) had a positive sensitivity of NBP to temperature [48]. Similarly, Marcolla et al. (2020) found a positive sensitivity of NBP to air temperature in higher latitudes and negative sensitivity in the tropics [16]. Since the tropics have the largest standing biomass and high latitude regions have the largest stored carbon, understanding the contrasting impacts of climate change across these regions is important to understanding climate–carbon feedbacks. The next two sections will briefly discuss the changing characteristics of extremes in the tropics and at high latitudes.

### 3.3.4 Increasing temperature sensitivity and weakening terrestrial carbon sink across the tropics

Observation-based studies have reported a decline in the rate of carbon uptake in Amazonian forests, and similar declines in the African tropics are expected in the future [25]. Over long timescales, the rising atmospheric $CO_2$ concentration may not necessarily lead to an increase in plant biomass [72] as respiration losses outpace carbon uptake. Increasingly frequent and stronger heatwaves, droughts, and fires due to climate change are likely to cause the growth rate of NBP to flatten by the late 21st century (Figure B9). They may lead to an eventual reduction in total stored carbon and a potential reversal for tropical vegetation from a net carbon sink to a carbon source. Toward the end of the 21st century (2075–99), most of the SREX regions (23 of 26) were dominated by negative NBP extremes (Figure 3.3(b)), especially in the tropical regions (CAM, AMZ, NEB, WAF, EAF, SAF, SAS, SEA, and NAU) (Figure 3.2). During 2075–99, almost all tropical SREX regions (with the exception of NAU) were dominated by negative NBP extremes.

Rising temperatures and atmospheric $CO_2$ lead to an increasing trend for gross primary production (GPP) and net primary production (NPP) across most of the tropics. However, they are often also accompanied by increases in disturbance (such as droughts and fire), inducing plant mortality

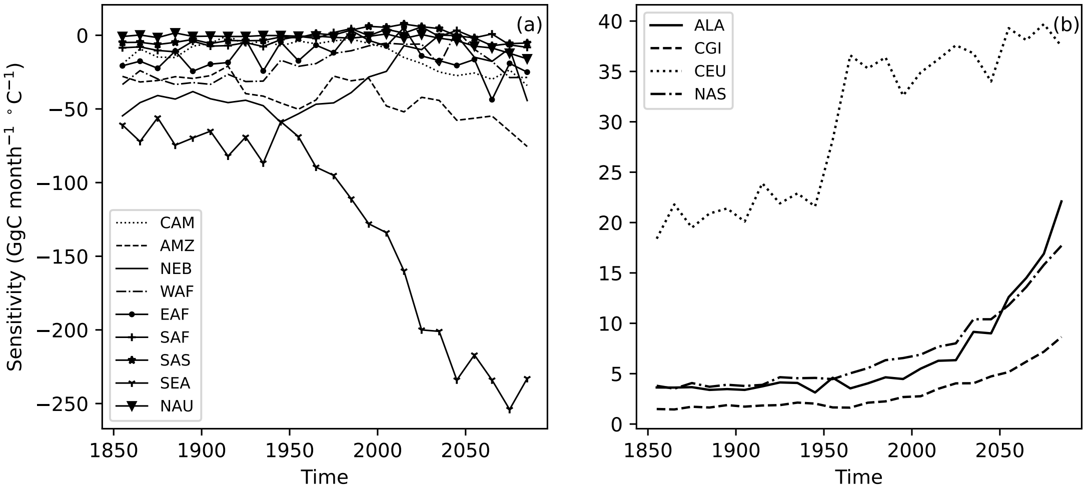

Figure 3.6: Changing temperature sensitivity of detrended anomalies in NBP to detrended anomalies in surface temperature for 10 year time periods at multiple SREX regions. The regions at low latitudes (a) have negative NBP sensitivity to temperature anomalies and high latitudes, and (b) have positive sensitivities.

and increases in heterotrophic respiration that contribute to significant quantities of negative carbon fluxes from the ecosystem. With the exception of AMZ and SEA that continued to witness an increase in NBP in the model simulation, most of the tropical regions showed a saturation or decline in NBP towards the end of 21$^{st}$ century (Figure B9). Analysis of temperature trends across tropical regions showed a significant trend towards warmer temperatures during warm (increase in 90$^{th}$ quantile) as well as cool (increase in 10$^{th}$ quantile) months of the year (Figure B7). Rising daily temperatures hinder net carbon uptake by enhancing stomatal closure and ecosystem respiration (Figure B9). The strength of 10 years of negative temperature sensitivity of NBP (see Section B1) increased over time (Figure 3.6(a)), suggesting an accelerated reduction in NBP growth with rising temperatures. The negative sensitivity values gradually increased from $-20$ GgC/month·°C to $-33$ GgC/month·°C for CAM, and $-30$ GgC/month·°C to $-70$ GgC/month·°C for AMZ during 1850–2100. South-East Asia (SEA) saw the highest negative temperature sensitivity of $-207$ GgC/month·°C by the end of 21$^{st}$ century. Similar patterns were seen in other tropical regions, suggesting an increasing negative temperature sensitivity of terrestrial ecosystem productivity to carbon uptake in a warming world (Figure 3.6(a)).

### 3.3.5 High latitude ecosystems can potentially become sources of carbon under warming climate

High latitude ecosystems store large amounts of carbon below ground and increasing exposure to warming and disturbance pose the risk of release of stored soil carbon [16] into the atmosphere. Warmer temperatures at high latitudes create favorable conditions for longer growing season, enhanced plant growth and overall increases in greening. All high latitude regions (ALA, CGI, CEU, NAS) showed a trend of positive and increasing NBP sensitivity to changes in air temperature (Section B1) over 1850–2100 (Figure 3.6).

While the overall impact of warming at high latitudes is expected to increase plant productivity and carbon uptake, high temperature anomalies increasingly induce negative NBP TCEs toward the end of the 21st century. The negative response of NBP to warm air temperature anomalies were found to occur most frequently during the summer months of July and August. For example, the 90th quantile temperature increased from 13°C by 8°C to 21°C in the NAS region while similar increases were observed for ALA, CGI and CEU (Figure B8(d)). With warming temperature trends, these periods of carbon losses in response to temperature extremes have an outsized impact on the overall carbon budget of high latitude ecosystems. Toward the end of the 21st century, CGI and NAS showed strong declines in NBP, becoming a net source of carbon.

The accelerated warming of winter temperatures have large consequences for respiration losses in the Arctic and Boreal regions [73, 74, 75]. Natali et al. (2019) found that the total carbon loss from wintertime respiration in the Arctic was 60% larger than the summer carbon uptake during 2003–17, driven primarily by higher soil and air temperatures. Contrary to in situ observations, which show significant $CO_2$ emissions at subzero temperatures, the current generation of process-based models shut off the respiration at subzero temperatures, thus underestimating the carbon losses during winters [73]. Simulation analyzed showed a 1.7 times higher increase in winter air temperature (10th quantile) compared to summer air temperature (90th quantile) at high latitudes (Figure B8). For example, in NAS, the 10th quantile temperature increased from $-25$°C during 1900–24 by 14°C to $-11$°C during 2075–99. The 90th quantile temperature increased from 13°C by 8°C to 21°C quantile over the same time period (Figure B8(d)). This enhanced rate of warming, especially during winter, resulted in rising winter and total ecosystem (autotrophic and heterotrophic) respiration, turning some regions to net sources of carbon (Figure B10).

The warming of warm and cold season temperatures induces a potential risk of losing a carbon sink and an accelerated release of stored carbon into the atmosphere. The increase in heterotrophic respiration is likely due to increased thaw of permafrost [76], a larger litter pool due to accelerated NPP, and longer warm season for higher microbial decomposition. As a result, the peak of NBP and NEP started to sharply decline towards the end of 21st century. The CGI region is expected to become a carbon source by the year 2100, and the NBP of the CEU region was gradually decreasing since 1975. The NAS region has shown a reduction in total NBP during 2075–2099, breaking the consistently increasing trend since 1850. With accelerated rising winter temperatures (Figure B8), declining NEP and NBP (Figure B10) and underestimation of respiration in the current process models, the losses in carbon uptake in the Arctic and at high latitudes in general are expected to be higher in the future.

## 3.4 Conclusions

The increasing frequency of climate change-driven extremes—such as fire, drought, and heatwaves—have the potential to cause large losses of carbon from terrestrial biomass and soils. The increasing frequency and magnitude of negative NBP extremes and saturation of NBP toward the end of the 21st century suggests that terrestrial ecosystems may increasingly lose the ability to sequester anthropogenic carbon and ameliorate the impact of climate extremes and change. Under a changing climate, parts of the globe are expected to experience enhanced vegetation growth and positive extremes in NBP; however, they are far outpaced by the frequency and intensity of negative extremes and associated losses in NBP. At the global scale, reductions in deforestation and enhanced $CO_2$ fertilization lead to an increase in NBP. The globally integrated NBP in the CESM2 reached a peak around 2070 and followed by a large decline toward the end of the 21st century. These losses in NBP were particularly large in the carbon-rich tropical region, followed by arid and semi-arid regions of the world. During 2075–99, 23 out of 26 SREX regions were dominated by negative NBP extreme events, especially in tropical regions. The increasing intensity and magnitude of negative extremes in NBP toward the end of the 21st century and beyond could lead to widespread declines in vegetation, loss of terrestrial carbon storage, and increasingly turn terrestrial ecosystems into a net source of carbon.

Extremes in the carbon cycle, driven by the extremes in environmental conditions, impact vegetation health and productivity. We analyzed anomalies in three primary environmental drivers (*hot, dry and fire*) of NBP extremes. Negative anomalies in soil moisture, causing widespread droughts and water stress in vegetation, were identified as the most dominant driver of negative NBP extremes, affecting almost half of the grid cells experiencing NBP extremes. The interactive and compounded impact of simultaneous anomalies in multiple drivers have especially large impacts on vegetation productivity, beyond the individual impacts of the variables. Extreme temperature anomalies compounded with dry conditions impact vegetation productivity, more than the sum of individual temperature and moisture anomalies. They also increase the risk and occurrence of fires. The compound effect of all three climate drivers (*hot, dry and fire*) cause the largest fraction of NBP TCEs.

In the tropics, the growth rate of NBP was decreasing, while the magnitude of negative extremes in NBP and the negative temperature sensitivity of NBP was strengthening over time. Large standing carbon stocks (fuel load) with hot and dry climate (fire weather conditions) increases the fire risk and potential loss of carbon stock during negative NBP extremes.

In the northern high latitudes, accelerated warming leads to permafrost thaw and release of belowground carbon, increasing the likelihood of reversal of the ecosystem to a net source of carbon over time.

This study analyzed climate-driven NBP extremes using an Earth system model simulation from 1850 to 2100. Future work should use multi-model analysis to evaluate the agreement among different Earth system models about the magnitude, frequency, and spatial distribution of NBP extremes and their attribution to individual and compound climate drivers. Longer-term simulations are needed to analyze the climate–carbon feedback post-2100, when the difference between the rate of $CO_2$ emissions and terrestrial carbon uptake is expected to increase.

# Chapter 4

# Investigating Variability in the Intensity, Direction, and Spatial Distribution of Carbon Cycle Extremes and Attribution to Climate Drivers Using Observations and CMIP6 Earth System Models.

## 4.1 Introduction

Terrestrial ecosystems have sequestered a quarter of the anthropogenic carbon emissions over the last decade [1]. However, the variability in the magnitude of carbon uptake is large [77, 78] and influenced by vegetation type, spatial location, and climate drivers [78, 5]. Climate extremes such as droughts, heatwaves, and fires have the potential to alter the carbon cycle by reducing the gross primary productivity (GPP), which is the total photosynthetic uptake of carbon [6]. Both the observations and models indicate that climate extremes are expected to increase with climate change. The increasing frequency and duration of climate extremes such as heatwaves and droughts and their compound occurences could a larger impact on carbon uptake than sum of individual impact of climate extremes [47]. Climate extremes increase the variability of the magnitude, duration, spatial distribution of carbon cycle anomalies, which is defined as the deviation from the expected carbon uptake. The key to understanding the adverse shifts in carbon uptake, i.e. very large GPP anomalies, it is essential to estimate the variability and direction of climate-carbon feedback.

With the availability of large amount (”big data”) of observation, we are better equipped than before to test the agreement among observations flux products and with Earth System Models (ESMs). Long-term goals in global ecology include understanding the multifaceted functions of terrestrial ecosystems in the Earth system [79]. Ecological-level quantities such as GPP are derived from flux and biometric observations are often comparable to ecophysical leaf-level quantities such as water-use efficiency, leaf conductance, light-use efficiency, or light-saturated photosynthetic $CO_2$ uptake [79]. Using statistical machine-learning methods using flux observations with remote sensing and metrological drivers has allowed us to infer site-to-global fluxes of ecosystem functions such as GPP [79]. These fields from up-scaled observations are used as benchmark data for evaluating the capability of ESMs in representing same carbon-cycle metrics [80]. These benchmarking efforts are inclined for evaluating the mean state of carbon fluxes and less importance is given to the tails of the probability distribution of the carbon fluxes. However, some tail events have the potential to change the state of climate-carbon feedbacks for much longer time; e.g. a large drought or heat wave or both can lead to drastic decline in GPP and will further lead to physiological and biogeochemical changes. Increase in the magnitude, frequency and duration of negative extremes in GPP could have adverse impact on biodiversity, natural ecosystem, agriculture (especially rain-fed) and terrestrial carbon uptake. Thus, a negative extreme in GPP represents a large loss in carbon uptake than expected, which could be associated with loss of vegetation productivity driven by fire, droughts, heatwaves, and/or insect infestations. In this chapter, we have focused on analysing the agreement of the characteristics of GPP, interannual annual variability (IAV) of GPP and GPP extremes among up-scaled grided observation products and ESMs.

The objectives of this study include, firstly, the quantification of the uncertainty within and among observations and models on the magnitude, frequency, and spatial distribution of GPP and IAV of GPP and negative extremes in GPP. Secondly, analysing the expected changes in the above mentioned characteristics of GPP extremes in the future SSP585 scenario. Lastly, attribution of negative carbon cycle extremes to individual and compound climate driver anomalies.

Most results are presented in the notation $\mu \pm \sigma$, where $\mu$ and $\sigma$ denotes mean and standard deviation, respectively.

## 4.2 Methods

### 4.2.1 Data

We used the observations-based GPP up-scaled data products and CMIP6 Earth System Model simulation outputs. Table C2 and Table C3 list the product names, data source websites, and the abbreviations that are used in this paper. The CMIP6 ESM simulation outputs were downloaded from the ESGF website. For attribution analysis using observational GPP, the meteorological data were used from reanalysis datasets of Global Soil Wetness Project Phase 3 (GSWP3) and ERA5. For attribution analysis using ESMs, the meteorological data from the respective ESMs were used.

FLUXCOM provides global gridded carbon fluxes from two experimental setups, one with only remote sensing ("RS") input drivers and other with RS and meteorological drivers ("RS+METEO"). The *FluxRS* data product represent the ensemble median of 18 members of up-scaled GPP products which vary in machine learning methods (e.g. Random forest (RF), Artificial Neural Network (ANN), Multivariate Adaptive Regression Splines (MARS), Model-Tree Ensemble (MTE), Kernel Ridge Regression (KRR), Support Vector Regression(SVR)) [81]. The fluxes in *FluxRS* are estimated only from Moderate Resolution Imaging Spectroradiometer (MODIS) satellite data. The *FluxRSMeteo* data product represent the ensemble median of 30 members of up-scaled GPP products which vary in machine learning methods (RF, ANN, and MARS) using mean seasonal cycle of satellite data and daily meteorological data, [81]. The meteorological data sources of *FluxRSMeteo* were GSWP3, CERES_GPCP, WFDEI, CRUJRA_v1, and ERA5. The *FluxANN* represents the up-scaled GPP based on "FLUXCOM RS+METEO" or *FluxRSMeteo* with CRUNCEPv6 climate and using ANN [82]. The *GOSIF* dataset is a global Solar-induced chlorophyll fluorescence (SIF) product based on discrete Orbiting Carbon Observatory-2 (OCO-2) SIF soundings, remote sensing data from the MODIS, and meteorological reanalysis data [83]. The resulting GPP product (are highly correlated with eddy covariance flux towers; $R^2$ = 0.73, p¡0.001) has a spatial and temporal resolution 0.05° and 8-day over 2000–17. The *FluxSat* dataset consist of GPP estimates based on models using satellite-based geometry-adjusted reflectances from MODIS (without meteorological inputs) and Level 3 (gridded) SIF derived from the Global Ozone Monitoring Experiment 2 (GOME-2) onboard the MetOp-A (GOME-2A). The GPP training model was calibrated with GPP estimates from eddy covariance flux towers and the resultant GPP was evaluated using an independent subset of FLUXNET 2015 GPP data. The GPP estimates from *FluxSat* are highly correlated with GPP estimates from GOSIF ($R^2$ = 0.98); similar comparison of IAV GPP yields $R^2$ =

0.84. The Water, Energy, and Carbon with Artificial Neural Networks,*WECANN*, estimates latent heat, sensible heat and GPP using ANN models with 6 inputs namely: GOME-2 SIF, net radiation, air temperature, soil moisture, precipitation, and snow water equivalent. The WECANN retrievals (at $1^\circ \times 1^\circ$ geographical grid and monthly resolution) were evaluated using eddy covariance tower estimates from the FLUXNET network across various climates and conditions [84]. For climate data we used precipitation and temperature from GSWP3 and ERA5. GSWP3 provides daily resolution observed climate data on a global $0.5^\circ \times 0.5^\circ$ from 1901 to 2010 [85]. ERA5 provides climate data at hourly and 30 km spatial grid [86].

### 4.2.2 Data Preparations

The spatial resolution of GOSIF and FluxSat was 0.05°, ERA5 was 0.1°, and FluxANN and GSWP3 was 0.5°. To have a consistent grid level attribution, the GOSIF and FluxSat were conservatively regridded, using tempestremap, to 0.1° and 0.5° for attribution with climate drivers from ERA5 and GSWP3, respectively. Climate variables from ERA5 were conservatively regridded to 0.5° spatial resolution for attribution analysis with carbon cycle extremes from FluxANN.

### 4.2.3 Calculation of Extreme Events

Any variation from an expected value of a variable is called an anomaly. We computed anomalies in GPP by subtracting the non-linear trend and modulated annual cycle from the time series of GPP at every grid cell [87]. Interannual variability of GPP is calculated by computing the standard deviation of detrended GPP time series [88]. Trend and modulated annual cycle were extracted from the time series of GPP by using singular spectral analysis [42]. Trend is computed by summing all signals that have a return period of 10 years or higher. Modulated annual cycle is composed of return periods of 12 months and harmonics. Therefore, the GPP anomalies comprise of intra-annual variability (periods $<$ 12 months) and interannual variability (12 months $<$ periods $<$ 10 years). To compute trend comprising of periods $\geq$ 10 years, the temporal duration of the data should be at least 20 years. Hence, only GOSIF, FluxSat, and FluxANN are selected for comparison of carbon cycle extremes with models. The common time period of GOSIF, FluxSat, and FluxANN is from the year 2001 to 2013 and the same period is selected for comparison of carbon cycle extremes with the CMIP6 models.

An extreme events occurs when the anomaly exceeds a certain threshold value. The negative and positive extremes in GPP, referred to as carbon negative and positive cycle extremes, are computed using percentile-based thresholds [40]. A threshold ($q$) is computed on the probability density function (pdf) of absolute negative and positive GPP anomalies of all non-zero GPP land grid cells, such that extremes represent only 10% of all GPP anomalies (for schematic representation, see Figure C4) . Therefore, the threshold value for calculation of GPP extremes is indifferent to the pdf of GPP anomalies. As a consequence, a threshold value, $q$ can be calculate such that negative anomalies in GPP are always $< -q$ and positive anomalies are $> q$.

The thresholds were computed by selecting 10th percentile anomalies in GPP for period 2001–13 and 2081–93. Using the singular spectral analysis [42], the trend (return period of 10 years and longer) and modulated annual cycle (return period of 12 months and harmonics) were calculated at every grid cell. Anomalies at every grid cell were calculated by subtracting trend and annual cycle from the time series of GPP. Hence, anomalies represent the frequencies with time period less than 12 months (intra-annual anomalies) and higher than 12 months but less then 10 years (inter-annual anomalies). The return period of ENSO events varies in the range of 2–7 years, so anomalies comprise of ENSO events.

The magnitude of negative carbon extremes is highly depended on the interannual variability (IAV) of GPP at that grid cell, which is defined as standard deviation of detrended GPP anomalies. The comparison of GPP IAV was done for both models and observations to investigate the hot spots of high agreement and disagreement. The data preparation for comparison of GPP among observation data products and models involves two basic steps. Firstly, all data products were regridded to a common 0.5° spatial resolution with monthly temporal resolution. Secondly, the time-period is chosen from 2007 to 2010 which is constrained by the availability of WECANN starting in 2007 and the corresponding end year of the FluxRSMeteo data product, i.e. 2010. The mean annual GPP values were calculated for all observation and model datasets. We report $R^2$ values are squared Pearson's Correlation Coefficients as a measure of agreement between two datasets on GPP distribution.

### 4.2.4 Attribution to Climate Drivers

We attributed negative carbon cycle to climate drivers by comparing the distribution of climate drivers anomalies at a grid cell during the negative carbon cycle extremes for the period 2001–13, such that if the median of the precipitation anomalies during the negative carbon cycle extremes at a grid cell is less than the 1$^{\text{st}}$ quantile of precipitation anomalies it is assumed that the negative carbon cycle extremes is driven by dry environmental conditions (see Figure C4 for schematic description).

The main advantage of this method is that it allows for attribution of negative carbon cycle extremes to either dry or wet and hot or cold conditions. Other most common method of attribution are linear or multi linear regression which have following drawbacks. If the assumed independent variables are partially correlated with each other, the coefficients of multi-linear regression equations could yield unreliable results. Using simple linear regression of dependent variable with each independent variable and comparison of resultant coefficients could be used to quantify relative importance of individual drivers. However, in order to get correlation coefficients with good significance values, one need to perform attribution on the combined time series of negative and positive extreme anomalies. Thus, one needs to further study the correlation coefficients to determine the direction of impact, e.g. if correlation coefficient of GPP and precipitation anomalies is greater than zero implies that anomalous drop in GPP is attributed to drop in precipitation.

The common period chosen for attribution of compound climate drivers, precipitation and surface temperature, among observation data and models is 2001–13. The spatio-temporal locations (mask) of negative carbon extremes were used to compute the median value of climate driver anomalies, $med_{\mathrm{dri-ext}}$, at every grid cell experiencing an extreme. The quartile values at 25th and 75th percentiles of driver anomalies, $dri_{\mathrm{q25}}$ and $dri_{\mathrm{q75}}$, were also calculated at every grid cell with extremes. The attribution of negative carbon cycle extreme to climate driver is determined by comparing $med_{\mathrm{dri\_du\_ext}}$ with $dri_{\mathrm{q25}}$ and $dri_{\mathrm{q75}}$. For example, if the 1$^{\mathrm{st}}$ quartile of precipitation anomalies are indicative of dry climatic condition and 4$^{\mathrm{th}}$ quartile of surface temperature represents hot climate, then :

- $med_{\mathrm{pr\_du\_ext}} < pr_{\mathrm{q25}}$ : represents extreme events driven by dry climate,
- $med_{\mathrm{tas\_du\_ext}} > tas_{\mathrm{q75}}$ : represents extreme events driven by hot climate, and
- $med_{\mathrm{pr\_du\_ext}} < pr_{\mathrm{q25}}$ & $med_{\mathrm{tas\_du\_ext}} > tas_{\mathrm{q75}}$: represents extremes driven by compound effect of hot and dry climate.

The impact of lagged effect of climate drivers on carbon cycle extremes is analyzed by comparing $med^{t:n}_{\mathrm{dri\_du\_ext}}$ with $dri^{0:n-t}_{\mathrm{q25}}$, where $t$ is the lag-months, $n$ is total months in time series and $t:n$ represents the range of values from $t^{th}$ to $n^{th}$ index, akin to python indexing.

The carbon cycle extremes could be driven by individual or compound climate drivers. When both hot and dry climatic conditions are fulfilled for attribution, it is referred to as negative extremes driven by compound climate drivers. We selected three observation GPP data products (GOSIF, FluxANN, and FluxSat) for attribution analysis with two observation climate data products

(GSWP3 and ERA5). Total precipitation and surface temperature were chosen as climate drivers causing negative carbon cycle extreme events. Similarly, six CMIP6 models were analyzed for attribution of negative carbon cycle extremes to precipitation and temperature. Additionally, attribution analysis was performed with soil moisture and surface temperature for CMIP6 models and included in Supplemantary Information Chapter 4. The median quantile distribution of climate drivers for the whole period and during extremes were compared to calculate the number of grid cells dominated by hot, cold, dry, wet, and hot & dry climatic conditions. The attribution analysis is dependent on the number of extremes in the grid cell and fewer number of extremes could give less meaningful results. Therefore, we report the attribution analysis using the grid cells that have total number of negative carbon cycle extremes more than the median of global count of negative extremes. The global aggregated results inform us of the most dominant climate driver(s) driving negative extremes but their spatial distribution could vary. We used the SREX regions (see Table C1) for to compute the relative distribution of hot and dry climate drivers across 26 regions.

## 4.3 Results

### 4.3.1 Comparison of Characteristics of GPP Extremes Among Observations and Models

During 2001–13, the distribution of total regional GPP among observations and models were consistent across most of the SREX regions (Figure 4.1a) with exception in the tropical regions, especially Amazon (AMZ), where GPP from observations was larger than models. The strong tropical carbon sink estimated by upscalled observation data is likely due to a combination of systematic biases in underlying eddy covariance data in tall tropical forests [81]. Among CMIP6 models, CanESM5 estimated the largest GPP across most regions. The global integrated timeseries of GPP was consistent among observations and models. The mean and standard deviation of GPP estimates from observations, 127 ± 10.8 PgC/year, were within the range of GPP from models, 128.5 ± 15.2 PgC/year (Figure C1).

The regional magnitudes of negative carbon cycle extremes among models were about three times larger than observations despite high consistency in regional and total GPP (Figure 4.1b). The difference in magnitude of losses in carbon uptakes in the regions of AMZ, Southeastern South America (SSA), Southeast Asia (SEA), and East, West and South Africa (EAS, WAF, SAF) between multi-model mean and multi-observation ranges from $-5$ to $-8$ PgC/month with large variability in

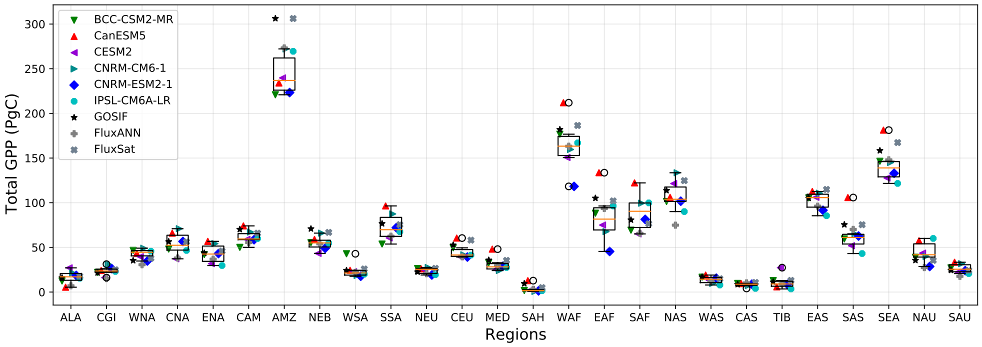

(a) Obs Models GPP comparison SREX

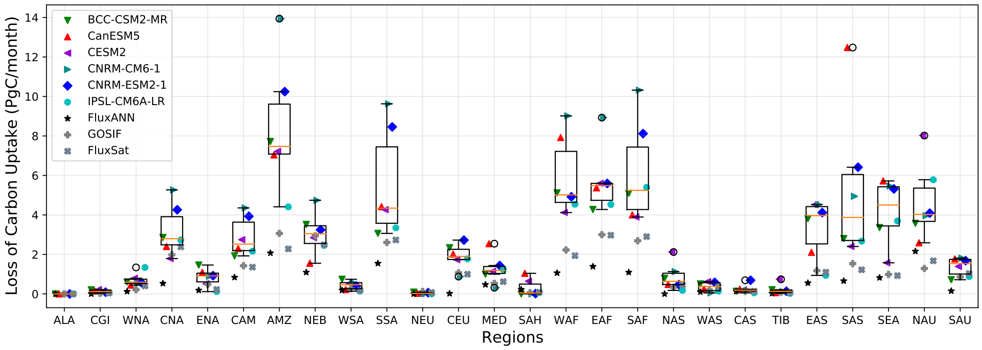

(b) Loss of carbon uptake

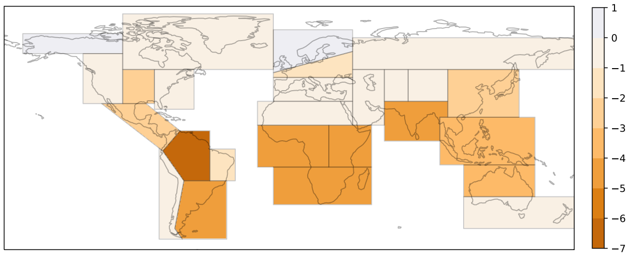

(c) Loss of carbon uptake, Models$_{mean}$ −Observations$_{mean}$

Figure 4.1: Spatial distribution of total regional GPP and loss of carbon uptake from observation data and model simulations for 2001–13. (a) Total regional GPP are calculated by integrating the GPP for the period 2001–13. The boxplots are created using only the total GPP values of only models, shown in colored markers, for each SREX region (Table C1). Total GPP from the observation data are plotted later (i.e. not considered for creating boxplots) and shown in different shades of grey. (b) Total loss of carbon uptake (PgC/month) during top 50 percent of the negative extremes in GPP for the period 2001–13. The boxplots are created using the total carbon loss values of only models, observations are plotted later. (c) Regional difference, Models$_{mean}$ − Observations$_{mean}$, in mean total loss of carbon uptake (PgC/month) among models and observations as shown in (b). The color range is from −9 to 9 PgC/month, the color bar ticker is shown for the range of regional data, for more details see Figure C2.

the regions of SEA, SSA, and Northeast Brazil (NEB). As a result, the disagreement in the magnitude of losses of carbon uptake ($L_{GPP}$) among models was much larger than observations (Figure 4.1b). The variation in the magnitude of $L_{GPP}$ and total GPP (and $L_{GPP}$ : *GPP*) was large which suggests that $L_{GPP}$ could increase or decrease disproportionately to the total regional GPP.

The disagreement among models on the magnitude of negative carbon cycle extremes was much higher than observations (Figure C2). The region of SAS showed highest standard deviation of total GPP of 3.5 PgC/month followed by AMZ (2.3 PgC/month) and SSA (2.2 PgC/month). The difference between magnitude of $L_{GPP}$ in models and observations highlight, 24 out of 26 regions, estimate much larger losses in carbon uptake in models (Figure C2e). The biggest disagreement was seen in tropical regions, especially in AMZ with $-7$ PgC/month.

The agreement between GOSIF and FluxSat on the regional distribution of frequency of negative carbon cycle extremes was higher than FluxANN (Figure C3). While the number of extremes estimated using FluxANN were larger in tropics than mid-latitudes, GOSIF and FluxSat estimated the opposite metrics. Among models, the agreement on frequency of negative carbon cycle extremes across regions was high. The negative extremes from the CESM2 and BCC-CSM2-MR were higher in northern mid-latitudes, NAS, Canada and Greenland (CGI), and fewer in tropics compared to the rest of the models (Figure C3). However, the agreement on the mean frequency of negative carbon extremes among observations and models is high except for NAS and CGI regions, where the standard deviation of frequency of extremes of observations is about two times larger than models. The observations (SEA, SAF, WAF, EAS, and NAU) and models (SEA, SAF, WAF, NAS, and EAS) agree on four of top five regions with largest frequency of negative extremes. The regions of SEA, SAF, and WAF represented about 14%, 10%, and 6% of total negative carbon cycle extremes among observations and models, respectively.

To understand the characteristics and distribution of negative carbon cycle extremes among observations and models, we compared the interannual variability (IAV) in GPP for each data product. The possible reason of larger magnitude of negative carbon cycle extremes estimated from model outputs than observations are likely due to larger magnitude of IAV in GPP in models (Figure 4.2) than observations (Figure 4.3). The regions with large IAV in GPP are also associated with high $L_{GPP}$ and vice versa. For example, CanESM5 estimated the largest $L_{GPP}$ in the region of Southern Asia (SAS, Figure 4.1b) and largest IAV in GPP in SAS (Figure 4.2). Similarly, CNRM-CM6-1 has the largest $L_{GPP}$ and largest IAV in GPP in the regions of Amazon (AMZ), West Africa (WAF), East Africa (EAF) and South Africa (SAF). CESM2 has the largest losses in carbon uptake and GPP IAV in Northern Australia (NAU) and lowest in Central North America (CNA), WAF and SAF. The

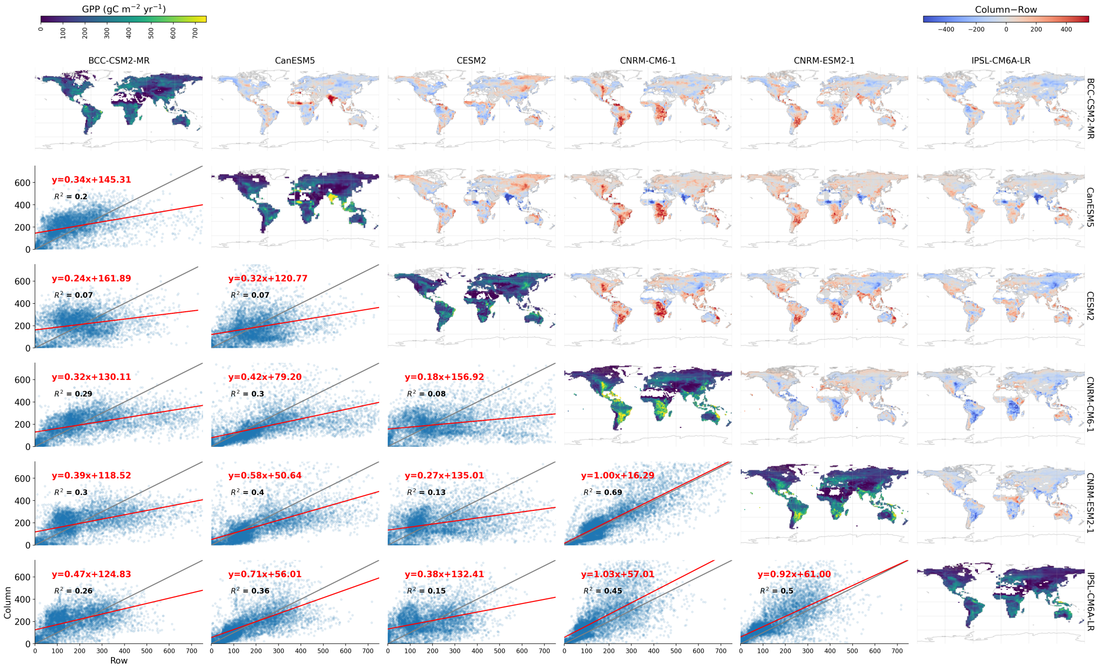

Figure 4.2: Comparison of interannual variability (IAV) of GPP, at 0.5° spatial resolution for the period 2001–2013, of 6 CMIP6 models. From left to right and top to bottom the order of models are BCC-CSM2-MR, CanESM5, CESM2, CNRM-CM6-1, CNRM-ESM2-1, and IPSL-CM6A-LR. The diagonal maps show the IAV GPP of every model. Maps above the diagonal show the difference of the IAV GPP of column dataset − row dataset. The plots below the diagonal show the point density in blue and 1:1 regression line in grey. Red line and equation represent the best fit line from total least-squares regression.

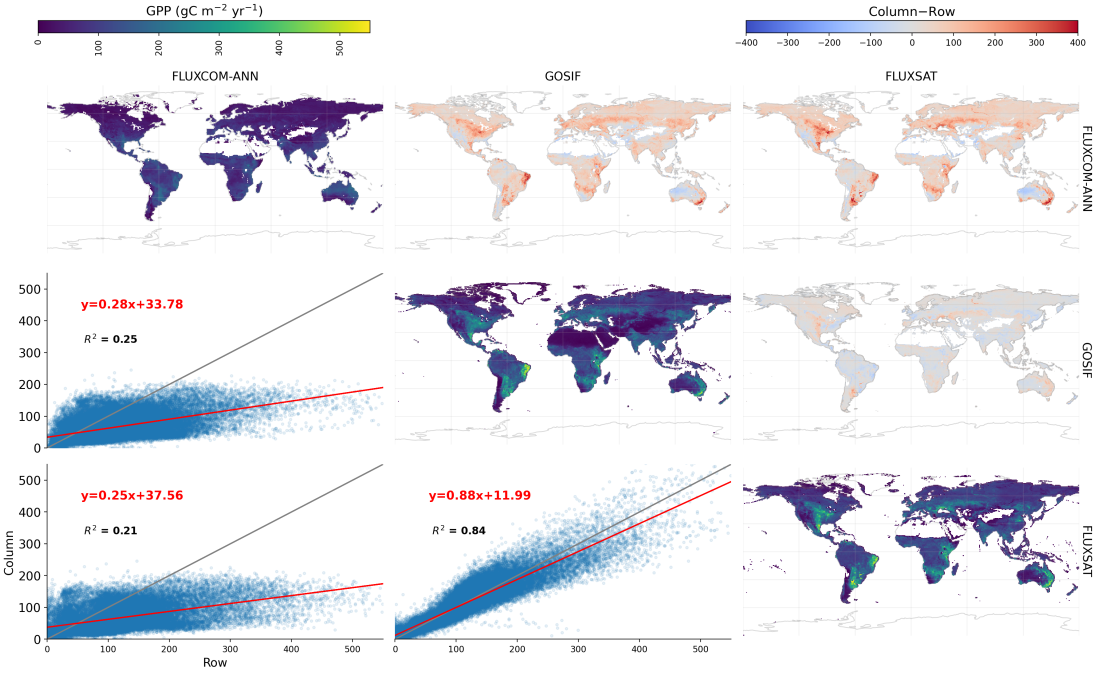

Figure 4.3: Comparison of interannual variability (IAV) of GPP, at 0.5° spatial resolution for the period 2001–2013, of 3 observation based upscaled GPP products. From left to right and top to bottom the order of models are FLUXCOM-ANN (FluxANN), GOSIF, and FLUXSAT (FluxSat). The diagonal maps show the IAV GPP of every dataset. Maps above the diagonal show the difference of the GPP of column dataset − row dataset. The plots below the diagonal show the point density in blue and 1:1 regression line in grey. Red line and equation represent the best fit line from total least-squares regression.

differences in the magnitude of IAV in GPP across regions and models were large and were likely the reason for large uncertainty in the characteristics of global and regional negative carbon cycle extremes. The disagreements among models on magnitude and spatial distribution are very high (Figure 4.2). Among the six models, BCC-CSM2-MR, CanESM5, and CESM2 showed the least consistent ($R^2 \leq 0.50$) distribution of IAV in GPP.

Similar patterns were seem in observation data products, where the losses in carbon uptake and GPP IAV are larger in FluxSat and GOSIF than FluxANN (Figure 4.3). The IAV in GPP in FluxANN was smaller than FluxSat and GOSIF, both of which possessed high consistency in comparing GPP IAV. The losses in carbon uptake among observations were also smaller than models likely due to low IAV in GPP among observations than models. Though the underestimation of IAV in GPP by observations is not fully clear [81], the likely reason is the low IAV simulated by machine learning models. Latter is likely driven by low temporal resolution of observations (8 day for MODIS), low sample size of eddy covariance (EC) sites in tropics and associated poor signal to noise, systematic errors of EC measurement, and errors of partitioning NEE to TER and GPP [81]. Improving the quality, standardization, and coverage of observation measurements will result in reduced uncertainties in the estimated carbon fluxes and better benchmark datasets for models' training and testing.

### 4.3.2 Changing Characteristics of GPP Extremes over time

All CMIP6 models showed an increase in total global GPP from the period 2001–13 (historical) to 2081–93 (ssp585), driven by increasing carbon fertilization and water use efficiency [89, 35, 90, 91]. The largest and smallest increase in GPP were shown by CanESM5 (63% or 1231 PgC) and IPSL-CM6A-LR (33% or 533 PgC), respectively (Figure 4.4d). The overall increase in GPP is also associated with large uncertainty (Figure 4.4c) and corresponding increase in IAV in GPP. Thus resulting in larger losses during negative carbon cycle extremes over time (Figure 4.5b and c) among all models and most regions. For the period of 2001–13, all observational datasets, except GOSIF and FluxSat, do not show any increase in total GPP (Figure C1). The cause of no-trend in GPP in FLUXCOM data products (and others) is due to lack of any treatment of $CO_2$ fertilization effect [81]. While the total GPP for the period 2001–13 for the models and observations are consistent (Figure 4.4d), the magnitude of negative carbon cycle extremes relative to total GPP is larger for models than observations (Figure 4.4b). This difference in the magnitude of negative carbon cycle extremes in models and observations is due to higher IAV in GPP in models than observations,

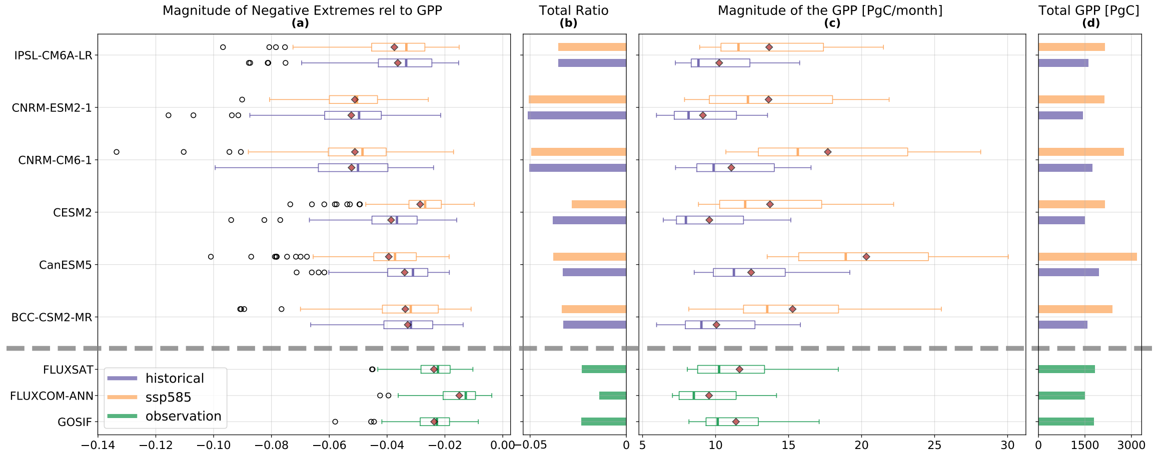

Figure 4.4: Change in the magnitude of negative carbon cycle extremes relative to GPP. The green, purple, and orange colors represent the statistics explained below for observation data (2001–13), historical model simulations (2001–13), and SSP585 model simulations (2081–93), respectively. Box plot of ratios of the monthly magnitude of negative carbon cycle extremes to total monthly GPP (a) and total monthly GPP (c) of observation data and model simulations. Ratio of total negative magnitude of negative extremes to to total GPP (b) and total GPP (d). The grey dashed line separates observations and models. Ratio of magnitude of negative extremes to total GPP is referred as $L : GPP$ (ratio) in the paper, which means loss in expected carbon uptake to total GPP.

which drives larger losses in carbon uptake during negative carbon cycle extremes in models than observations. The losses in carbon uptake ($L_{GPP}$) to total GPP, $L_{GPP}$:*GPP*, were associated with large variation for every dataset which highlight that changes in the monthly magnitude of negative extremes to total GPP are not proportional and may also be associated with larger carbon losses (shown in circle markers in Figure 4.4a).

The CNRM models have the largest $L_{GPP}$:*GPP* for both the historical and ssp585 periods, indicating highest losses in carbon uptake relative to total GPP. CNRM models also have the largest IAV in GPP (Figure 4.2) which strongly correlates with large anomalies in GPP and losses in carbon uptake. Despite varied increases in GPP among models, the $L_{GPP}$:*GPP* has been consistent for both periods which means that the negative carbon cycle extremes are expected to increase in proportion to the increase in GPP over time. The highest increase in $L_{GPP}$:*GPP* was shown by CanESM5 followed by BCC-CSM2-MR which depicts that the negative carbon cycle extremes will rise faster than the total increase in GPP. The rate of $L_{GPP}$:*GPP* of CanESM5 increased especially after 1950 and continued to further increase over time (see Figure C9 for details). The decreasing $L_{GPP}$:*GPP* in CESM2 suggests the the relative magnitude of negative carbon extremes to total GPP will decline over time. However, the magnitude of total negative carbon cycle extremes in CESM2 are expected to increase over time but at a slower rate than increase in GPP (Figure C8). Five out of six models depict that the changes in $L_{GPP}$:*GPP* from 2001–13 to 2081–93 are expected to remain consistent or increase with time.

The regional changes in GPP (Figure 4.5a) indicate that most regions are expected to witness an increase in total GPP from 2001–13 to 2081–93. The largest increase in GPP, based on multimodel mean GPP, is expected to occur in Amazon (AMZ) of about 85 ± 37 PgC, followed by East Asia (EAS) of about 75 ± 19 PgC. However, the uncertainty of GPP and IAV in GPP changes are large among the models. For the region of West Africa (WAF), CanESM5 estimates an increase of 170 PgC and CNRM-ESM2-1 a decrease of 20 PgC of total GPP (and standard deviation of 64 PgC). Similarly, the magnitude of negative carbon cycle extremes show large uncertainty and losses in carbon uptake show an increase overtime. Most regions and models that indicate an increase in losses in expected carbon uptake, predict GPP to increase over time which could help in compensating for the overall loss of vegetation during negative carbon cycle extreme events. A decrease in GPP has an opposite effect, such that the negative extremes weaken over time which is likely due to reduced IAV in GPP with reduction in GPP (e.g. NAU and CESM2 or SAF and CNRM-ESM2-1). The multimodel mean magnitude of negative carbon cycle extreme predicts an increase at most regions (Figure 4.5b,c). However, the spatial distribution of the change in the mean multimodel

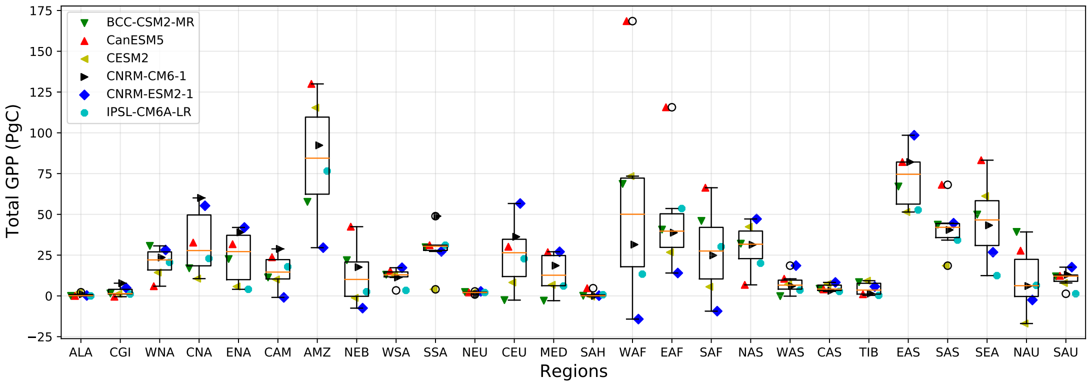

(a) Change in Magnitude of GPP (2081–93 $minus$ 2001–13)

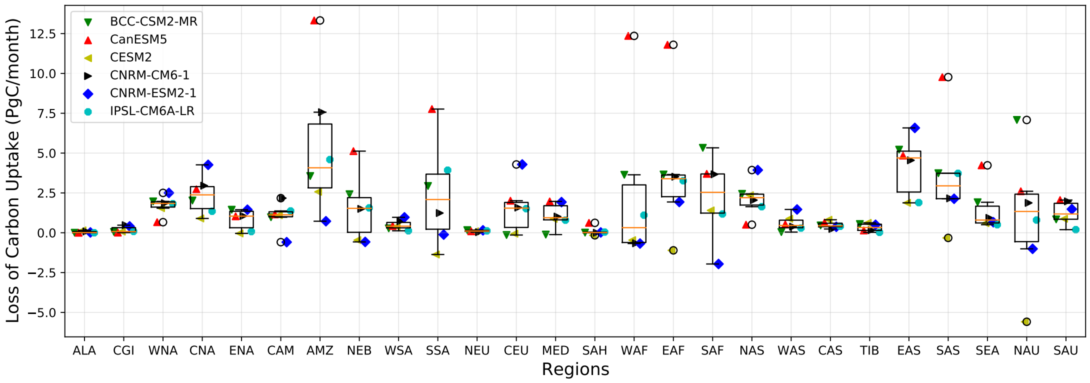

(b) Change in Magnitude of Negative Carbon Cycle Extremes (2081–93 $minus$ 2001–13)

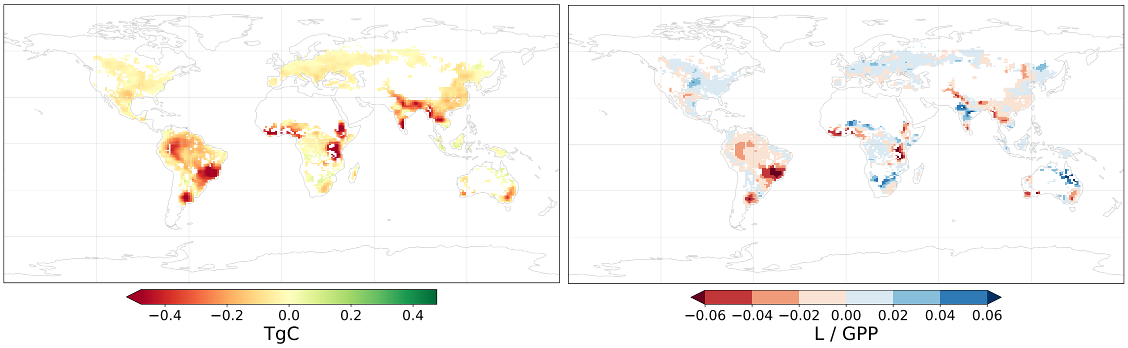

(c) $\Delta L_{GPP}$ (2081–93 $minus$ 2001–13)

(d) $\Delta$*L/GPP* (2081–93 $minus$ 2001–13)

Figure 4.5: (a) Total regional change in GPP is difference between total GPP of 2081–93 period and GPP of 2001–13 for each SREX region and model. (b) The total loss of carbon uptake ($L_{GPP}$) during top 50% of negative carbon cycle extremes is calculated for both periods. The regional change in $L_{GPP}$ is the difference between $L_{GPP}$ of 2081–93 and 2001–13, for each SREX region and models. (c and d) The spatial distribution of difference between the multimodel mean of $L_{GPP}$ and $L_{GPP}$*:GPP* for 2081–93 and 2001–13 shows strengthening of absolute negative carbon cycle extremes and relative to change in GPP over time, respectively.

$L_{GPP}$:*GPP* varies, suggesting that relative to increase in GPP, the proportion of the magnitude of negative extreme may increase or decrease over time (Figure 4.5d). Though the number of gridcells that show positive and negative $L_{GPP}$:*GPP* are similar, but total grid cells where $L_{GPP}$:*GPP* $< -0.04$ were more than twice the count of grid cells where $L_{GPP}$:*GPP* $> 0.04$. Thus, with more regions that are expected to witness higher losses in carbon uptake indicate an overall strengthening of negative carbon cycle extremes with respect to the change in GPP.

Figure 4.5: change in the magnitude of negative carbon extremes and total GPP

### 4.3.3 Attribution to Climate Drivers

Most negative carbon cycle extremes, 76% (± 3%) and 56% (± 5%), among GPP observational datasets were driven by *Dry* events using GSWP3 and ERA5, respectively (Figure 4.6a, c). Compound *Hot & Dry* events drives 8% (± 0.5%) and 19% (± 2.6%) of all negative carbon cycle extremes using GSWP3 and ERA5, respectively. Similarly, about 8.5% (± 1.5%) and 12% (± 1%) of all negative extremes were driven by *Hot* events using GSWP3 and ERA5, respectively. While the attributions of negative carbon cycle extremes to GSWP3 and ERA5 were consistent, the models showed a large uncertainty among drivers. The largest driver (62% ± 23%) of negative carbon cycle extremes among models was *Dry* climatic condition, except for CanESM5 where hot events caused most negative carbon cycle extremes (Figure 4.6e). *Hot* events and compound *Hot & Dry* events caused 17% (± 15%) and 13% (± 13%) of all negative carbon cycle extremes.

The spatial distribution of climate drivers of negative carbon cycle extremes (Figure C10) depicts that *Dry* and *Hot* events were dominant drivers across the globe. The regional distribution of gridcells from both observations and models suggests that majority of negative carbon cycle extremes occurred in tropical regions of SEA and SAF and driven by *Dry* events (Figure 4.6b,d, and f). Though, *Dry* events drive most negative carbon cycle extremes, the number of *Hot* events were larger than *Dry* events in the latitudinal range of $-23.27°$ to $23.27°$ for all except CNRM models. For example, the spatial distribution of climate drivers for CESM2 (Figure C10) show a larger number of hot events in the region of South Asia (SEA), Amazon (AMZ), North Eastern Brazil (NEB), and Central America (CAM) than dry events. The stark differences in the regional distribution of magnitude (Figure 4.1b) and frequency (Figure 4.6b,d, and f) of negative carbon cycle extremes indicate that either small number of extremes (e.g. AMZ, SSA) could cause large losses in most tropical regions or many negative extremes in tropical regions or most negative extremes in tropics occur even during 2nd and 3rd quartile of precipitation and temperature anomalies. The occurrence

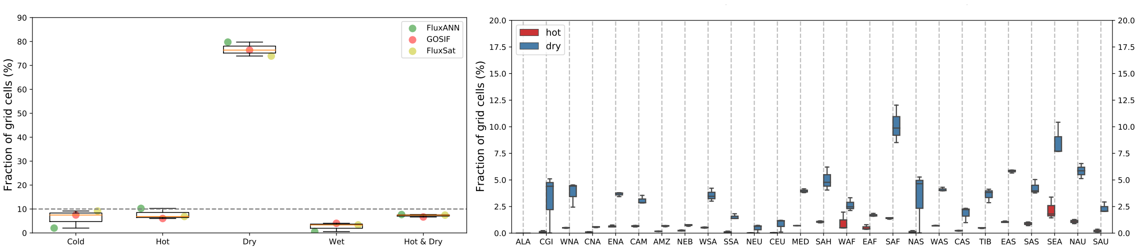

(a) Global, GSWP3 (b) Regional, GSWP3

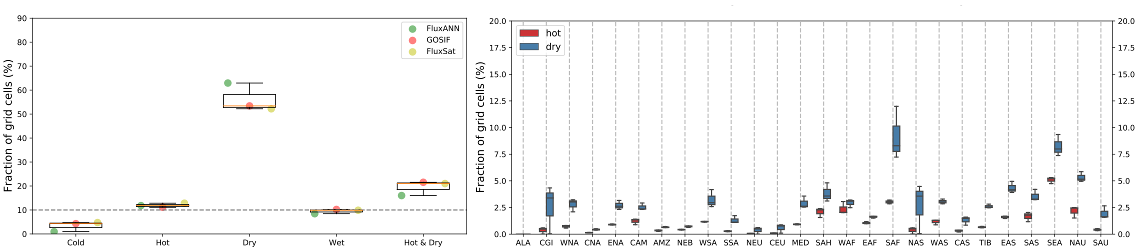

(c) Global, ERA5 (d) Regional, ERA5

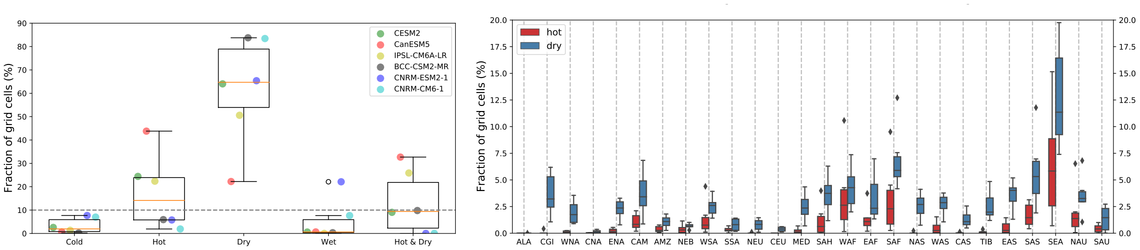

(e) Global, CMIP6 Models (f) Regional, CMIP6 Models

Figure 4.6: Global and regional distribution of climate drivers of negative carbon cycle extremes. The left panel (a, c, and e) shows fraction of grid cells where negative carbon cycle extremes are driven by exclusive individual and compound climate drivers aggregated globally. The right panel (b, d, and f) shows the fraction of grid cells driven either by hot (shown in red) or dry (shown in blue) events across 26 SREX regions. The attribution of negative carbon cycle extremes from observation flux data was performed with two observation based climate data, i.e. GSWP3 (a, b) and ERA5 (c, d). The attribution of negative carbon cycle extremes from CMIP6 models was performed with their own climate drivers (e, f). Cold and wet conditions rarely drive a negative carbon cycle extreme event as they lie below the horizontal dashed line at 10%.

of large negative carbon cycle extremes during the non-extremes of climate drivers is consistent with the earlier findings [18, 31] and such negative carbon extremes are likely driven by compound effect of non-extreme climate drivers.

The terrestrial ecosystem has an ingrained capacity to buffer and push back the effects of climate change which results in delayed response of climate extremes on vegetation productivity [46]. Using the CMIP6 models, we show the impact of no-lag and 1 month lagged response of hot and dry events on negative carbon cycle extremes. First quartile of precipitation (*Dry-pr*) and soil moisture (*Dry-sm*) anomalies were used to define dry events. The uncertainty of relative attribution to *Hot* and *Dry-sm* events was less among the models than *Hot* and *Dry-pr* events (Figure C11). The percent of negative carbon cycle extremes attributed to *Hot* and *Dry-pr* events at no-lag were 28.8% (± 17.4%) and 35.3% (± 21.7%), and at 1 month lag were 17.5% (± 15.8%) and 61% (± 22.8%), which shows that lagged of water scarcity caused higher losses in carbon uptake. Total percent of negative carbon cycle extremes driven by *Hot*, *Dry-sm*, and compound *Hot & Dry-sm* were 8.8% (± 8.4%), 56% (± 12.6%), and 22.8% (± 16.6%) for no lag and 5.4% (± 4.5%), 63.8% (± 12.1%), and 18.2% (± 17.2%) for 1 month lag, respectively. The percent of negative carbon extremes in CanESM5 attributed to *Dry-sm* were larger than both *Hot* and *Dry-pr*. Consistent and increased attribution of negative extremes to decline in soil water content depicts that lack of soil moisture impairs the vegetation productivity strongly than precipitation. Attribution of negative carbon cycle extremes to *Cold* and *Wet* events were $\leq 10\%$ among both models and observations.

## 4.4 Discussion

While global mean GPP values from observation estimates and model outputs are consistent, the disagreement on GPP at spatial resolution is large, especially among models. The uncertainty in the GPP estimates among CMIP6 ESMs is about 1.5 times than of observations for the period 2001-13. The mean GPP of the FluxRSMetro (132.97 PgC/year) was 10% more than FluxRS (121.69 PgC/year), which is similar to the finding of [81], largely due to differences in the tropics. The difference in GPP in FluxRS and FluxRSMeteo is not likely because of FluxRS only dependence on remote sensing, rather related to different predictor sets and machine learning methods, which requires more investigation [81]. Carbon flux trends of FLUXCOM datasets are likely unrealistic since it does not account for $CO_2$ fertilization effects.

The order of dominance of regional magnitude of negative carbon cycle extremes and regional GPP were not consistent. The patterns of losses in carbon uptake and IAV in GPP suggests that the largest negative extremes in the carbon cycle anomalies are highly dependent on the magnitude of IAV in GPP. Since IAV is based on detrended GPP time series and anomalies are calculated by removing seasonality from detrended anomalies, high correlation between the regional IAV and extremes, suggests that seasonality of GPP has minimal effect on the magnitude of carbon cycle extremes. This suggests that spatial patterns of negative carbon extremes are dominated by detrended anomalies and not seasonality and total GPP.

The AMZ showed the largest regional magnitude of negative carbon cycle extremes for models and observations. However, SEA showed maximum frequency (14%) of negative carbon cycle extremes for both models and observations. Despite less than 1% of all negative extremes occurred in the AMZ, the total losses in carbon uptake were highest in the AMZ. Large losses represented in AMZ were due to high IAV in GPP in the AMZ which is highly correlated with total regional GPP, which is highest for the region of AMZ. Thus, a few large negative carbon cycle extremes represented most of the IAV in carbon cycle.Moreover, the magnitude of negative carbon cycle extremes of observations were smaller than of models. One reason of low variance of IAV in observed data products could be due to low resolution of time input in the machine learning model [81]. Other machine learning methods can be applied which benefit from higher temporal variability by using high frequency remote sensing measurements.

Most CMIP6 models show similar magnitude of $L_{GPP}$:*GPP* for historical and SSP585 periods, indicating that increase in magnitude of negative carbon cycle extremes will be proportional to increase in GPP. This also suggests that the increases IAV in GPP in the future will most likely increase proportional to increase in GPP. While CESM2 suggests that $L_{GPP}$:*GPP* will decrease, CanESM5 and BCC-CSM2-MR show an increase in $L_{GPP}$:*GPP* over time. However, the uncertainties in the magnitude of regional changes in GPP and IAV of GPP are very large and require us to improve climate-carbon modelling and observations on how carbon uptake of terrestrial vegetation is affectted by $CO_2$ enrichment of the atmosphere, and what are the feedbacks from the vegetation to the atmosphere. The changes in $L_{GPP}$:*GPP* from historical to SSP585 periods show a larger number of gridcells with strengthening of negative carbon extremes, losses $\geq$4% of GPP, than weakening of negative carbon extremes. Stonger negative carbon cycle extremes could adversely impact terrestrial ecosystems, wildlife, and unirrigated croplands.

## 4.5 Conclusions

With increasing human activities due to fossil fuel emissions and land use and land cover changes, the carbon emissions have been increasing for decades. While the total carbon uptake by land and ocean was more than 50%, the rest of the carbon emissions have caused an increase in the atmospheric carbon dioxide concentration. This increased atmospheric $CO_2$ has resulted in increased vegetation productivity due to $CO_2$ fertilization and rising water use efficiency. Since more than a quarter of carbon emissions are taken up terrestrial ecosystems, further increases in negative carbon cycle extremes could lead to reduction of expected carbon uptake which have a negative feedback on climate change.

We found that the uncertainty in the quantification of GPP by multiple models (15%) was higher than multiple observations (8.5%). Thought the mean GPP among multi-observations and multi-models was consistent, the uncertainty of the interannual variability of GPP among multi-observations and multi-models was much larger. Even the agreement among multiple observations on the interannual variability of GPP was very poor which poses a larger question on the reliability of the benchmark datasets that are used to train the models. The magnitude of negative extremes in GPP was about 3 times higher among models than observations. While the GPP is increasing over time, most models indicate that the rate of increase of the magnitude of negative extremes ($L$) in GPP are expected to be proportional or larger than in rate of increase of GPP, globally. The regions that show a weakening of negative extremes in GPP often witness a decline in total GPP (e.g. Sahel and Northern Australia), thus lower vegetation productivity most likely causing reduced variance of GPP.

Both observations and models agree that the largest driver of negative carbon cycle extremes is water scarcity driven reduced soil moisture and precipitation. The compound effect of dry and hot events drive the second largest proportion of negative carbon cycle extremes. The hot temperature have the largest impact in the tropical regions of South America and South Asia, while dry events drive most of the extremes in arid and semi-arid regions. Moreover, at the lag of 1 month the proportion of negative carbon cycle extremes driven by dry events were higher than no-lag response, which implies that vegetation have a buffer and capacity to push back the effects of climate drivers (e.g. water scarcity).

# Chapter 5

# Conclusions and Future Work

The extremes in the carbon cycle poses a concern not only for future carbon sink capacity but also for contemporary natural ecosystems, wildlife, and food security. The main questions addressed in the thesis were (a) what was the impact of increasing anthropogenic $CO_2$ emissions on the anomalies in carbon cycle?, (b) what were the climatic drivers of large anomalous losses in terrestrial carbon uptake?, (c) how would land use and land cover change affect the climate drivers and carbon cycle (extremes) drivers in the terrestrial ecosystems?, and (d) what were the (un)certainties in the quantification of characteristics of carbon cycle extremes and their drivers among Earth system models and observations? In this dissertation research, I conducted a comprehensive study of carbon cycle extremes using multiple carbon fluxes, under multiple climate change scenarios by leveraging multiple observational datasets and multiple ESMs. Analysis highlighted a large variability in the frequency, magnitude, and regional distribution of both negative and positive carbon cycle extremes. A few large negative and positive extremes in GPP - especially in tropical regions - represented most of the global interannual variability in GPP. Both observations and ESMs showed an increasing trend in magnitude and frequency of both negative and positive extremes in carbon cycle, with negative extremes outnumbering the positives.

Land use and land cover changes (LULCC) cause a reduction of total global GPP, but increase the interannual variability of GPP, at a rate of 2.6× larger than without LULCC forcing. This increased IAV in GPP with LULCC forcing was consistent with larger losses of carbon uptake during GPP extremes with LULCC forcing.

Both observations and ESMs identifies Amazon region to experience the largest loss of carbon during carbon cycle extremes. However, there were large disagreements and uncertainties among observations and ESMs on the magnitude and frequency of such carbon cycle extremes. It is expected that the westwards low-level jets will carry evaporative water from the Northeastern and Eastern Amazon towards the Andes and cause an increase in GPP near the Andes (with low interannual variability) and reduction in GPP in the Northeastern Amazon. Thus, resulting in the weakening of negative carbon cycle extremes over time in the Northeastern Amazon and near the Andes due to vegetation die-back and benign growing climatic conditions with low interannual variability, respectively. Most regions across the globe showed a large increase in GPP and GPP extremes. I also investigated the changing temperature–NBP sensitivity across 26 SREX regions and found that the temperature sensitivity of NBP was negative and expected to get more negative in the tropics and was positive in high latitudes and expected to be more positive through the 21st century. While the overall impact of warming at high latitudes is expected to increase plant productivity and carbon uptake, high temperature anomalies increasingly induce negative NBP TCEs toward the end of the 21st century. This is especially concerning since most process-based models underestimate the respiration losses and the negative temperature–NBP feedback in the future raises concerns about viability of summer sink in the high latitudes.

The climate–carbon feedbacks are complex and ecosystems have ingrained plasticity to absorb sudden changes in climate, hence the attribution analysis considered impact of antecedent climate drivers on carbon cycle extremes. Negative soil moisture anomalies were the largest drivers of negative carbon cycle extremes. The regions that were impacted the most by negative carbon cycle extremes include arid and semi-arid regions. While soil moisture controls for how long an extreme persists, often the lack of precipitation triggered a negative carbon cycle extreme. Over time, the dominance of fire increased and it emerged as the second largest dominant climate driver. Although hot temperatures showed high dominance in the tropical regions. The continued rising mean surface temperatures are expected to increase the occurrence of heatwaves and that could have larger impact on vegetation. The interactive effect of multiple climate drivers causes significantly larger impact on ecosystems than any single climate driver. I found that the compound effect of hot, dry, and fire conditions caused more than 50% of extremes at any period, which was more than any single climate driver.

With increasing human activities due to fossil fuel emissions and land use and land cover changes, the carbon emissions have been increasing at an unprecedented rate. While the total carbon uptake by land and ocean was more than 50%, the rest of the carbon emissions have caused an increase in the atmospheric carbon dioxide concentration. This increased atmospheric $CO_2$ has resulted in increased vegetation productivity due to $CO_2$ fertilization and rising water use efficiency. However, most CMIP6 ESMs suggest that rate of increase of frequency of negative carbon cycle extremes and losses of carbon during carbon extremes are expected to grow faster than the total photosynthetic uptake. The net biospheric production is expected to flatten before the end of the 21$^{st}$ century. Further increases in negative carbon cycle extremes could lead to reduction of expected carbon uptake which have a negative feedback on climate change. This research provides new insights into the contribution of human activities in altering carbon cycle extremes and the vulnerability of terrestrial vegetation and associated ecosystem services that could present increasing risks to human lives, wildlife, and food security.

## Next Steps

This thesis presented detailed analysis of global carbon cycle extremes at both global and regional scales. As a consequence of the scope of carbon cycle extremes, high productive plant functional types (PFTs) such as broad-leaf forests were represented more and other PFTs with less vegetation productivity were less represented. Due to this caveat in the definition of carbon cycle extremes, extremes in the high and mid latitudes were under represented. We performed PFT-specific analysis of carbon cycle extremes and found that the magnitude of carbon cycle extremes of a few PFTs was significantly larger (and smaller) than the mean magnitude of global extremes. Further work is needed to identify the changes in the characteristics of the PFT-specific extremes in carbon cycle over time and attribution of these extremes to climate drivers.

In this thesis, I defined time continuous extreme events, where an extreme event could have long time contiguity if other extremes occur within a season length. Since carbon cycle extreme events could be contiguous across space and time [92, 21], the characteristics of spatio-temporal contiguous and non-contiguous extremes should be analyzed to understand the relationship between IAV in carbon cycle and spatio-temporal extreme events. Similarly, the attribution analysis could be performed based on the representative climatic condition per spatio-temporal contiguous extreme. This question will investigate whether attributions are consistent across grid cells to spatio-temporal contiguous manifolds.

There are several approaches to attribute (compound) climate drivers to carbon cycle extremes. I explored two such approaches in my thesis, 1) linear regression of climate driver anomalies with carbon cycle time continuous extreme events and 2) comparison of climatic conditions during carbon cycle extremes with extreme climatic conditions at that location. The future work could consider using attribution analysis using the Granger causality test, which tests the hypothesis if a time series $X$ forecasts time series $Y$ through a series of t-tests. The Granger causality test could be tested to investigate if the lagged response of anomalies in climate drivers forecasts anomalies in carbon cycle and vice versa. This approach is popular for causality analysis due to computational simplicity [93].

## Future Opportunities

In this dissertation research, only a few grid cells showed a significant correlations between wet climatic conditions (such as floods or heavy precipitation) with negative carbon cycle extremes. This is most likely due to limitations of ESMs to capture such feedbacks. Further analysis is needed to synthesize datasets that will allow for an investigation of the compound effects of abiotic (droughts, floods, wildfire, frost), and biotic (insects, pests) stressors on carbon cycle extremes.

The ESMs intercomparison and benchmarking projects such as International Land Model Benchmarking (ILAMB) focus on the evaluation of ESMs based on averages and annual cycles. Very little attention is paid to metrics on interannual variability and extreme events. A model with a high benchmarking score based on annual averages may not perform well when compared to the metrics of extremes. The projects like ILAMB should be expanded to include metrics that compare the characteristics of extremes among ESMs and observations. It is equally important to identify the best observation datasets; as I showed in Chapter 4 that a large disagreement exists among different GPP observation datasets on annual GPP, it's interannual variability, and characteristics of extreme events.

While the ESMs show large interannual variability (IAV) in GPP, observation-based datasets have less variability. One reason for the low variance of IAV in GPP in observed data products could be due to the low resolution of time input in the machine learning model [81]. Other machine learning methods should be tested which benefit from higher temporal variability by using high-frequency remote sensing measurements. I also found large disagreements in the characteristics of GPP extremes in the tropics, especially in the Amazon. This suggests that more observations are needed in the tropical ecosystems to represent the diversity in the vegetation at both the canopy and understory, which is often not captured by remote sensing satellites. The temperature sensitivity is negative and positive in low and high latitudes. The mid-latitudes, especially the temperate and semi-arid regions have very varied climate-carbon feedbacks. More observations at multiple locations can help the community to understand vegetation response to changes in temperature. The data from Free-Air Carbon dioxide Enrichment (FACE) projects can provide us with valuable information on potential changes in the biogeochemical feedback. These data need to be thoroughly investigated to identify anomalies in the expected process based understanding and improving the representation of such processes in the models. Improved representation of vegetation physiology is needed in the models to capture the vegetation response to stress in diverse and heterogeneous ecosystems. Parameter perturbation experiments can help one develop insights into which processes are to be improved.

# Bibliography

[1] P. Friedlingstein, M. W. Jones, M. O'Sullivan, R. M. Andrew, D. C. E. Bakker, J. Hauck, C. Le Quéré, G. P. Peters, W. Peters, J. Pongratz, S. Sitch, J. G. Canadell, P. Ciais, R. B. Jackson, S. R. Alin, P. Anthoni, N. R. Bates, M. Becker, N. Bellouin, L. Bopp, T. T. T. Chau, F. Chevallier, L. P. Chini, M. Cronin, K. I. Currie, B. Decharme, L. M. Djeutchouang, X. Dou, W. Evans, R. A. Feely, L. Feng, T. Gasser, D. Gilfillan, T. Gkritzalis, G. Grassi, L. Gregor, N. Gruber, O. Gürses, I. Harris, R. A. Houghton, G. C. Hurtt, Y. Iida, T. Ilyina, I. T. Luijkx, A. Jain, S. D. Jones, E. Kato, D. Kennedy, K. Klein Goldewijk, J. Knauer, J. I. Korsbakken, A. Körtzinger, P. Landschützer, S. K. Lauvset, N. Lefèvre, S. Lienert, J. Liu, G. Marland, P. C. McGuire, J. R. Melton, D. R. Munro, J. E. M. S. Nabel, S.-I. Nakaoka, Y. Niwa, T. Ono, D. Pierrot, B. Poulter, G. Rehder, L. Resplandy, E. Robertson, C. Rödenbeck, T. M. Rosan, J. Schwinger, C. Schwingshackl, R. Séférian, A. J. Sutton, C. Sweeney, T. Tanhua, P. P. Tans, H. Tian, B. Tilbrook, F. Tubiello, G. R. van der Werf, N. Vuichard, C. Wada, R. Wanninkhof, A. J. Watson, D. Willis, A. J. Wiltshire, W. Yuan, C. Yue, X. Yue, S. Zaehle, and J. Zeng, "Global carbon budget 2021," *Earth System Science Data*, vol. 14, no. 4, pp. 1917–2005, 2022.

[2] P. Friedlingstein, M. Jones, M. O'sullivan, R. Andrew, J. Hauck, G. Peters, W. Peters, J. Pongratz, S. Sitch, C. Le Quéré *et al.*, "Global carbon budget 2019," *Earth System Science Data*, vol. 11, no. 4, pp. 1783–1838, 2019.

[3] C. Le Quéré, R. M. Andrew, P. Friedlingstein, S. Sitch, J. Hauck, J. Pongratz, P. A. Pickers, J. I. Korsbakken, G. P. Peters, J. G. Canadell, A. Arneth, V. K. Arora, L. Barbero, A. Bastos, L. Bopp, F. Chevallier, L. P. Chini, P. Ciais, S. C. Doney, T. Gkritzalis, D. S. Goll, I. Harris, V. Haverd, F. M. Hoffman, M. Hoppema, R. A. Houghton, G. Hurtt, T. Ilyina, A. K. Jain, T. Johannessen, C. D. Jones, E. Kato, R. F. Keeling, K. K. Goldewijk, P. Landschützer, N. Lefèvre, S. Lienert, Z. Liu, D. Lombardozzi, N. Metzl, D. R. Munro, J. E. M. S. Nabel, S.-I. Nakaoka, C. Neill, A. Olsen, T. Ono, P. Patra, A. Peregon, W. Peters, P. Peylin, B. Pfeil, D. Pierrot, B. Poulter,

G. Rehder, L. Resplandy, E. Robertson, M. Rocher, C. Rödenbeck, U. Schuster, J. Schwinger, R. Séférian, I. Skjelvan, T. Steinhoff, A. Sutton, P. P. Tans, H. Tian, B. Tilbrook, F. N. Tubiello, I. T. van der Laan-Luijkx, G. R. van der Werf, N. Viovy, A. P. Walker, A. J. Wiltshire, R. Wright, S. Zaehle, and B. Zheng, "Global carbon budget 2018," *Earth System Science Data*, vol. 10, no. 4, pp. 2141–2194, 2018.

[4] G. B. Bonan, R. S. DeFries, M. T. Coe, and D. S. Ojima, "Land use and climate," in *Land change science. Remote Sensing and Digital Image Processing*. Springer, 2012, vol. 6, pp. 301–314.

[5] G. Bonan, *Ecological Climatology: Concepts and Applications*, 3rd ed. Cambridge University Press, 2015.

[6] M. Reichstein, M. Bahn, P. Ciais, D. Frank, M. D. Mahecha, S. I. Seneviratne, J. Zscheischler, C. Beer, N. Buchmann, D. C. Frank, D. Papale, A. Rammig, P. Smith, K. Thonicke, M. van der Velde, S. Vicca, A. Walz, and M. Wattenbach, "Climate extremes and the carbon cycle," *Nature*, vol. 500, no. 7462, pp. 287–295, 2013.

[7] J. Sillmann, V. V. Kharin, F. W. Zwiers, X. Zhang, and D. Bronaugh, "Climate extremes indices in the cmip5 multimodel ensemble: Part 2. future climate projections," *Journal of Geophysical Research: Atmospheres*, vol. 118, no. 6, pp. 2473–2493, 2013.

[8] J. Lehmann, D. Coumou, and K. Frieler, "Increased record-breaking precipitation events under global warming," *Climatic Change*, vol. 132, no. 4, pp. 501–515, 2015.

[9] J. Yin, P. Gentine, S. Zhou, S. C. Sullivan, R. Wang, Y. Zhang, and S. Guo, "Large increase in global storm runoff extremes driven by climate and anthropogenic changes," *Nature Communications*, vol. 9, no. 1, pp. 1–10, 2018.

[10] D. Gampe, J. Zscheischler, M. Reichstein, M. O'Sullivan, W. K. Smith, S. Sitch, and W. Buermann, "Increasing impact of warm droughts on northern ecosystem productivity over recent decades," *Nature Climate Change*, vol. 11, pp. 772–779, 2021.

[11] P. Friedlingstein, P. Cox, R. Betts, L. Bopp, W. von Bloh, V. Brovkin, P. Cadule, S. Doney, M. Eby, I. Fung, G. Bala, J. John, C. Jones, F. Joos, T. Kato, M. Kawamiya, W. Knorr, K. Lindsay, H. D. Matthews, T. Raddatz, P. Rayner, C. Reick, E. Roeckner, K.-G. Schnitzler, R. Schnur, K. Strassmann, A. J. Weaver, C. Yoshikawa, and N. Zeng, "Climate–carbon cycle

feedback analysis: Results from the c4mip model intercomparison," *Journal of Climate*, vol. 19, no. 14, pp. 3337 – 3353, 2006.

[12] P. Bousquet, P. Peylin, P. Ciais, C. Le Quéré, P. Friedlingstein, and P. P. Tans, "Regional changes in carbon dioxide fluxes of land and oceans since 1980," *Science*, vol. 290, no. 5495, pp. 1342–1346, 2000.

[13] C. D. Jones and P. M. Cox, "Modeling the volcanic signal in the atmospheric co2 record," *Global Biogeochemical Cycles*, vol. 15, no. 2, pp. 453–465, 2001.

[14] W. Lucht, I. C. Prentice, R. B. Myneni, S. Sitch, P. Friedlingstein, W. Cramer, P. Bousquet, W. Buermann, and B. Smith, "Climatic control of the high-latitude vegetation greening trend and pinatubo effect," *Science*, vol. 296, no. 5573, pp. 1687–1689, 2002.

[15] J. Hansen, A. Lacis, D. Rind, G. Russell, P. Stone, I. Fung, R. Ruedy, and J. Lerner, *Climate sensitivity: Analysis of feedback mechanisms*, ser. AGU Geophysical Monograph 29, Maurice Ewing Vol. 5. Washington, D.C.: American Geophysical Union, 1984, pp. 130–163.

[16] B. Marcolla, M. Migliavacca, C. Rödenbeck, and A. Cescatti, "Patterns and trends of the dominant environmental controls of net biome productivity," *Biogeosciences*, vol. 17, no. 8, pp. 2365–2379, 2020.

[17] G. Z. Xian, T. Loveland, S. M. Munson, J. E. Vogelmann, X. Zeng, and C. J. Homer, "Climate sensitivity to decadal land cover and land use change across the conterminous United States," *Global and Planetary Change*, vol. 192, p. 103262, Sep. 2020.

[18] D. Frank, M. Reichstein, M. Bahn, K. Thonicke, D. Frank, M. D. Mahecha, P. Smith, M. van der Velde, S. Vicca, F. Babst, C. Beer, N. Buchmann, J. G. Canadell, P. Ciais, W. Cramer, A. Ibrom, F. Miglietta, B. Poulter, A. Rammig, S. I. Seneviratne, A. Walz, M. Wattenbach, M. A. Zavala, and J. Zscheischler, "Effects of climate extremes on the terrestrial carbon cycle: concepts, processes and potential future impacts," *Global Change Biology*, vol. 21, no. 8, pp. 2861–2880, 2015.

[19] K. Ichii, H. Hashimoto, R. Nemani, and M. White, "Modeling the interannual variability and trends in gross and net primary productivity of tropical forests from 1982 to 1999," *Global and Planetary Change*, vol. 48, no. 4, pp. 274–286, 2005.

[20] S. Piao, X. Wang, K. Wang, X. Li, A. Bastos, J. G. Canadell, P. Ciais, P. Friedlingstein, and S. Sitch, “Interannual variation of terrestrial carbon cycle: Issues and perspectives,” *Global Change Biology*, vol. 26, no. 1, pp. 300–318, 2020.

[21] J. Zscheischler, M. Reichstein, J. von Buttlar, M. Mu, J. T. Randerson, and M. D. Mahecha, “Carbon cycle extremes during the 21st century in cmip5 models: Future evolution and attribution to climatic drivers,” *Geophysical Research Letters*, vol. 41, no. 24, pp. 8853–8861, 2014.

[22] Z. Zhu, S. Piao, R. Myneni, M. Huang, Z. Zeng, J. Canadell, P. Ciais, S. Sitch, P. Friedlingstein, A. Arneth, C. Cao, L. Cheng, E. Kato, C. Koven, Y. Li, X. Lian, Y. Liu, R. Liu, J. Mao, and N. Zeng, “Greening of the earth and its drivers,” *Nature Climate Change*, vol. 6, 04 2016.

[23] F. M. Hoffman, J. T. Randerson, V. K. Arora, Q. Bao, P. Cadule, D. Ji, C. D. Jones, M. Kawamiya, S. Khatiwala, K. Lindsay, A. Obata, E. Shevliakova, K. D. Six, J. F. Tjiputra, E. M. Volodin, and T. Wu, “Causes and implications of persistent atmospheric carbon dioxide biases in earth system models,” *Journal of Geophysical Research: Biogeosciences*, vol. 119, no. 2, pp. 141–162, 2014.

[24] J. K. Moore, W. Fu, F. Primeau, G. L. Britten, K. Lindsay, M. Long, S. C. Doney, N. Mahowald, F. Hoffman, and J. T. Randerson, “Sustained climate warming drives declining marine biological productivity,” *Science*, vol. 359, no. 6380, pp. 1139–1143, 2018.

[25] W. Hubau, S. L. Lewis, O. L. Phillips, K. Affum-Baffoe, H. Beeckman, A. Cuní-Sanchez, A. K. Daniels, C. E. Ewango, S. Fauset, J. M. Mukinzi *et al.*, “Asynchronous carbon sink saturation in African and Amazonian tropical forests,” *Nature*, vol. 579, no. 7797, pp. 80–87, 2020.

[26] A. J. Pitman, N. de Noblet-Ducoudré, F. B. Avila, L. V. Alexander, J.-P. Boisier, V. Brovkin, C. Delire, F. Cruz, M. G. Donat, V. Gayler, B. van den Hurk, C. Reick, and A. Voldoire, “Effects of land cover change on temperature and rainfall extremes in multi-model ensemble simulations,” *Earth System Dynamics*, vol. 3, no. 2, pp. 213–231, 2012.

[27] G. C. Hurtt, L. P. Chini, S. Frolking, R. A. Betts, J. Feddema, G. Fischer, J. P. Fisk, K. Hibbard, R. A. Houghton, A. Janetos, C. D. Jones, G. Kindermann, T. Kinoshita, K. Klein Goldewijk, K. Riahi, E. Shevliakova, S. Smith, E. Stehfest, A. Thomson, P. Thornton, D. P. van Vuuren, and Y. P. Wang, “Harmonization of land-use scenarios for the period 1500–2100: 600 years

of global gridded annual land-use transitions, wood harvest, and resulting secondary lands," *Climatic Change*, vol. 109, no. 1, p. 117, Aug 2011.

[28] K. W. Oleson, D. M. Lawrence, G. B. Bonan, M. G. Flanner, E. Kluzek, P. J. Lawrence, S. Levis, S. C. Swenson, P. E. Thornton, A. Dai, M. Decker, R. Dickinson, J. Feddema, C. Heald, F. Hoffman, J.-F. Lamarque, N. Mahowald, G.-Y. Niu, T. Qian, J. Randerson, S. Running, K. Sakaguchi, A. Slater, R. Stöckli, A. Wang, Z.-L. Yang, X. Zeng, and X. Zeng, "Technical description of version 4.0 of the Community Land Model (CLM)," National Center for Atmospheric Research, Boulder, Colorado, USA, Technical Note NCAR/TN-478+STR, Mar. 2010. [Online]. Available: http://www.cesm.ucar.edu/models/cesm1.0/clm/CLM4_Tech_Note.pdf

[29] G. B. Bonan, P. J. Lawrence, K. W. Oleson, S. Levis, M. Jung, M. Reichstein, D. M. Lawrence, and S. C. Swenson, "Improving canopy processes in the community land model version 4 (clm4) using global flux fields empirically inferred from fluxnet data," *Journal of Geophysical Research: Biogeosciences*, vol. 116, no. G2, 2011.

[30] C. D. Koven, W. J. Riley, Z. M. Subin, J. Y. Tang, M. S. Torn, W. D. Collins, G. B. Bonan, D. M. Lawrence, and S. C. Swenson, "The effect of vertically resolved soil biogeochemistry and alternate soil c and n models on c dynamics of clm4," *Biogeosciences*, vol. 10, no. 11, pp. 7109–7131, 2013.

[31] M. Flach, A. Brenning, F. Gans, M. Reichstein, S. Sippel, and M. D. Mahecha, "Vegetation modulates the impact of climate extremes on gross primary production," *Biogeosciences Discussions*, vol. 2020, pp. 1–20, 2020.

[32] K. Lindsay, G. B. Bonan, S. C. Doney, F. M. Hoffman, D. M. Lawrence, M. C. Long, N. M. Mahowald, J. Keith Moore, J. T. Randerson, and P. E. Thornton, "Preindustrial-control and twentieth-century carbon cycle experiments with the earth system model cesm1(bgc)," *Journal of Climate*, vol. 27, no. 24, pp. 8981–9005, 2014.

[33] P. J. Lawrence, J. J. Feddema, G. B. Bonan, G. A. Meehl, B. C. O'Neill, K. W. Oleson, S. Levis, D. M. Lawrence, E. Kluzek, K. Lindsay, and P. E. Thornton, "Simulating the biogeochemical and biogeophysical impacts of transient land cover change and wood harvest in the community climate system model (ccsm4) from 1850 to 2100," *Journal of Climate*, vol. 25, no. 9, pp. 3071–3095, 2012.

[34] N. Collier, F. M. Hoffman, D. M. Lawrence, G. Keppel-Aleks, C. D. Koven, W. J. Riley, M. Mu, and J. T. Randerson, "The international land model benchmarking (ilamb) system: Design, theory, and implementation," *Journal of Advances in Modeling Earth Systems*, vol. 10, no. 11, pp. 2731–2754, 2018.

[35] N. M. Mahowald, J. T. Randerson, K. Lindsay, E. Munoz, S. C. Doney, P. Lawrence, S. Schlunegger, D. S. Ward, D. Lawrence, and F. M. Hoffman, "Interactions between land use change and carbon cycle feedbacks," *Global Biogeochemical Cycles*, vol. 31, no. 1, pp. 96–113, 2017.

[36] J.-F. Lamarque, T. C. Bond, V. Eyring, C. Granier, A. Heil, Z. Klimont, D. Lee, C. Liousse, A. Mieville, B. Owen, M. G. Schultz, D. Shindell, S. J. Smith, E. Stehfest, J. Van Aardenne, O. R. Cooper, M. Kainuma, N. Mahowald, J. R. McConnell, V. Naik, K. Riahi, and D. P. van Vuuren, "Historical (1850–2000) gridded anthropogenic and biomass burning emissions of reactive gases and aerosols: methodology and application," *Atmospheric Chemistry and Physics*, vol. 10, no. 15, pp. 7017–7039, 2010.

[37] S. I. Seneviratne and M. Hauser, "Regional climate sensitivity of climate extremes in cmip6 vs cmip5 multi-model ensembles," *Earth's Future*, p. e2019EF001474, 2020.

[38] N. Ban, J. Schmidli, and C. Schär, "Heavy precipitation in a changing climate: Does short-term summer precipitation increase faster?" *Geophysical Research Letters*, vol. 42, no. 4, pp. 1165–1172, 2015.

[39] M. Xu, S. Mahajan, F. M. Hoffman, and X. Shi, "Evaluating carbon extremes in a coupled climate-carbon cycle simulation," in *Proceedings of the 2019 IEEE International Conference on Data Mining Workshops (ICDMW 2019)*, Institute of Electrical and Electronics Engineers (IEEE). Conference Publishing Services (CPS), Nov. 2019, pp. 303–310.

[40] S. I. Seneviratne, N. Nicholls, D. Easterling, C. M. Goodess, S. Kanae, J. Kossin, Y. Luo, J. Marengo, K. McInnes, M. Rahimi, M. Reichstein, A. Sorteberg, C. Vera, and X. Zhang, *Changes in Climate Extremes and their Impacts on the Natural Physical Environment*. Cambridge Univ. Press, Cambridge, U.K., and New York, 2012, pp. 109–230, [Field, C.B., V. Barros, T.F. Stocker, D. Qin, D.J. Dokken, K.L. Ebi, M.D. Mastrandrea, K.J. Mach, G.-K. Plattner, S.K. Allen, M. Tignor, and P.M. Midgley (eds.)]. A Special Report of Working Groups I and II of the Intergovernmental Panel on Climate Change (IPCC).

[41] J. W. Baldwin, J. B. Dessy, G. A. Vecchi, and M. Oppenheimer, “Temporally compound heat wave events and global warming: An emerging hazard,” *Earth’s Future*, vol. 7, no. 4, pp. 411–427, 2019.

[42] N. Golyandina, V. Nekrutkin, and A. A. Zhigljavsky, *Analysis of Time Series Structure: SSA and Related Techniques*, 1st ed. Chapman and Hall/CRC, Jan. 2001.

[43] P. Chylek, P. Tans, J. Christy, and M. K. Dubey, “The carbon cycle response to two el nino types: an observational study,” *Environmental Research Letters*, vol. 13, no. 2, p. 024001, Jan 2018.

[44] G. Poveda, A. Jaramillo, M. M. Gil, N. Quiceno, and R. I. Mantilla, “Seasonally in enso-related precipitation, river discharges, soil moisture, and vegetation index in colombia,” *Water Resources Research*, vol. 37, no. 8, pp. 2169–2178, 2001.

[45] Z. Wu, E. K. Schneider, B. Kirtman, E. Sarachik, N. Huang, and C. J. Tucker, “The modulated annual cycle: An alternative reference frame for climate anomalies,” *Climate Dynamics*, vol. 31, pp. 823–841, 12 2008.

[46] T. Zhang, M. Xu, Y. Xi, J. Zhu, L. Tian, X. Zhang, Y. Wang, Y. Li, P. Shi, G. Yu, X. Sun, and Y. Zhang, “Lagged climatic effects on carbon fluxes over three grassland ecosystems in China,” *Journal of Plant Ecology*, vol. 8, no. 3, pp. 291–302, 12 2014.

[47] J. Zscheischler, S. Westra, B. J. Van Den Hurk, S. I. Seneviratne, P. J. Ward, A. Pitman, A. Aghakouchak, D. N. Bresch, M. Leonard, T. Wahl, and X. Zhang, “Future climate risk from compound events,” *Nature Climate Change*, vol. 8, no. 6, pp. 469–477, 2018.

[48] S. Pan, J. Yang, H. Tian, H. Shi, J. Chang, P. Ciais, L. Francois, K. Frieler, B. Fu, T. Hickler, A. Ito, K. Nishina, S. Ostberg, C. P. Reyer, S. Schaphoff, J. Steinkamp, and F. Zhao, “Climate extreme versus carbon extreme: Responses of terrestrial carbon fluxes to temperature and precipitation,” *Journal of Geophysical Research: Biogeosciences*, vol. 125, no. 4, p. e2019JG005252, 2019.

[49] P. A. O’Gorman, “Precipitation extremes under climate change,” *Current Climate Change Reports*, vol. 1, no. 2, pp. 49–59, Jun 2015.

[50] D. M. Lawrence, G. C. Hurtt, A. Arneth, V. Brovkin, K. V. Calvin, A. D. Jones, C. D. Jones, P. J. Lawrence, N. de Noblet-Ducoudré, J. Pongratz, S. I. Seneviratne, and E. Shevliakova,

"The Land Use Model Intercomparison Project (LUMIP) contribution to CMIP6: Rationale and experimental design," *Geoscientific Model Development*, vol. 9, no. 9, pp. 2973–2998, 2016.

[51] I. N. Williams, M. S. Torn, W. J. Riley, and M. F. Wehner, "Impacts of climate extremes on gross primary production under global warming," *Environmental Research Letters*, vol. 9, no. 9, p. 094011, Sep 2014.

[52] T. Keenan, I. Baker, A. Barr, P. Ciais, K. Davis, M. Dietze, D. Dragoni, C. M. Gough, R. Grant, D. Hollinger, K. Hufkens, B. Poulter, H. McCaughey, B. Raczka, Y. Ryu, K. Schaefer, H. Tian, H. Verbeeck, M. Zhao, and A. D. Richardson, "Terrestrial biosphere model performance for inter-annual variability of land-atmosphere $CO_2$ exchange," *Global Change Biology*, vol. 18, no. 6, pp. 1971–1987, 2012.

[53] L. Cao, G. Bala, K. Caldeira, R. Nemani, and G. Ban-Weiss, "Importance of carbon dioxide physiological forcing to future climate change," *Proceedings of the National Academy of Sciences*, vol. 107, no. 21, pp. 9513–9518, 2010.

[54] A. L. S. Swann, F. M. Hoffman, C. D. Koven, and J. T. Randerson, "Plant responses to increasing $co_2$ reduce estimates of climate impacts on drought severity," *Proceedings of the National Academy of Sciences*, vol. 113, no. 36, pp. 10 019–10 024, 2016. [Online]. Available: https://www.pnas.org/doi/abs/10.1073/pnas.1604581113

[55] B. Langenbrunner, M. S. Pritchard, G. J. Kooperman, and J. T. Randerson, "Why does Amazon precipitation decrease when tropical forests respond to increasing $CO_2$?" *Earth's Future*, vol. 7, no. 4, pp. 450–468, 2019.

[56] G. B. Bonan, K. W. Oleson, R. A. Fisher, G. Lasslop, and M. Reichstein, "Reconciling leaf physiological traits and canopy flux data: Use of the try and fluxnet databases in the community land model version 4," *Journal of Geophysical Research: Biogeosciences*, vol. 117, no. G2, 2012.

[57] D. L. Lombardozzi, Y. Lu, P. J. Lawrence, D. M. Lawrence, S. Swenson, K. W. Oleson, W. R. Wieder, and E. A. Ainsworth, "Simulating agriculture in the community land model version 5," *Journal of Geophysical Research: Biogeosciences*, vol. 125, no. 8, p. e2019JG005529, 2020.

[58] D. L. Lombardozzi, G. B. Bonan, N. G. Smith, J. S. Dukes, and R. A. Fisher, "Temperature acclimation of photosynthesis and respiration: A key uncertainty in the carbon cycle-climate feedback," *Geophysical Research Letters*, vol. 42, no. 20, pp. 8624–8631, 2015.

[59] B. Sharma, J. Kumar, N. Collier, A. R. Ganguly, and F. M. Hoffman, "Quantifying carbon cycle extremes and attributing their causes under climate and land use and land cover change from 1850 to 2300," *Journal of Geophysical Research: Biogeosciences*, vol. 127, no. 6, p. e2021JG006738, 2022, e2021JG006738 2021JG006738.

[60] S. Piao, X. Zhang, A. Chen, Q. Liu, X. Lian, X. Wang, S. Peng, and X. Wu, "The impacts of climate extremes on the terrestrial carbon cycle: A review," *Science China Earth Sciences*, vol. 62, no. 10, pp. 1551–1563, 2019.

[61] J. von Buttlar, J. Zscheischler, A. Rammig, S. Sippel, M. Reichstein, A. Knohl, M. Jung, O. Menzer, M. A. Arain, N. Buchmann, A. Cescatti, D. Gianelle, G. Kiely, B. E. Law, V. Magliulo, H. Margolis, H. McCaughey, L. Merbold, M. Migliavacca, L. Montagnani, W. Oechel, M. Pavelka, M. Peichl, S. Rambal, A. Raschi, R. L. Scott, F. P. Vaccari, E. van Gorsel, A. Varlagin, G. Wohlfahrt, and M. D. Mahecha, "Impacts of droughts and extreme-temperature events on gross primary production and ecosystem respiration: a systematic assessment across ecosystems and climate zones," *Biogeosciences*, vol. 15, no. 5, pp. 1293–1318, 2018. [Online]. Available: https://bg.copernicus.org/articles/15/1293/2018/

[62] N. S. Diffenbaugh, D. Singh, J. S. Mankin, D. E. Horton, D. L. Swain, D. Touma, A. Charland, Y. Liu, M. Haugen, M. Tsiang, and B. Rajaratnam, "Quantifying the influence of global warming on unprecedented extreme climate events," *Proceedings of the National Academy of Sciences*, vol. 114, no. 19, pp. 4881–4886, 2017.

[63] M. R. Grose, S. Narsey, F. P. Delage, A. J. Dowdy, M. Bador, G. Boschat, C. Chung, J. B. Kajtar, S. Rauniyar, M. B. Freund, K. Lyu, H. Rashid, X. Zhang, S. Wales, C. Trenham, N. J. Holbrook, T. Cowan, L. Alexander, J. M. Arblaster, and S. Power, "Insights From CMIP6 for Australia's Future Climate," *Earth's Future*, vol. 8, no. 5, p. e2019EF001469, 2020, e2019EF001469 2019EF001469.

[64] T. R. Ault, "On the essentials of drought in a changing climate," *Science*, vol. 368, no. 6488, pp. 256–260, 2020.

[65] A. F. S. Ribeiro, A. Russo, C. M. Gouveia, P. Páscoa, and J. Zscheischler, “Risk of crop failure due to compound dry and hot extremes estimated with nested copulas,” *Biogeosciences*, vol. 17, no. 19, pp. 4815–4830, 2020.

[66] G. Danabasoglu, J.-F. Lamarque, J. Bacmeister, D. A. Bailey, A. K. DuVivier, J. Edwards, L. K. Emmons, J. Fasullo, R. Garcia, A. Gettelman, C. Hannay, M. M. Holland, W. G. Large, P. H. Lauritzen, D. M. Lawrence, J. T. M. Lenaerts, K. Lindsay, W. H. Lipscomb, M. J. Mills, R. Neale, K. W. Oleson, B. Otto-Bliesner, A. S. Phillips, W. Sacks, S. Tilmes, L. van Kampenhout, M. Vertenstein, A. Bertini, J. Dennis, C. Deser, C. Fischer, B. Fox-Kemper, J. E. Kay, D. Kinnison, P. J. Kushner, V. E. Larson, M. C. Long, S. Mickelson, J. K. Moore, E. Nienhouse, L. Polvani, P. J. Rasch, and W. G. Strand, “The Community Earth System Model Version 2 (CESM2),” *Journal of Advances in Modeling Earth Systems*, vol. 12, no. 2, p. e2019MS001916, 2020, e2019MS001916 2019MS001916. [Online]. Available: https://agupubs.onlinelibrary.wiley.com/doi/abs/10.1029/2019MS001916

[67] D. M. Lawrence, R. A. Fisher, C. D. Koven, K. W. Oleson, S. C. Swenson, G. Bonan, N. Collier, B. Ghimire, L. van Kampenhout, D. Kennedy *et al.*, “The Community Land Model version 5: Description of new features, benchmarking, and impact of forcing uncertainty,” *Journal of Advances in Modeling Earth Systems*, vol. 11, no. 12, pp. 4245–4287, 2019.

[68] J. Zscheischler, M. D. Mahecha, J. von Buttlar, S. Harmeling, M. Jung, A. Rammig, J. T. Randerson, B. Schölkopf, S. I. Seneviratne, E. Tomelleri, S. Zaehle, and M. Reichstein, “A few extreme events dominate global interannual variability in gross primary production,” *Environmental Research Letters*, vol. 9, no. 3, p. 035001, mar 2014.

[69] C. F. Dormann, J. Elith, S. Bacher, C. Buchmann, G. Carl, G. Carré, J. R. G. Marquéz, B. Gruber, B. Lafourcade, P. J. Leitão, T. Münkemüller, C. McClean, P. E. Osborne, B. Reineking, B. Schröder, A. K. Skidmore, D. Zurell, and S. Lautenbach, “Collinearity: a review of methods to deal with it and a simulation study evaluating their performance,” *Ecography*, vol. 36, no. 1, pp. 27–46, 2013.

[70] L. Liu, L. Gudmundsson, M. Hauser, D. Qin, S. Li, and S. I. Seneviratne, “Soil moisture dominates dryness stress on ecosystem production globally,” *Nature Communications*, vol. 11, no. 1, pp. 1–9, 2020.

[71] F. Li, S. Levis, and D. S. Ward, "Quantifying the role of fire in the Earth system; Part 1: Improved global fire modeling in the Community Earth System Model (CESM1)," *Biogeosciences*, vol. 10, no. 4, pp. 2293–2314, 2013.

[72] A. P. Walker, M. G. De Kauwe, B. E. Medlyn, S. Zaehle, C. M. Iversen, S. Asao, B. Guenet, A. Harper, T. Hickler, B. A. Hungate *et al.*, "Decadal biomass increment in early secondary succession woody ecosystems is increased by co2 enrichment," *Nature Communications*, vol. 10, no. 1, pp. 1–13, 2019.

[73] S. M. Natali, J. D. Watts, B. M. Rogers, S. Potter, S. M. Ludwig, A.-K. Selbmann, P. F. Sullivan, B. W. Abbott, K. A. Arndt, L. Birch *et al.*, "Large loss of co2 in winter observed across the northern permafrost region," *Nature Climate Change*, vol. 9, no. 11, pp. 852–857, 2019.

[74] M. H. Jones, J. T. Fahnestock, D. A. Walker, M. D. Walker, and J. M. Welker, "Carbon dioxide fluxes in moist and dry arctic tundra during the snow-free season: Responses to increases in summer temperature and winter snow accumulation," *Arctic and Alpine Research*, vol. 30, no. 4, pp. 373–380, 1998.

[75] R. Commane, J. Lindaas, J. Benmergui, K. A. Luus, R. Y.-W. Chang, B. C. Daube, E. S. Euskirchen, J. M. Henderson, A. Karion, J. B. Miller, S. M. Miller, N. C. Parazoo, J. T. Randerson, C. Sweeney, P. Tans, K. Thoning, S. Veraverbeke, C. E. Miller, and S. C. Wofsy, "Carbon dioxide sources from alaska driven by increasing early winter respiration from arctic tundra," *Proceedings of the National Academy of Sciences*, vol. 114, no. 21, pp. 5361–5366, 2017.

[76] M. R. Turetsky, B. W. Abbott, M. C. Jones, K. W. Anthony, D. Olefeldt, E. A. Schuur, G. Grosse, P. Kuhry, G. Hugelius, C. Koven *et al.*, "Carbon release through abrupt permafrost thaw," *Nature Geoscience*, vol. 13, no. 2, pp. 138–143, 2020.

[77] A. Ahlström, J. Xia, A. Arneth, Y. Luo, and B. Smith, "Importance of vegetation dynamics for future terrestrial carbon cycling," *Environmental Research Letters*, vol. 10, no. 5, p. 054019, may 2015.

[78] C. Chen, B. He, W. Yuan, L. Guo, and Y. Zhang, "Increasing interannual variability of global vegetation greenness," *Environmental Research Letters*, vol. 14, no. 12, p. 124005, nov 2019. [Online]. Available: https://doi.org/10.1088/1748-9326/ab4ffc

[79] M. Reichstein, M. Bahn, M. D. Mahecha, J. Kattge, and D. D. Baldocchi, “Linking plant and ecosystem functional biogeography,” *Proceedings of the National Academy of Sciences*, vol. 111, no. 38, pp. 13 697–13 702, 2014.

[80] F. M. Hoffman, C. D. Koven, G. Keppel-Aleks, D. M. Lawrence, W. J. Riley, J. T. Randerson, A. Ahlström, G. Abramowitz, D. D. Baldocchi, M. J. Best, B. Bond-Lamberty, M. G. De Kauwe, A. S. Denning, A. R. Desai, V. Eyring, J. B. Fisher, R. A. Fisher, P. J. Gleckler, M. Huang, G. Hugelius, A. K. Jain, N. Y. Kiang, H. Kim, R. D. Koster, S. V. Kumar, H. Li, Y. Luo, J. Mao, N. G. McDowell, U. Mishra, P. R. Moorcroft, G. S. Pau, D. M. Ricciuto, K. Schaefer, C. R. Schwalm, S. P. Serbin, E. Shevliakova, A. G. Slater, J. Tang, M. Williams, J. Xia, C. Xu, R. Joseph, and D. Koch, “2016 international land model benchmarking (ilamb) workshop report,” USDOE Office of Science, Washington, DC (United States), Tech. Rep., 4 2017.

[81] M. Jung, C. Schwalm, M. Migliavacca, S. Walther, G. Camps-Valls, S. Koirala, P. Anthoni, S. Besnard, P. Bodesheim, N. Carvalhais, F. Chevallier, F. Gans, D. S. Goll, V. Haverd, P. Köhler, K. Ichii, A. K. Jain, J. Liu, D. Lombardozzi, J. E. M. S. Nabel, J. A. Nelson, M. O’Sullivan, M. Pallandt, D. Papale, W. Peters, J. Pongratz, C. Rödenbeck, S. Sitch, G. Tramontana, A. Walker, U. Weber, and M. Reichstein, “Scaling carbon fluxes from eddy covariance sites to globe: synthesis and evaluation of the fluxcom approach,” *Biogeosciences*, vol. 17, no. 5, pp. 1343–1365, 2020.

[82] M. Jung and F. team FLUXCOM, “global land carbon fluxes using cruncep climate data,” *FLUXCOM Data Portal*, 2016.

[83] X. Li and J. Xiao, “A global, 0.05-degree product of solar-induced chlorophyll fluorescence derived from oco-2, modis, and reanalysis data,” *Remote Sensing*, vol. 11, no. 5, 2019.

[84] S. H. Alemohammad, B. Fang, A. G. Konings, F. Aires, J. K. Green, J. Kolassa, D. Miralles, C. Prigent, and P. Gentine, “Water, energy, and carbon with artificial neural networks (wecann): a statistically based estimate of global surface turbulent fluxes and gross primary productivity using solar induced fluorescence,” *Biogeosciences*, vol. 14, no. 18, pp. 4101–4124, 2017.

[85] P. A. Dirmeyer, X. Gao, M. Zhao, Z. Guo, T. Oki, and N. Hanasaki, “Gswp-2: Multimodel analysis and implications for our perception of the land surface,” *Bulletin of the American Meteorological Society*, vol. 87, no. 10, pp. 1381–1398, 2006.

[86] C. C. C. S. (C3S), “Era5: Fifth generation of ecmwf atmospheric reanalyses of the global climate,” *Copernicus Climate Change Service Climate Data Store (CDS)*, vol. 15, no. 2, p. 2020, 2017.

[87] B. Sharma, J. Kumar, A. R. Ganguly, and F. M. Hoffman, “Carbon cycle extremes accelerate weakening of the land carbon sink in the late 21st century,” *Biogeosciences Discussions*, vol. 2022, pp. 1–21, 2022.

[88] S. Fatichi, V. Y. Ivanov, and E. Caporali, “Investigating interannual variability of precipitation at the global scale: Is there a connection with seasonality?” *Journal of Climate*, vol. 25, no. 16, pp. 5512 – 5523, 2012.

[89] G. Kraemer, G. Camps-Valls, M. Reichstein, and M. D. Mahecha, “Summarizing the state of the terrestrial biosphere in few dimensions,” *Biogeosciences*, vol. 17, no. 9, pp. 2397–2424, 2020. [Online]. Available: https://bg.copernicus.org/articles/17/2397/2020/

[90] J. K. Green, S. I. Seneviratne, A. M. Berg, K. L. Findell, S. Hagemann, D. M. Lawrence, and P. Gentine, “Large influence of soil moisture on long-term terrestrial carbon uptake,” *Nature*, vol. 565, no. 7740, pp. 476–479, 2019.

[91] D. Schimel, B. B. Stephens, and J. B. Fisher, “Effect of increasing $co_2$ on the terrestrial carbon cycle,” *Proceedings of the National Academy of Sciences*, vol. 112, no. 2, pp. 436–441, 2015.

[92] J. Zscheischler, M. D. Mahecha, J. von Buttlar, S. Harmeling, M. Jung, A. Rammig, J. T. Randerson, B. Schölkopf, S. I. Seneviratne, E. Tomelleri, S. Zaehle, and M. Reichstein, “A few extreme events dominate global interannual variability in gross primary production,” *Environmental Research Letters*, vol. 9, no. 3, p. 035001, mar 2014.

[93] A. Seth, “Granger causality,” *Scholarpedia*, vol. 2, no. 7, p. 1667, 2007, revision #127333.

[94] S. Piao, S. Sitch, P. Ciais, P. Friedlingstein, P. Peylin, X. Wang, A. Ahlström, A. Anav, J. G. Canadell, N. Cong, C. Huntingford, M. Jung, S. Levis, P. E. Levy, J. Li, X. Lin, M. R. Lomas, M. Lu, Y. Luo, Y. Ma, R. B. Myneni, B. Poulter, Z. Sun, T. Wang, N. Viovy, S. Zaehle, and N. Zeng, “Evaluation of terrestrial carbon cycle models for their response to climate variability and to co2 trends,” *Global Change Biology*, vol. 19, no. 7, pp. 2117–2132, 2013.

# Appendix A

# Supplemantary Information Chapter 2

**Contents:**

1. Figures A1 to A11
2. Tables A1 to A5

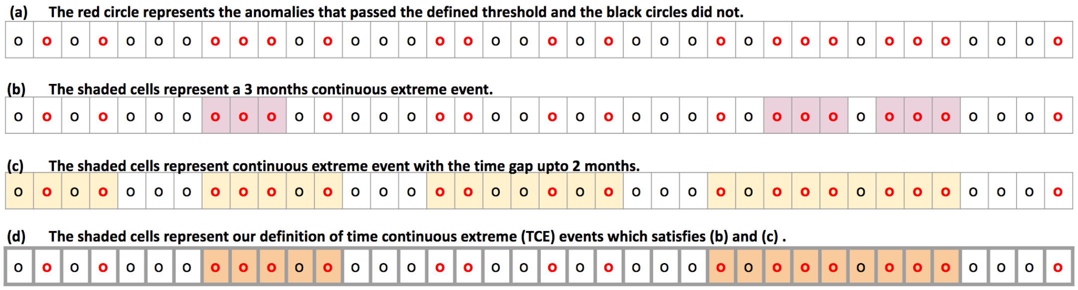

**(a)** **The red circle represents the anomalies that passed the defined threshold and the black circles did not.**

**(b)** **The shaded cells represent a 3 months continuous extreme event.**

**(c)** **The shaded cells represent continuous extreme event with the time gap upto 2 months.**

**(d)** **The shaded cells represent our definition of time continuous extreme (TCE) events which satisfies (b) and (c) .**

Figure A1: The schematic flow-diagram for finding a temporally contiguous extreme (TCE) event from a time series of variable anomalies at any grid cell. The black and red colored circles represent the anomalies that have not passed and passed the thresholds, respectively. Hence, red circles are individual extreme months in a time series of a variable anomalies (a). We then look for 3 month continuous extremes (b) which is the first condition to qualify as a TCE event. We also look for the individual or temporally continuous extremes that are located in vicinity of each other up to 2 months (c). The temporally contiguous extreme events that fulfil both conditions (shown in (b) and (c)) are referred to as TCE events.

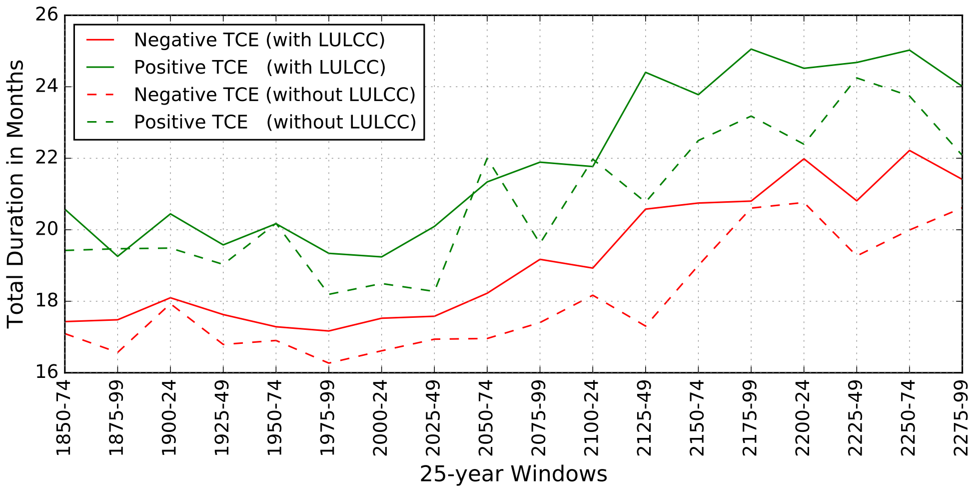

Figure A2: The standard deviation duration of temporally continuous extreme (TCE) events for every time window from 1850–2299. The figure shows the development of standard deviation duration of positive (shown in green) and negative (shown in red) TCEs for both the simulations, *with* (solid lines) and *without LULCC* (dashed lines).

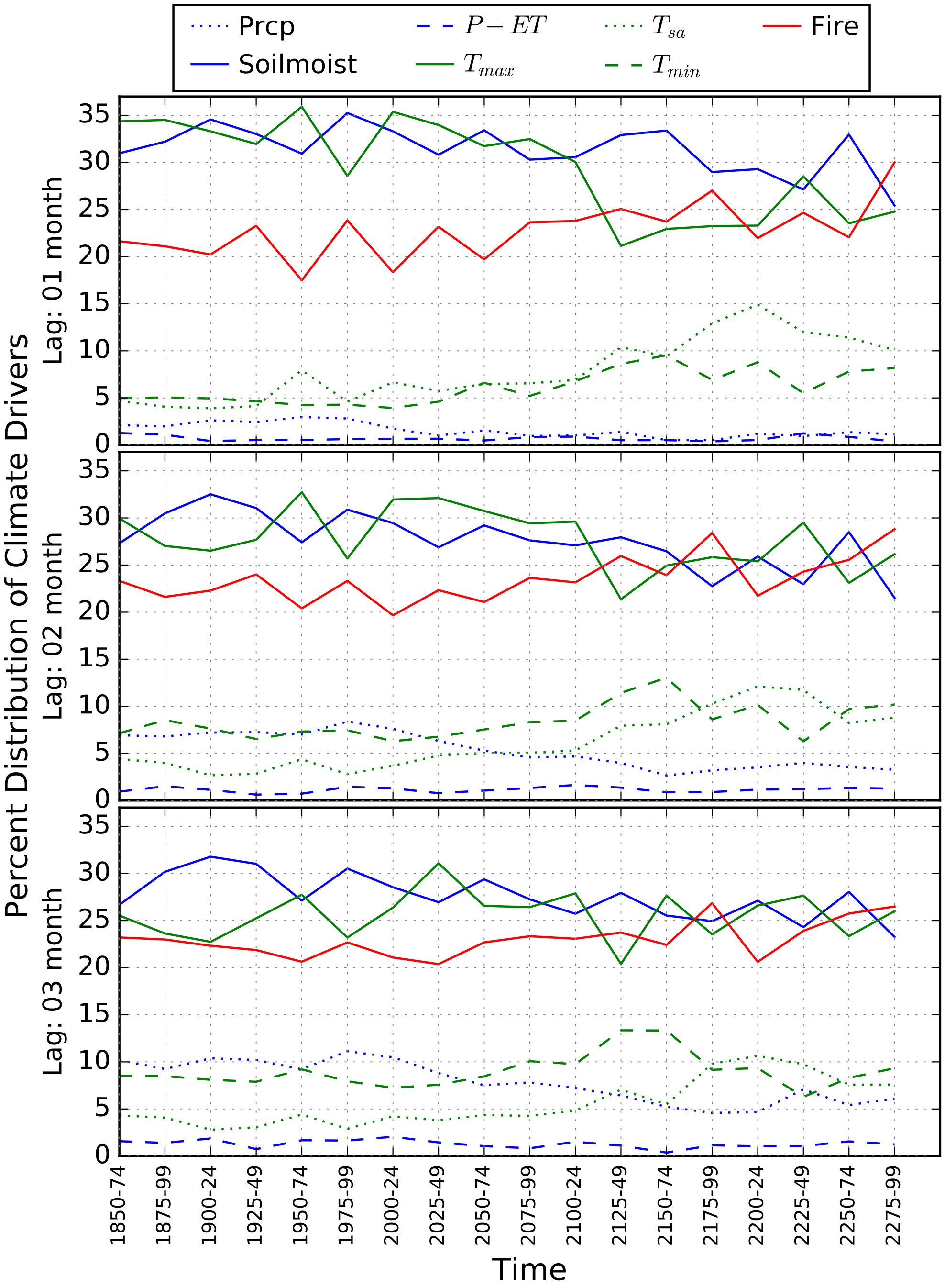

Figure A3: Percent distribution of global dominant climate drivers *without LULCC* for every time window from 1850–2299. For a particular lag month (1, 2, 3, etc.), a climate driver with highest correlation coefficient ($p < 0.05$) with carbon cycle TCEs at any grid cell is called a dominant climate driver.

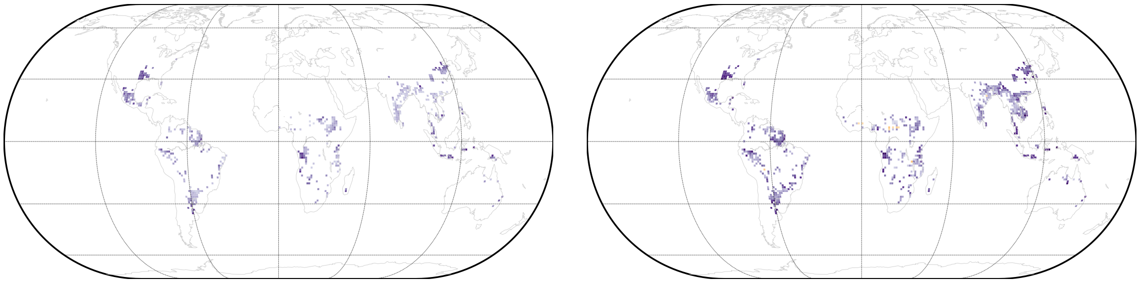

(a) Precipitation

(b) Soil Moisture

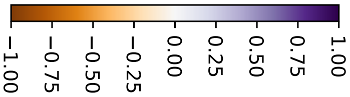

(c) Correlation Coefficient

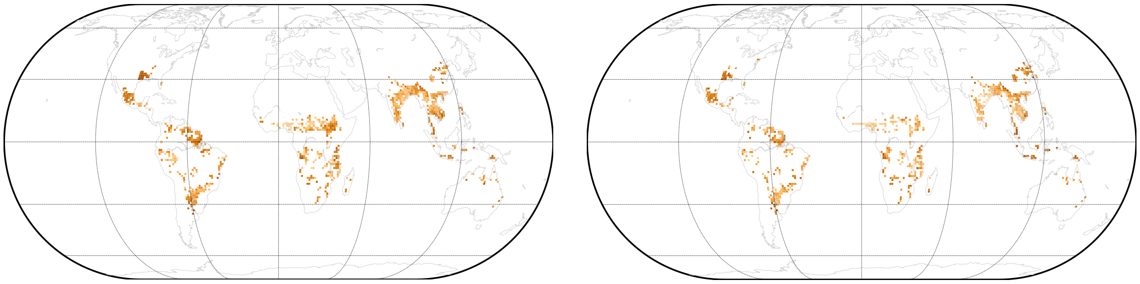

(d) Monthly Max Temperature

(e) Fire

Figure A4: Spatial distribution of climate drivers driving temporally continuous extremes in GPP at a lag of 1 month for the time window 2000–24 for *with LULCC*. Large losses in carbon uptake or increase in negative extremes, and reduction of precipitation and soil moisture are positively correlated. And, increase in temperatures and fire are negatively correlated with negative extremes in GPP. The compound effect of these climate drivers are shown in RGB maps (Figure 7).

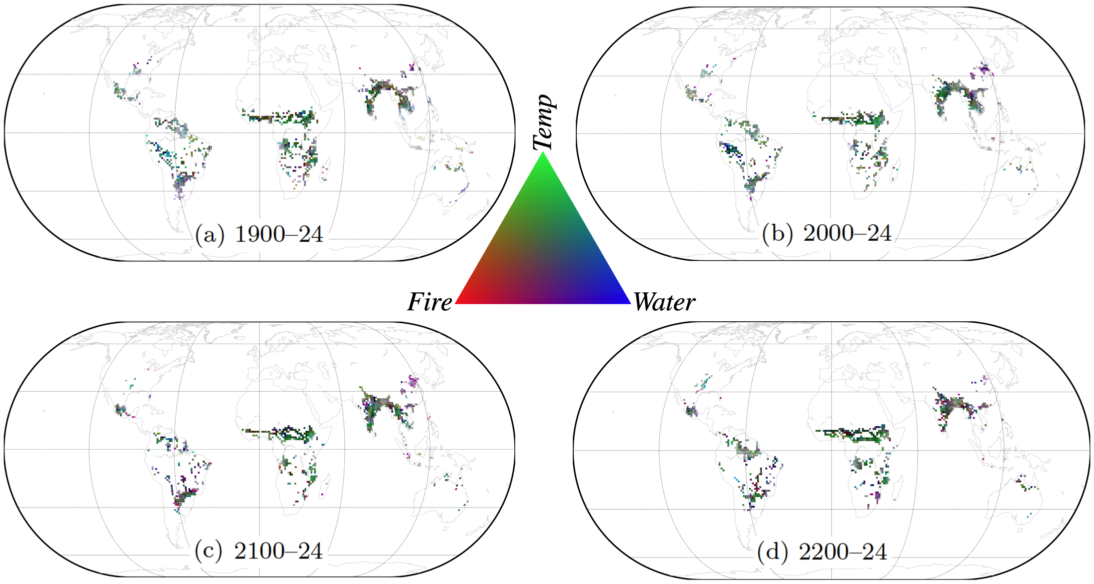

Figure A5: Spatial distribution of climate drivers attributing to negative TCEs for *without LULCC* for four 25-year time windows, (a) 1900–24, (b) 2000–24, (c) 2100–24, and (d) 2200–24. The climate drivers are pooled in three colors, red, green, and blue. Red ($Fire$) is for loss of carbon due to fire, green ($Temp$) represents monthly maximum, mean, and minimum daily temperatures ($T_{\mathrm{max}}$, $T_{\mathrm{sa}}$, $T_{\mathrm{min}}$ respectively), Blue ($Water$) includes monthly means of soil moisture, precipitation and $P{-}E$ (precipitation minus evapotranspiration). The results shown here are at 1 month lag.

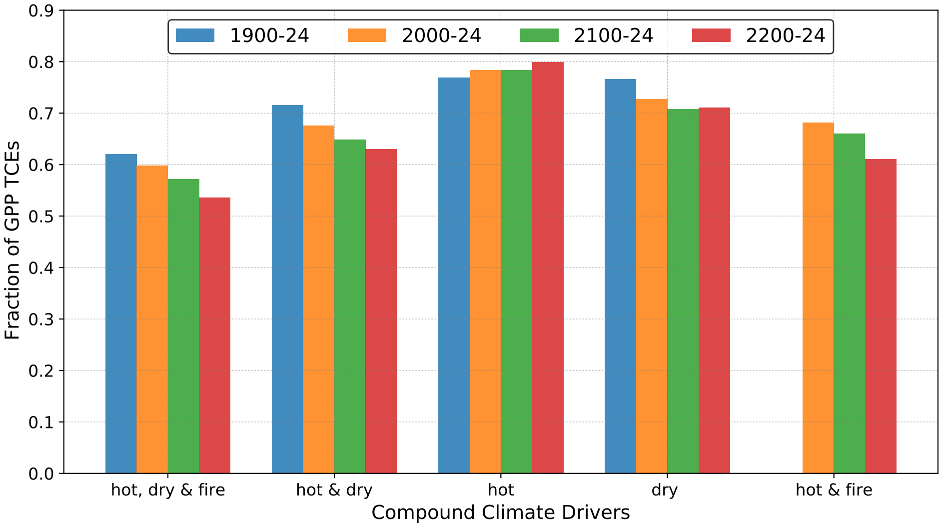

Figure A6: Attribution of temporally continuous extreme events in GPP to compound effect of climate drivers for *with LULCC* at lag of 1 month for 25-year time windows, (a) 1900–24, (b) 2000–24, (c) 2100–24, and (d) 2200–24. The fractions are mutually inclusive, i.e., events driven by *hot and dry* climate is also counted in either *hot* or *dry* climate driven events. Any location could be affected by one or compound climatic conditions. The chart here only represents the inclusiveness of the climatic conditions represented in Figure 8. The combined effect of hot and dry climate accompanied by fire leads to most negative TCE events in GPP.

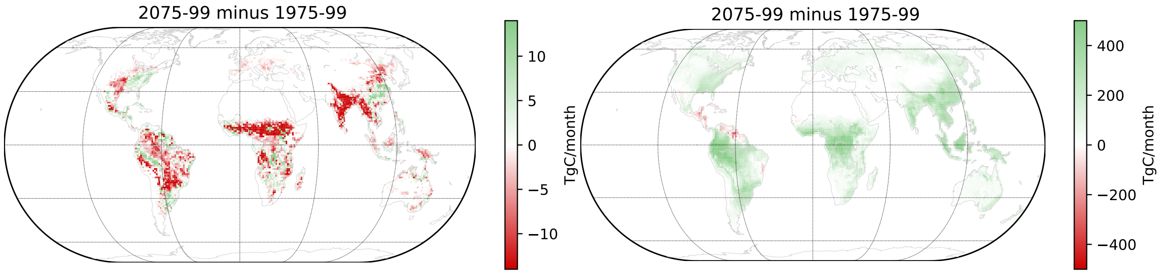

(a) Change of Negative GPP Extremes (21st century)

(b) Change of total GPP (21st century)

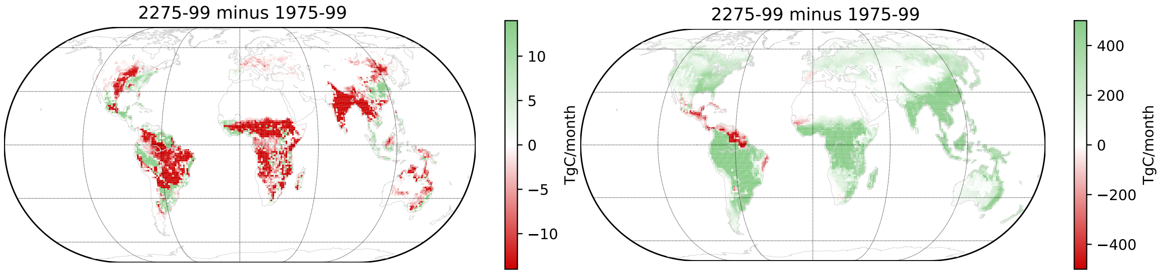

(c) Change of Negative GPP Extremes (23rd century)

(d) Change of total GPP (23rd century)

Figure A7: The GPP negative extremes in *without LULCC* (a)&(c) and GPP (b)&(d) are integrated over the whole globe and 25-year time periods. Red and green color in (a)&(c) indicates the increasing and weakening intensity of negative extremes respectively. Red and green color in (b)&(d) indicates the loss and increase of vegetation respectively.

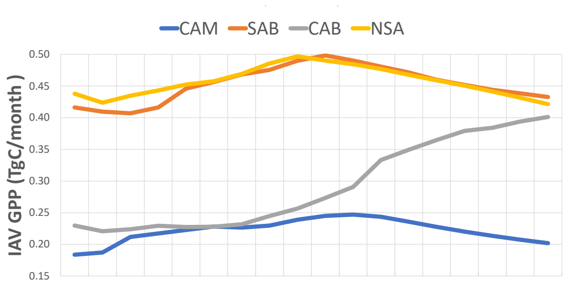

(a) The IAV of GPP.

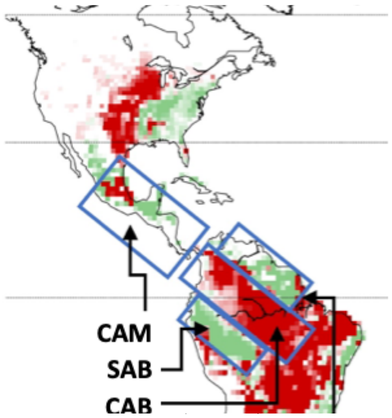

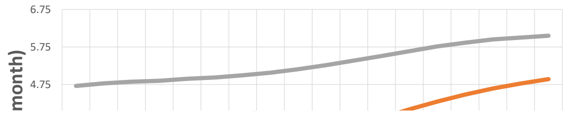

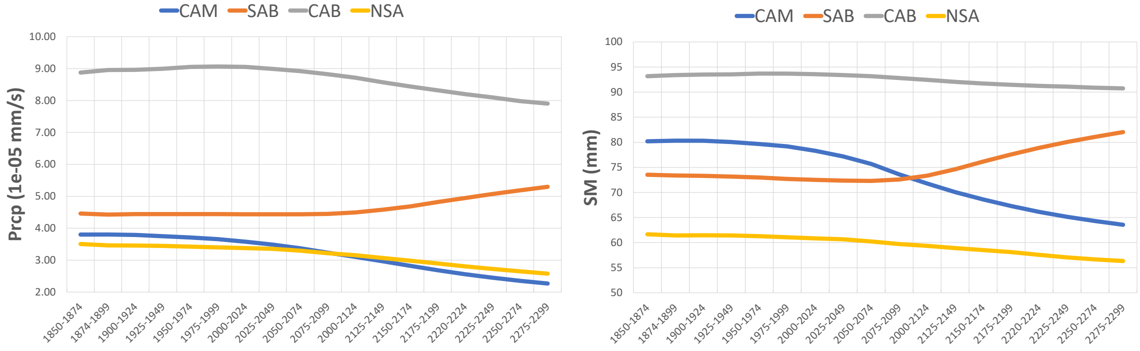

(d) Changes in precipitation.

(e) Changes in soil moisture.

Figure A8: The IAV of GPP and changes in GPP and climate drivers are shown for *without LULCC*. The IAV and changes are calculated from 1850 as the base year to 25 year increments, as shown in $x$-axis.

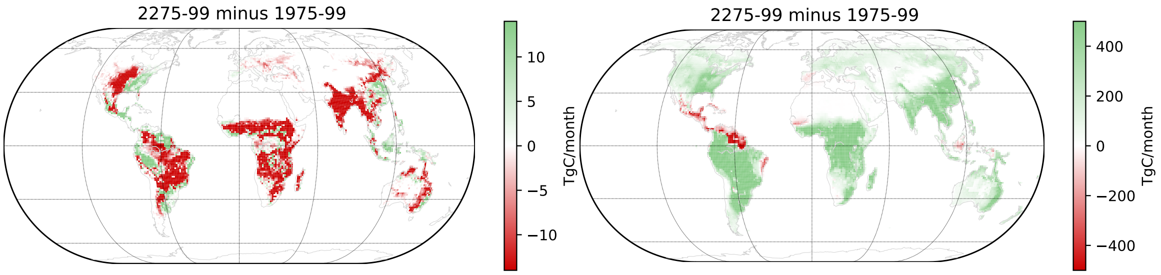

(a) Change of Negative GPP Extremes (23rd century)

(b) Change of total GPP (23rd century)

Figure A9: The GPP negative extremes in *with LULCC* (a) and GPP (b) are integrated over the whole globe and 25-year time period. Red and green color in (a) indicates the increasing and weakening intensity of negative extremes respectively. Red and green color in (b) indicates the loss and increase of vegetation respectively. The patterns are similar to the *without LULCC* except for Indonesia which shows the decline of productivity and weakening of negative extreme events.

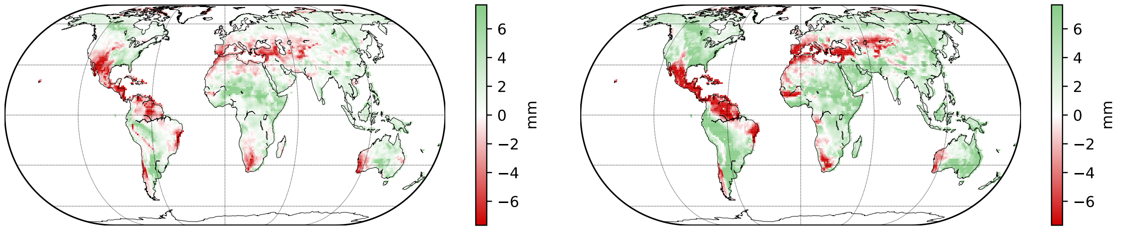

(a) Changes in Soil Moisture (21st century)

(b) Changes in Soil Moisture (23rd century)

Figure A10: The area weighted average of Soil Moisture for *without LULCC*. (a) Changes in soil moisture for years 2075–2099 minus 1975–1999 and (b) changes in soil moisture for years 2275–2099 minus 1975–1999. Red and green color in indicates the reduction and increase of soil moisture respectively.

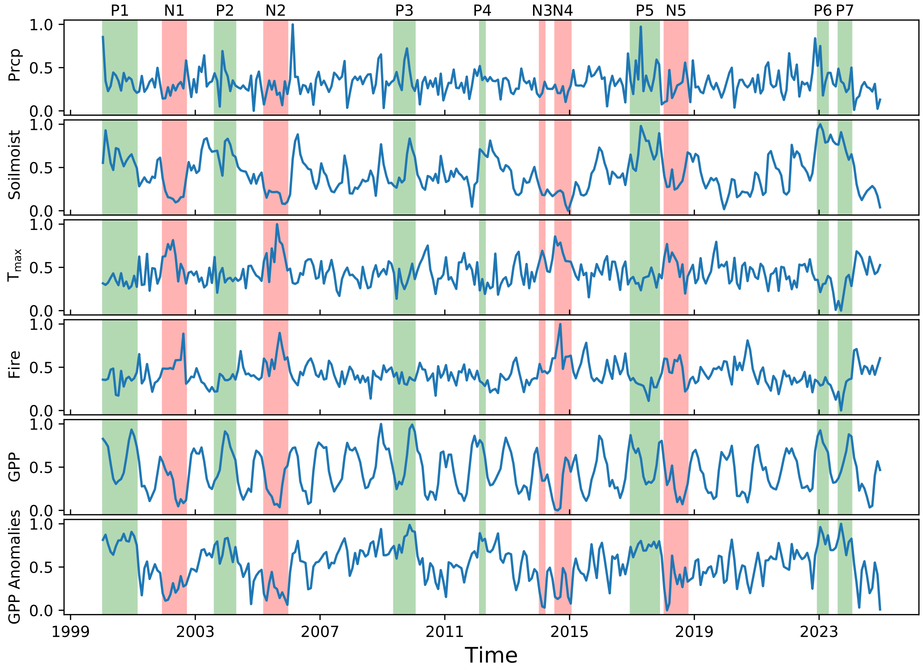

(a) *without LULCC*

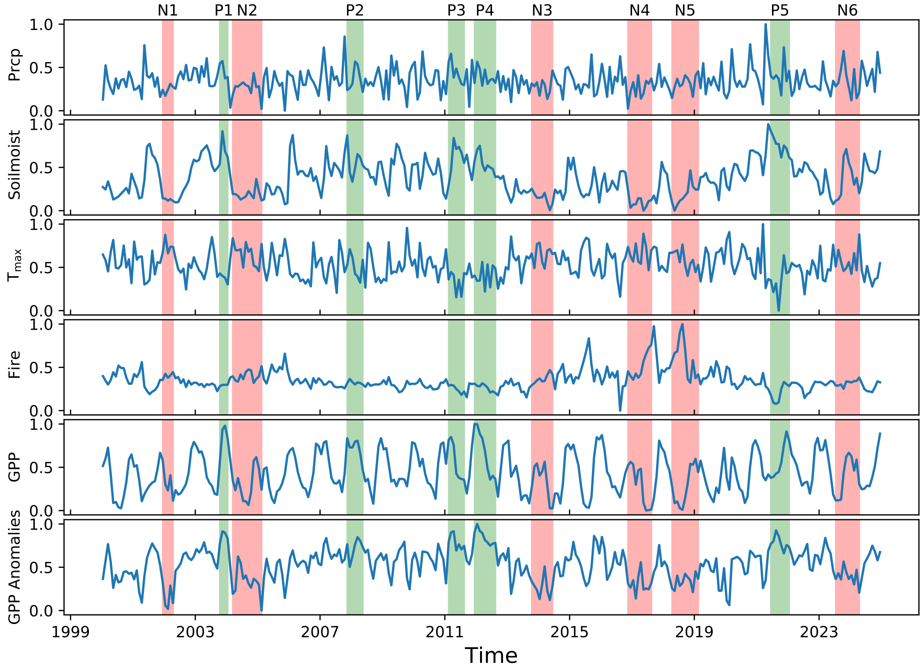

(b) *with LULCC*

Figure A11: Time series of normalized anomalies of climate drivers and GPP at Chaco Province, Argentina for (a) *without LULCC* and (b) *with LULCC* during 2000–24. The shaded areas in green color span over the positive TCEs ((a): P1 to P7 and (b): P1 to P5). Similarly, the areas in red color represents the negative GPP TCEs ((a): N1 to N5 and (b): N1 to N6).

Table A1: ILAMB score of the variables of CESM1(BGC)

Source: `https://www.ilamb.org/CMIP5/historical/`

| **Variable/Benchmark Data** | **IAV Score** | **Overall Score** |
|---|---|---|
| Surface Air Temperature/CRU | 0.821 | 0.782 |
| Diurnal Max Temperature/CRU | 0.793 | 0.752 |
| Precipitation/ GPCC | 0.793 | 0.651 |
| Terrestrial Water Storage Anomaly/GRACE | 0.905 | 0.588 |
| Burned Area/GFED4S | 0.447 | 0.409 |
| Evapotranspiration/MODIS | 0.617 | 0.588 |

Table A2: Details of GPP TCEs and PFT distribution at Chaco Province, Argentina. The results are shown for *without LULCC* and time window 2000–24. PFT refers to plant functional type, BDT is broadleaf deciduous tree, and BET is broadleaf evergreen tree.

| **TCE - neg** | **TCE - pos** | **TCE length - neg** | **TCE length - pos** | **TCE length - total** |
|---|---|---|---|---|
| 5 (events) | 7 (events) | 40 (months) | 53 (months) | 93 (months) |
| **PFT (I)** | **PFT(II)** | **PFT(III)** | **Latitude** | **Longitude** |
| BDT Temperate (43.2%) | BET Temperate (17.91%) | $C_3$ grass (17.48%) | 25.916° S | 300° E |

Table A3: Linear regression results for attribution analysis using the cumulative lagged effects for the region of Chaco Province, Argentina. The results are shown for *without LULCC* and time window 2000–24.

| | Fire | | $P - E$ | | Precipitation | | Soil Moisture | | $T_{\mathrm{max}}$ | | $T_{\mathrm{min}}$ | | $T_{\mathrm{sa}}$ | |
|---|---|---|---|---|---|---|---|---|---|---|---|---|---|---|
| **Lags** | CC | PV | CC | PV | CC | PV | CC | PV | CC | PV | CC | PV | CC | PV |
| **1** | -0.65 | 1.76E-12 | 0.365 | 3.27E-04 | 0.557 | 6.56E-09 | 0.734 | 5.85E-17 | -0.677 | 8.89E-14 | -0.328 | 1.31E-03 | -0.576 | 1.54E-09 |
| **2** | -0.653 | 1.25E-12 | 0.479 | 1.16E-06 | 0.653 | 1.25E-12 | 0.678 | 8.61E-14 | -0.693 | 1.42E-14 | -0.35 | 5.86E-04 | -0.592 | 4.29E-10 |
| **3** | -0.647 | 2.44E-12 | 0.502 | 2.99E-07 | 0.669 | 2.24E-13 | 0.639 | 5.61E-12 | -0.676 | 1.02E-13 | -0.364 | 3.36E-04 | -0.585 | 7.16E-10 |
| **4** | -0.624 | 2.45E-11 | 0.4918 | 5.53E-07 | 0.673 | 1.50E-13 | 0.621 | 3.26E-11 | -0.674 | 1.37E-13 | -0.36 | 3.96E-04 | -0.584 | 7.97E-10 |

Table A4: Linear regression results for attribution to climate driver triggers (i.e. onset 25% of TCE length) and cumulative lagged effects for the region of Chaco Province, Argentina. The results are shown for *without LULCC* and time window 2000–24.

| | Fire | | $P - E$ | | Precipitation | | Soil Moisture | | $T_{\mathrm{max}}$ | | $T_{\mathrm{min}}$ | | $T_{\mathrm{sa}}$ | |
|---|---|---|---|---|---|---|---|---|---|---|---|---|---|---|
| **Lags** | CC | PV | CC | PV | CC | PV | CC | PV | CC | PV | CC | PV | CC | PV |
| **1** | -0.679 | 5.08E-05 | 0.557 | 1.68E-03 | 0.718 | 1.16E-05 | 0.609 | 4.49E-04 | -0.622 | 3.12E-04 | -0.331 | 7.93E-02 | -0.534 | 2.84E-03 |
| **2** | -0.602 | 5.50E-04 | 0.595 | 6.57E-04 | 0.697 | 2.71E-05 | 0.469 | 1.03E-02 | -0.597 | 6.32E-04 | -0.259 | 1.75E-01 | -0.494 | 6.49E-03 |
| **3** | -0.518 | 3.98E-03 | 0.569 | 1.29E-03 | 0.662 | 9.15E-05 | 0.361 | 5.46E-02 | -0.527 | 3.35E-03 | -0.207 | 2.81E-01 | -0.424 | 2.19E-02 |
| **4** | -0.377 | 4.39E-02 | 0.439 | 1.71E-02 | 0.605 | 5.11E-04 | 0.353 | 6.05E-02 | -0.479 | 8.51E-03 | -0.125 | 5.19E-01 | -0.36 | 5.53E-02 |

Table A5: Linear regression results for attribution to climate driver triggers (i.e. onset 25% of TCE length) and cumulative lagged effects for the region of Chaco Province, Argentina. The results are shown for the simulation *with LULCC* and time window 2000–24.

| | Fire | | $P-E$ | | Precipitation | | Soil Moisture | | $T_{\max}$ | | $T_{\min}$ | | $T_{\mathrm{sa}}$ | |
|---|---|---|---|---|---|---|---|---|---|---|---|---|---|---|
| **Lags** | CC | PV | CC | PV | CC | PV | CC | PV | CC | PV | CC | PV | CC | PV |
| **1** | -0.457 | 1.69E-02 | 0.574 | 1.74E-03 | 0.668 | 1.37E-04 | 0.549 | 3.00E-03 | -0.73 | 1.53E-05 | 0.062 | 7.57E-01 | -0.578 | 1.59E-03 |
| **2** | -0.353 | 7.12E-02 | 0.598 | 9.90E-04 | 0.614 | 6.47E-03 | 0.428 | 2.59E-02 | -0.581 | 1.49E-03 | 0.056 | 7.81E-01 | -0.418 | 2.90E-02 |
| **3** | -0.236 | 2.37E-01 | 0.502 | 7.60E-03 | 0.512 | 6.30E-03 | 0.376 | 5.33E-02 | -0.357 | 6.75E-02 | 0.108 | 5.92E-01 | -0.186 | 3.54E-01 |
| **4** | -0.2 | 3.16E-01 | 0.416 | 3.09E-02 | 0.454 | 1.73E-02 | 0.367 | 5.90E-02 | -0.293 | 1.38E-01 | 0.07 | 7.28E-01 | -0.12 | 5.50E-01 |

# Appendix B

# Supplemantary Information Chapter 3

**Contents:**

1. Sections B1
2. Figures B1 to B10
3. Table B1

## B1 Calculation of temperature sensitivity of NBP

The sensitivity of NBP flux to surface air temperature is calculated using linear regression method [94],

$$NBP_{detrended} = b_0 + b_1 . TAS_{detrended} + \epsilon \qquad \text{(B.1)}$$

where NBP$_{detrended}$ refers to the detrended monthly timeseries of NBP and TAS refers to the detrended monthly timeseries of surface air temperature. The regression coefficient b$_1$ represent the apparent sensitivity of NBP to TAS; b$_0$ is the fitted intercept; $\epsilon$ is the residue error in the linear regression. The sensitivities of tropical and high latitudinal regions, as shown in Figure 3.6, has been calculated for consequentive 10 years periods starting from 1850 to 2100. The detrended timeseries of NBP and TAS for every SREX region were calculated by calculating the difference of area weighted mean and 10 year moving average of respective variables. Positive temperature sensitivity to NBP signifies strengthening the impact of temperature on net biome carbon flux and vice versa.

Table B1: SREX Reference Regions

| Abreviation | Region's Full Name |
|---|---|
| ALA | Alaska/N.W. Canada |
| AMZ | Amazon |
| CAM | Central America/Mexico |
| CAS | Central Asia |
| CEU | Central Europe |
| CGI | Canada/Greenland/Iceland |
| CNA | Central North America |
| EAF | East Africa |
| EAS | East Asia |
| ENA | East North America |
| MED | South Europe/Mediterranean |
| NAS | North Asia |
| NAU | North Australia |
| NEB | North-East Brazil |
| NEU | North Europe |
| SAF | Southern Africa |
| SAH | Sahara |
| SAS | South Asia |
| SAU | South Australia/New Zealand |
| SEA | Southeast Asia |
| SSA | Southeastern South America |
| TIB | Tibetan Plateau |
| WAF | West Africa |
| WAS | West Asia |
| WNA | West North America |
| WSA | West Coast South America |

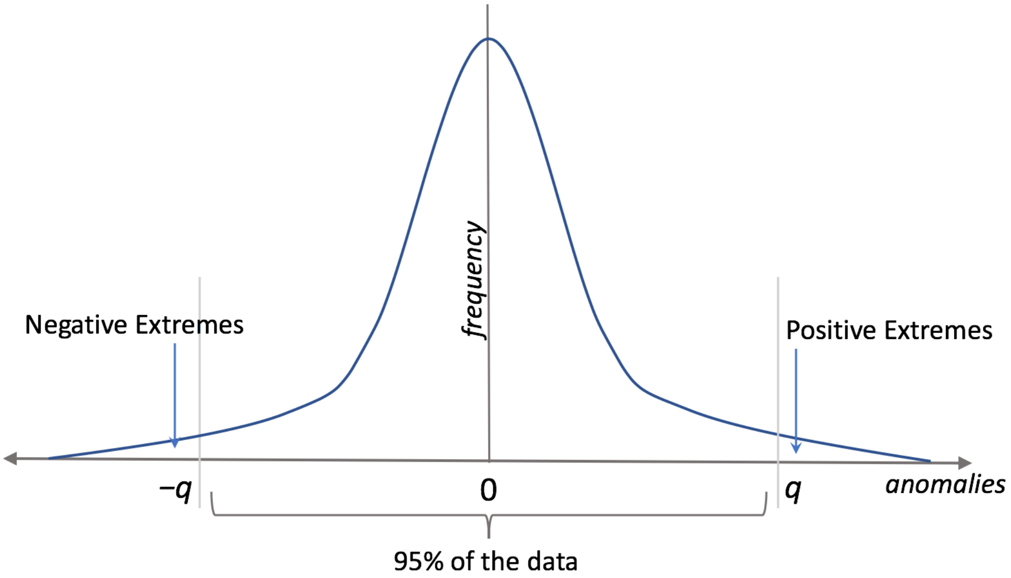

Figure B1: The schematic diagram representing the NBP extremes. The threshold $q$ is set at $5^{th}$ percentile in this study, such that 95% of the NBP anomalies lie within $-q$ and $q$.

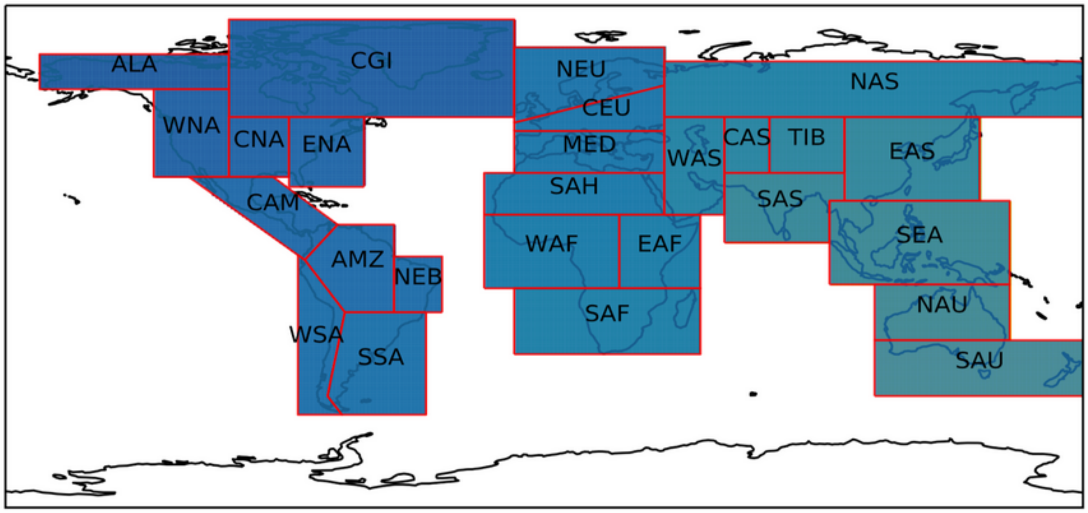

Figure B2: The spatial extent of SREX reference regions; abbreviations mentioned in the Table C1.

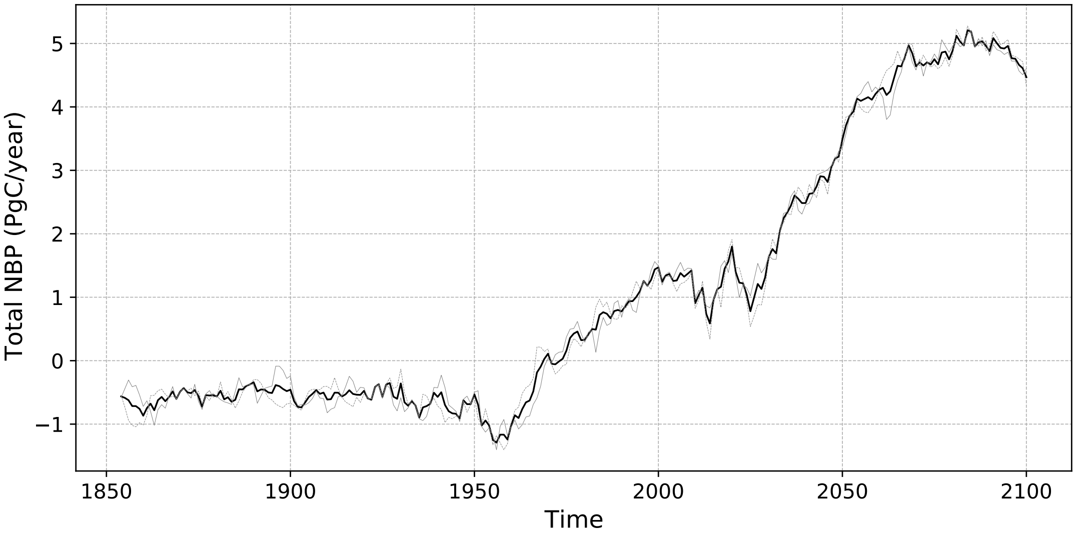

Figure B3: The timeseries of globally integrated 5 year rolling mean of NBP from 1850–2100 for CESM2 ensemble members is shown in gray dashed lines. The timeseries of globally integrated 5 year rolling mean of multi-ensemble mean is shown in black solid line.

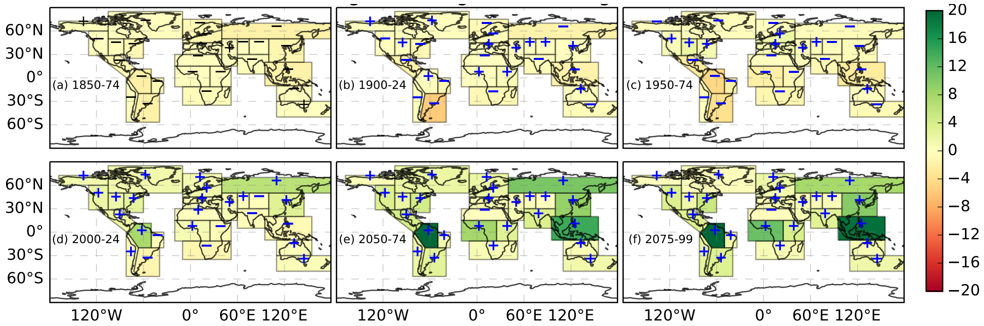

Figure B4: Total integrated NBP (PgC) for 25-year time windows for the period 1850–2100. Spatial distribution of integrated NBP (PgC) change over time: (a) 1850–74, (b) 1900–24, (c) 1950–74, (d) 2000-24, (e) 2050–74, and (f) 2075–99. Net increase in regional NBP or total carbon uptake is represented by green color and '+' sign; net decrease is represented by red color and '−' sign.

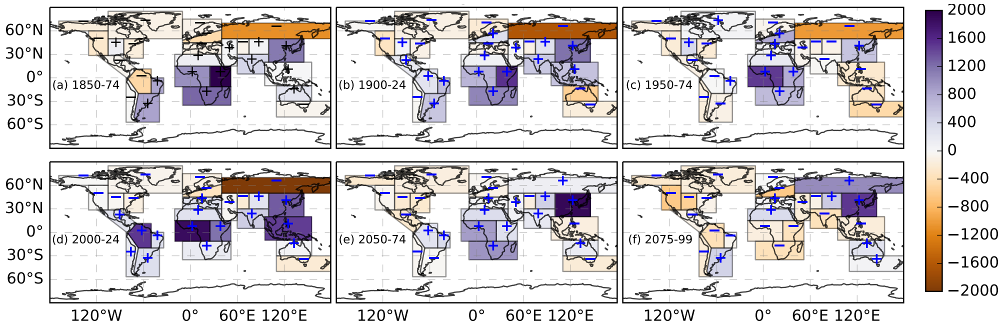

Figure B5: Frequency of positive $vs$ negative NBP extreme events across SREX regions. Purple color ('+' sign) highlights the regions where frequency of positive NBP extremes events exceed negative NBP extremes; and brown color ('−' sign) identifies regions where frequency of negative NBP extreme events exceed positive NBP extremes. Towards the end of 21st century, most tropical regions are dominated by frequent negative NBP extremes.

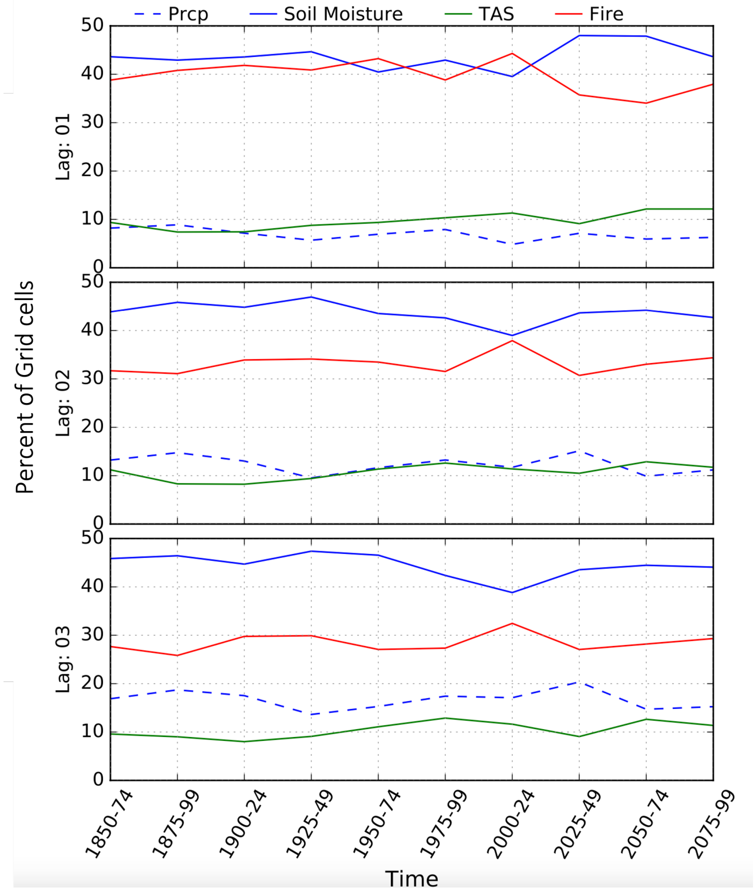

Figure B6: Percent distribution of number of grid cells with dominant climate drivers causing time continuous carbon cycle extremes from 1850 to 2100 for every 25-year period. The dominance of climate drivers is estimated by the absolute magnitude of correlation coefficient ($p < 0.05$) at lags of 1 (*top*), 2 (*middle*), and 3 (*bottom*) months.

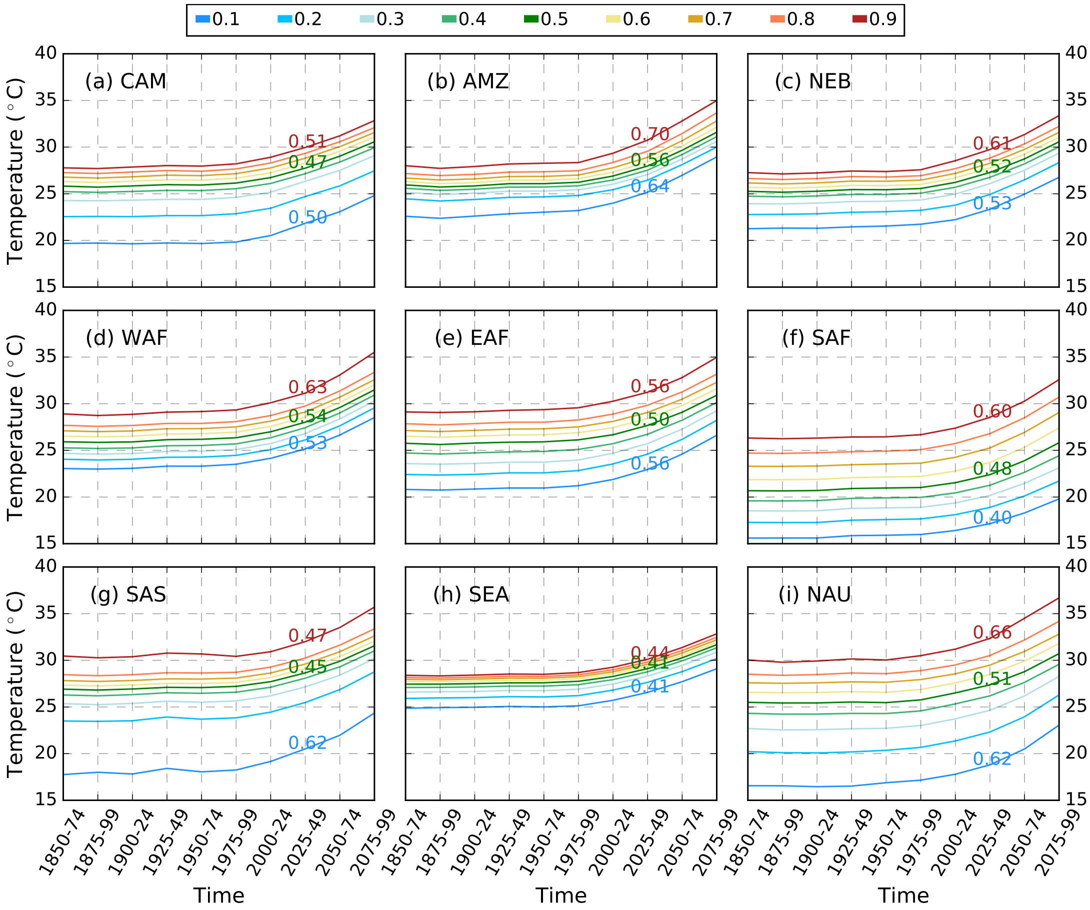

Figure B7: Change in area weighted average surface temperature (TAS) at various quantiles in the 9 SREX regions in tropics for 25-year windows from 1850–2100. The numbers shown in maroon, green, and blue in each subplot represent the rate of increase of temperature per decade (°C/decade) for $90^{th}$, median, and $10^{th}$ quantile of temperatures, respectively.

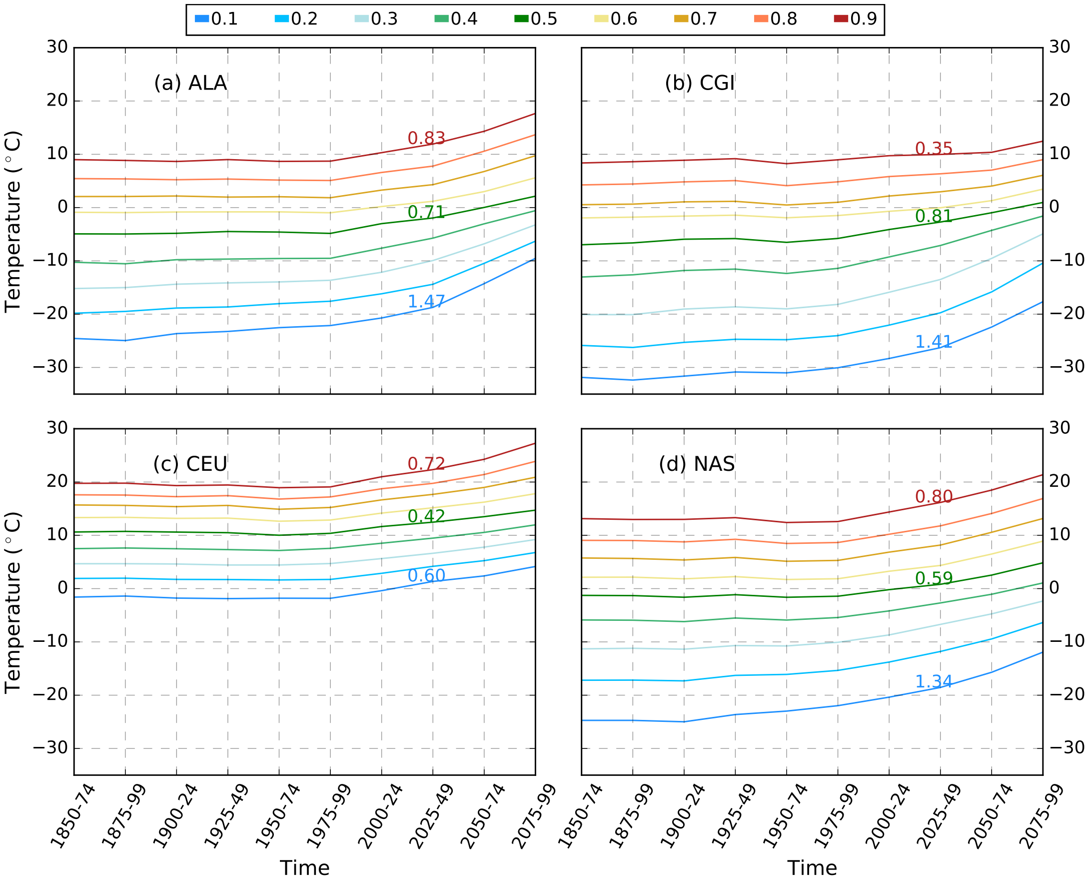

Figure B8: Change in area weighted average surface temperature (TAS) at various quantiles in the 9 SREX regions at high latitudes for 25-year windows from 1850–2100. The numbers shown in maroon, green, and blue in each subplot represent the rate of increase of temperature per decade (°C/decade) for $90^{th}$, median, and $10^{th}$ quantile of temperatures, respectively.

Figure B9: Timeseries of total carbon fluxes for the regions of (a) Central America/Mexico (CAM), (b) Amazon(AMZ), (c) North-East Brazil (NEB), (d) West Africa (WAF),(e) East Africa (EAF), (f) Southern Africa (SAF), (g) South Asia (SAS), (h) Southeast Asia (SEA), and (i) North Australia (NAU) . Row 1 for each region shows the time series of total GPP (left y-axis) and NPP (right y-axis). Row 2 shows RA and RH on left y-axis and fFireAll on right y-axis. Row 3 shows NEP, NBP on left y-axis and −NEE on right y-axis. NEP is calculated by subtracting RH from NPP. NEP is surface net downward mass flux of carbon dioxide expressed as carbon due to all land processes excluding anthropogenic land use change. −NEE has the consistent direction with the carbon flux such as NBP and NPP.

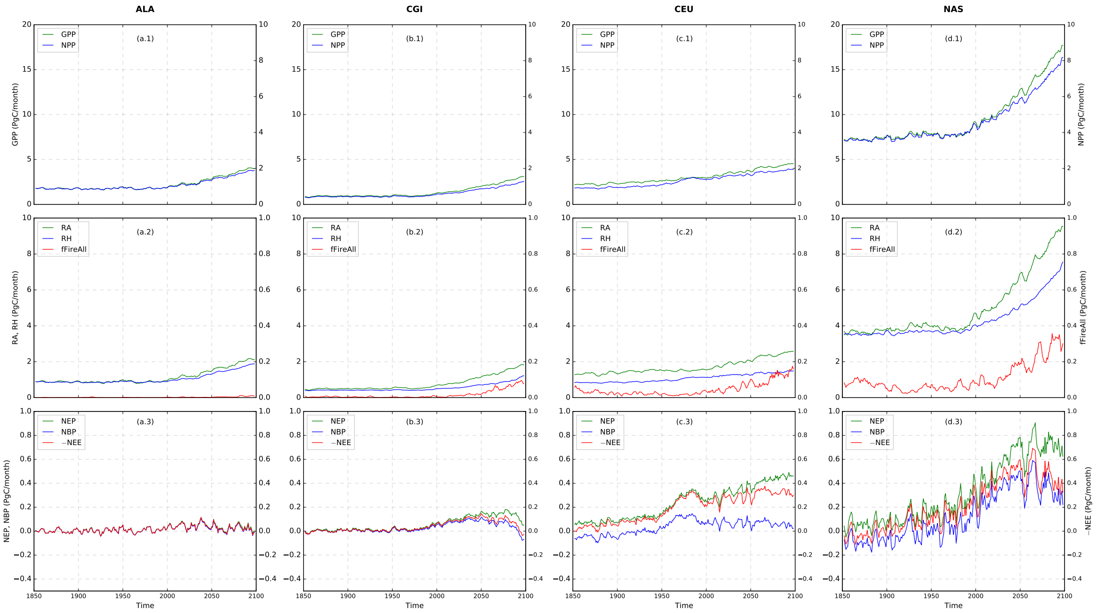

Figure B10: Timeseries of total carbon fluxes for the regions of (a) Alaska, (b) Canada, Greenland, and Iceland, (c) Central Europe, and (d) Northern Asia (NAS). Row 1 of every region shows the time series of total GPP (left y-axis) and NPP (right y-axis). Row 2 shows RA and RH on left y-axis and fFireAll on right y-axis. Row 3 shows NEP, NBP on left y-axis and −NEE on right y-axis. NEP is calculated by subtracting RH from NPP. NEP is surface net downward mass flux of carbon dioxide expressed as carbon due to all land processes excluding anthropogenic land use change. −NEE has the consistent direction with the carbon flux such as NBP and NPP.

# Appendix C

# Supplemantary Information Chapter 4

**Contents:**

1. Figures C1 to C11
2. Tables C1 to C3

Table C1: SREX Reference Regions

| Abreviation | Region's Full Name |
|---|---|
| ALA | Alaska/N.W. Canada |
| AMZ | Amazon |
| CAM | Central America/Mexico |
| CAS | Central Asia |
| CEU | Central Europe |
| CGI | Canada/Greenland/Iceland |
| CNA | Central North America |
| EAF | East Africa |
| EAS | East Asia |
| ENA | East North America |
| MED | South Europe/Mediterranean |
| NAS | North Asia |
| NAU | North Australia |
| NEB | North-East Brazil |
| NEU | North Europe |
| SAF | Southern Africa |
| SAH | Sahara |
| SAS | South Asia |
| SAU | South Australia/New Zealand |
| SEA | Southeast Asia |
| SSA | Southeastern South America |
| TIB | Tibetan Plateau |
| WAF | West Africa |
| WAS | West Asia |
| WNA | West North America |
| WSA | West Coast South America |

The mean GPP of observations for the period of 2001-13 are (Figure C5):

- GOSIF: 137.68 PgC/year
- FluxSat: 140.45 PgC/year
- FluxAnn: 114.87 PgC/year
- WECANN: 117.01 PgC/year
- FluxRS: 121.69 PgC/year
- FluxRSMeteo: 132.97 PgC/year

Table C2: Observation GPP Datasets

| Abbreviation | Product Name | #Lat × #Lon | Time |
|---|---|---|---|
| FluxRS[1] | FLUXCOM-RS | 360 × 720 | 1-2001 to 12-2015 |
| FluxRSMeteo[2] | FLUXCOM-RS+METEO | 360 × 720 | 1-2001 to 12-2010 |
| FluxAnn[3,*] | FLUXCOM | 360 × 720 | 1-1980 to 12-2013 |
| GOSIF[4,*] | GOSIF | 3600 × 7200 | 3-2000 to 12-2020 |
| FluxSat[5,*] | FluxSat v2.0 | 3600 × 7200 | 3-2000 to 7-2020 |
| WECANN[6] | WECANN | 180 × 360 | 1-2007 to 12-2015 |

[1] GPP estimates from remote sensing (MODIS) only

[2] GPP estimates from remote sensing (MODIS) and meteorological forcing

[3] GPP based on FLUXCOM RS+METEO with CRUNCEPv6 climate using Artificial Neural Network.

[4] GPP derived from OCO-2 Solar-induced chlorophyll fluorescence (SIF)

[5] GPP derived from global MODIS and FLUXNET

[6] Water, Energy, and Carbon with Artificial Neural Networks (WECANN): Estimate of GPP using SIF.

[*] Used for comparison of carbon cycle extremes with models, for details refer to *Methods* section.

Table C3: CMIP6 Models' Data Details

| Product Name | #Lat × #Lon |
|---|---|
| BCC-CSM2-MR | 160 × 320 |
| CanESM5 | 64 × 128 |
| CESM2 | 192 × 288 |
| CNRM-CM6-1 | 128 × 256 |
| CNRM-ESM2-1 | 128 × 256 |
| IPSL-CM6A-LR | 143 × 144 |
| MPI-ESM1-2-HR | 96 × 192 |
| MPI-ESM1-2-LR | 192 × 384 |
| NorESM2-LM | 96 × 144 |

All the CMIP6 Earth System Models are fully coupled.
Downloaded from: https://esgf-node.llnl.gov/search/cmip6/

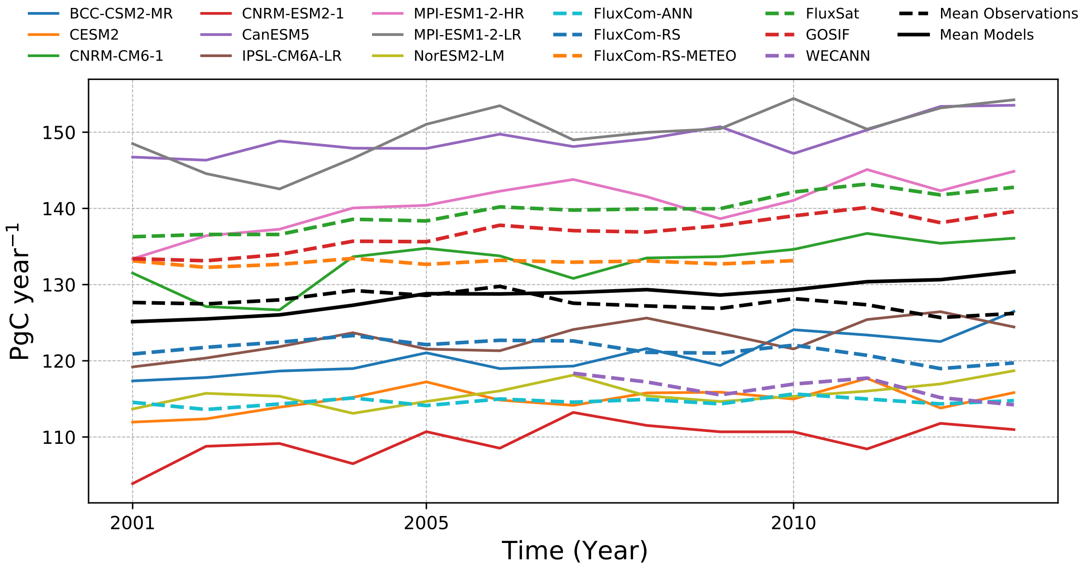

Figure C1: Timeseries of the integrated yearly GPP from the year 2001 to 2013 of observations and models. The observations and models are represented in dashed and solid lines respectively. For this period, observation yielded GPP estimates of 127 ± 10.8 PgC/year which are within the estimates of models, i.e. 128.5 ± 15.2 PgC/year.

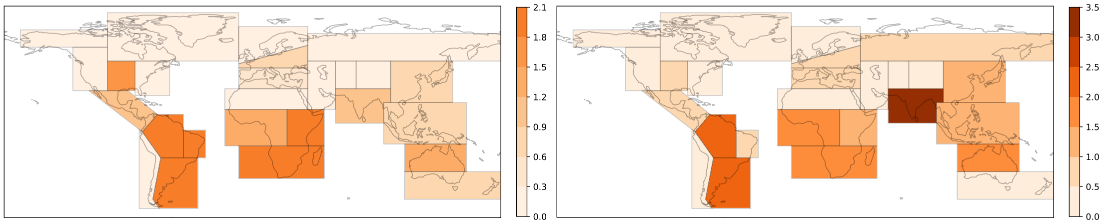

(a) SD Observations (b) SD Models

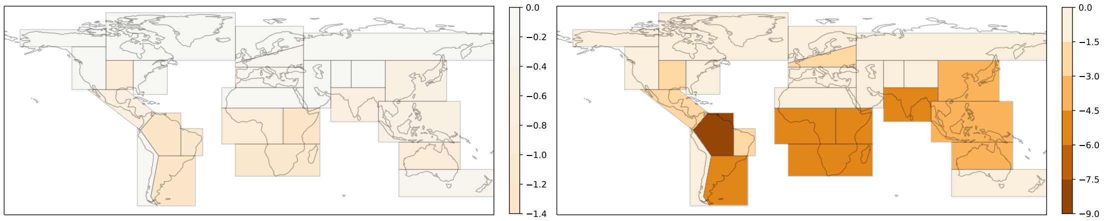

(c) Mean Observations (d) Mean Models

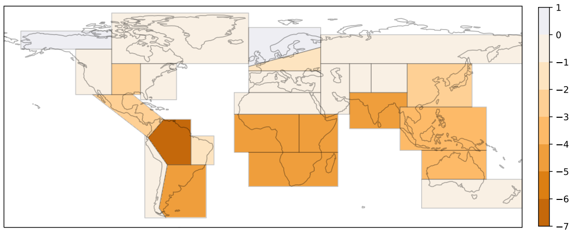

(e) Mean Models−Observations

Figure C2: Spatial distribution of the magnitude of negative carbon cycle extremes from top 50 percent of grid cells experiencing most of the negative extremes. The colors of standard deviation of magnitude of negative GPP extremes of observations (a) and models (b) ranges from 0 to 3.5 PgC/month. The colors of mean magnitude of negative GPP extremes of observations (c), models (d), and models−observation ranges from −9 to 9 PgC/month.

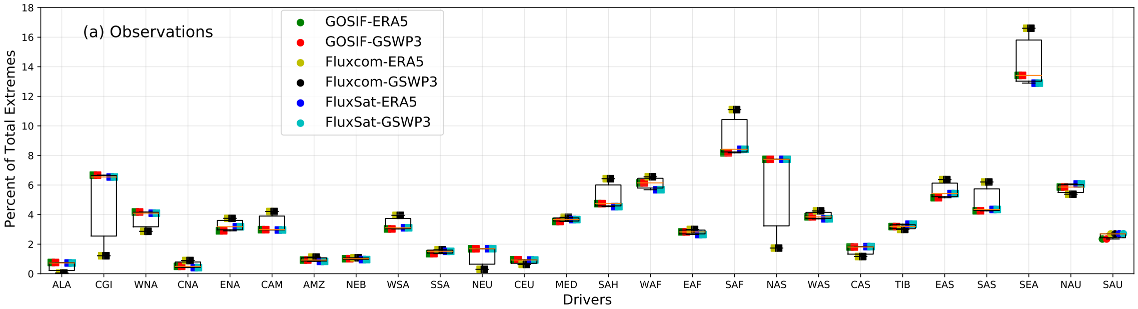

(a) Count of Negative Carbon Extremes of Observations

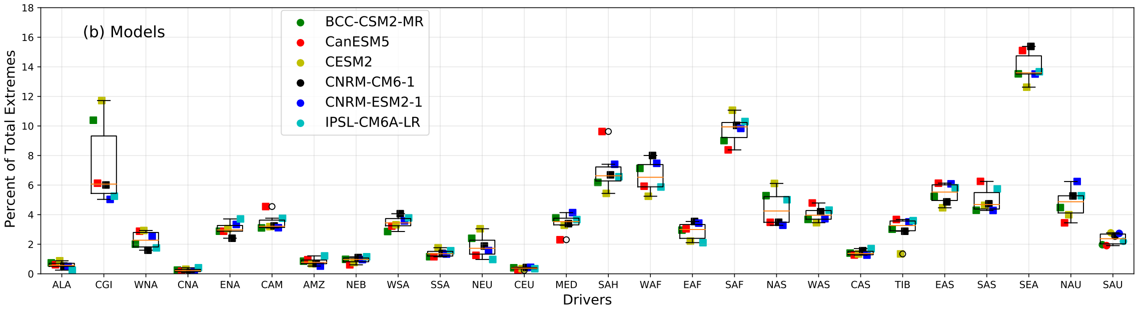

(b) Count of Negative Carbon Extremes of Models

Figure C3: Spatial distribution of percent count of negative carbon cycle extremes. The box plots of percent count of negative carbon cycle extremes of observations (a) and models (b).

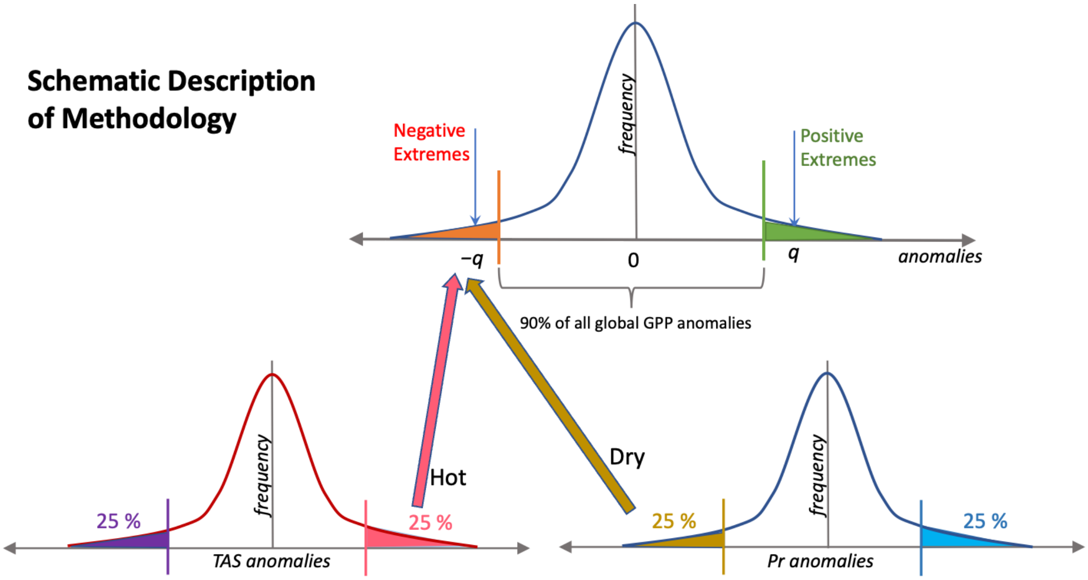

$med_{pr\_du\_ext} < pr_{q25}$ : carbon cycle extremes driven by dry conditions,

$med_{tas\_du\_ext} > tas_{q75}$ : carbon cycle extremes driven by hot condition,

$med_{pr\_du\_ext} < pr_{q25}$ & $med_{tas\_du\_ext} > tas_{q75}$ : carbon cycle extremes driven by compound effect of hot and dry conditions.

Figure C4: Schematic diagram of detection of GPP extremes and attribution to climate drivers. The shape of the plots is made Gaussian for illustration purposes only.

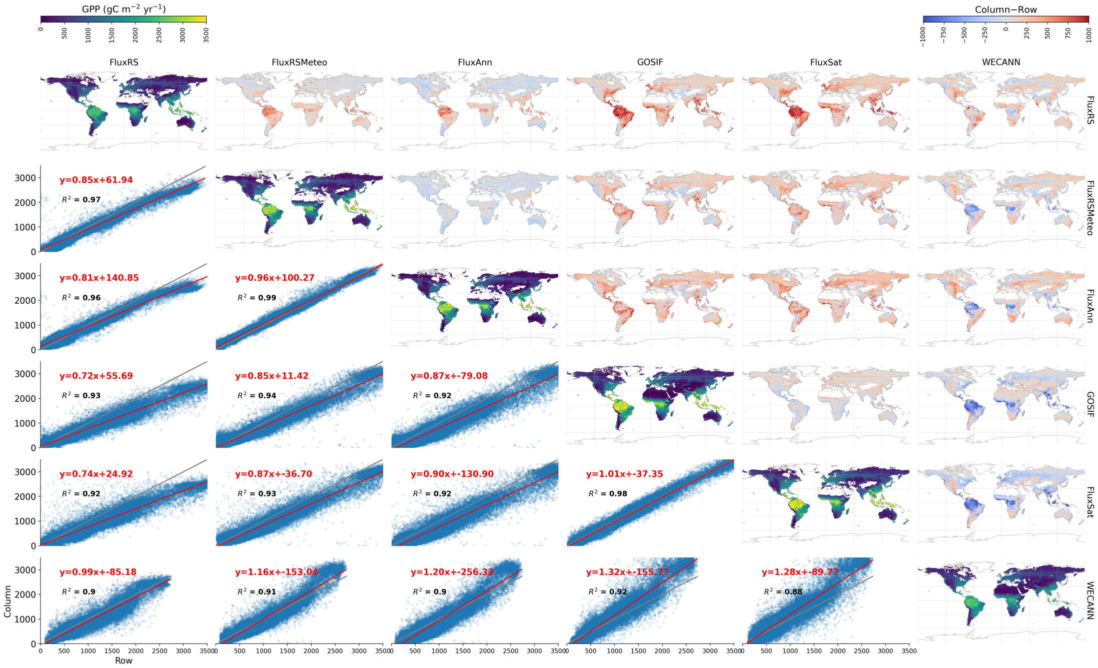

Figure C5: Comparison of mean annual GPP at 0.5° spatial resolution for the period 2007–2010 among observations. From left to right and top to bottom the order of observation datasets are FluxRS, FluxRSMeteo, FluxANN, GOSIF, FluxSat, and WECANN. The diagonal maps show the mean annual GPP of every dataset. Maps above the diagonal show the difference of the GPP of column dataset − row dataset. The plots below the diagonal show the point density in blue and 1:1 regression line in grey. Red line and equation represent the best fit line from total least-squares regression.

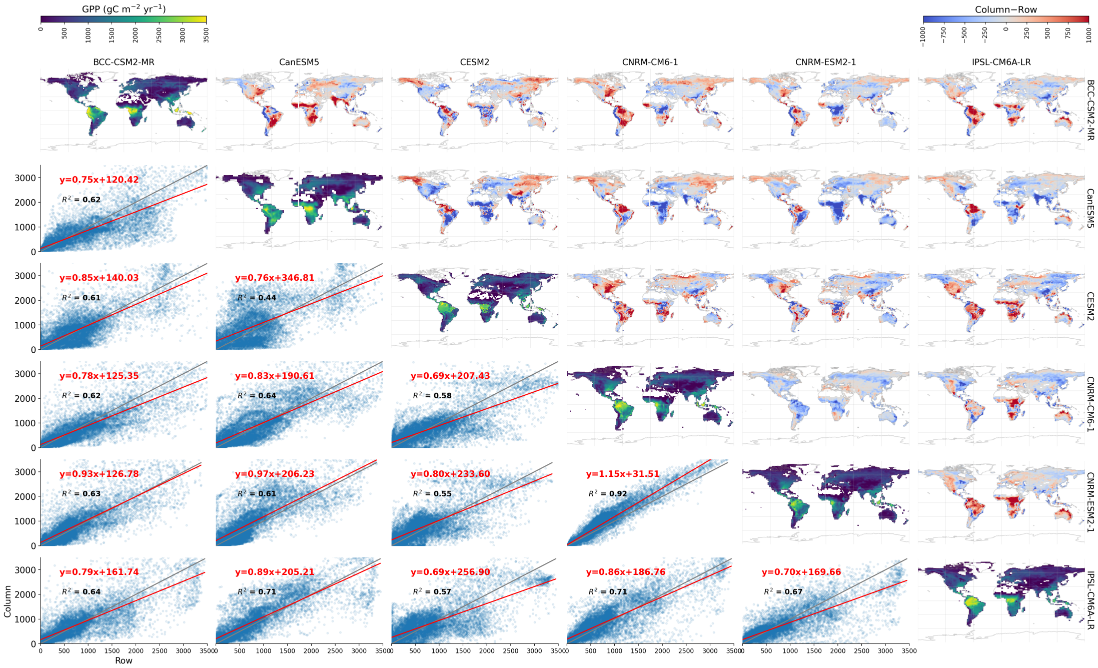

Figure C6: Comparison of mean annual GPP at 0.5° spatial resolution for the period 2007–2010 among CMIP6 models. From left to right and top to bottom the order of models are BCC-CSM2-MR, CanESM5, CESM2, CNRM-CM6-1, CNRM-ESM2-1, and IPSL-CM6A-LR. The diagonal maps show the mean annual GPP of every dataset. Maps above the diagonal show the difference of the GPP of column dataset − row dataset. The plots below the diagonal show the point density in blue and 1:1 regression line in grey. Red line and equation represent the best fit line from total least-squares regression.

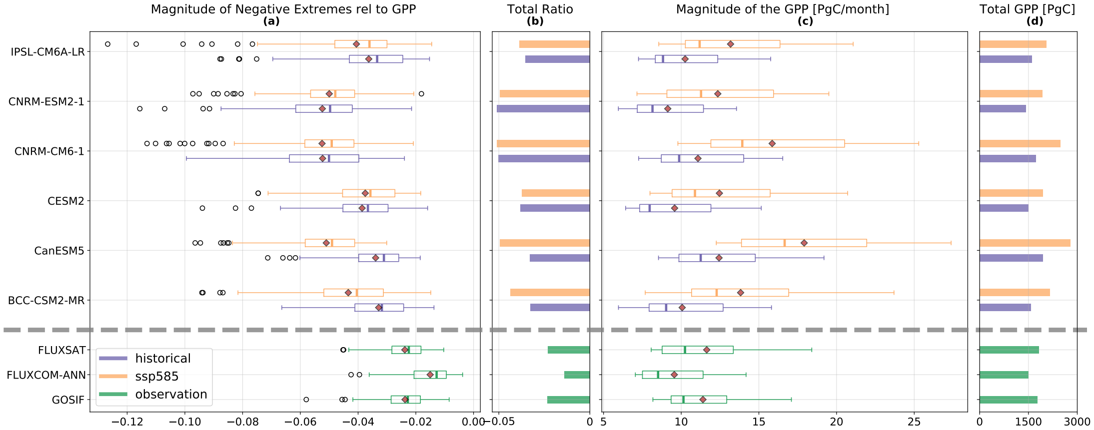

Figure C7: The green, purple, and orange colors represent the statistics explained below for observation data (2001–13), historical model simulations (2001–13), and SSP585 model simulations (2061–73), respectively. Box plot of ratios of the monthly magnitude of negative carbon cycle extremes to total monthly GPP (a) and total monthly GPP (c) of observation data and model simulations. Ratio of total negative magnitude of negative extremes to to total GPP (b) and total GPP (d). The grey dashed line separates observations and models. Ratio of magnitude of negative extremes to total GPP is referred as $L/GPP$ (ratio) in the paper, which means loss in expected carbon uptake to total GPP. The negative extremes in GPP are calculated using same threshold as historical period.

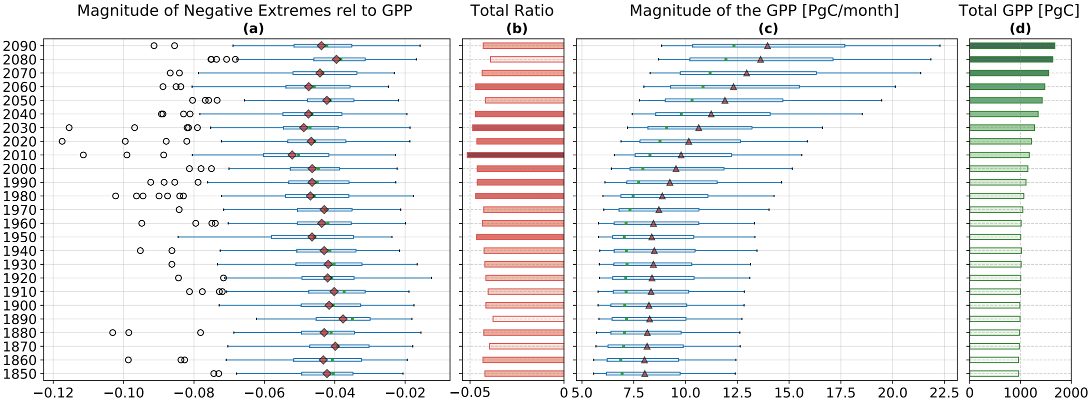

Figure C8: Decadal change in GPP and ratio of negative carbon cycle extremes to GPP ($L : GPP$) for the CESM2. The negative extremes are calculated with respect the extremes of the period 1850–60.

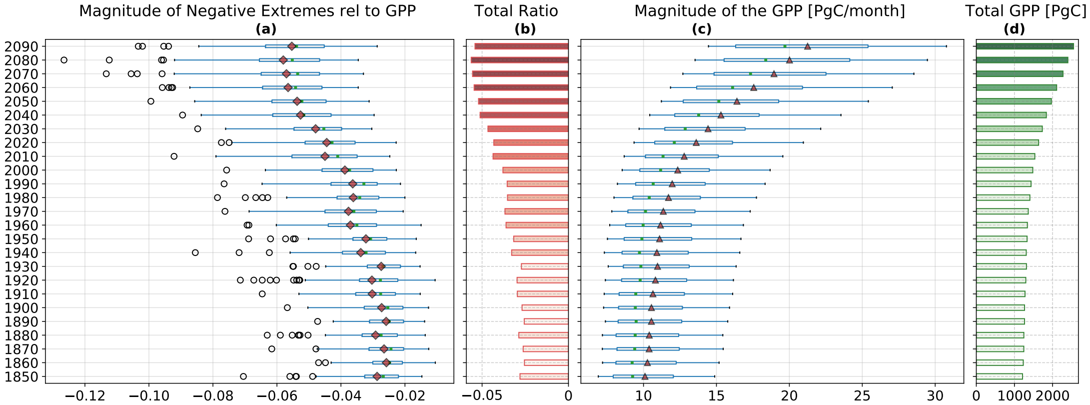

Figure C9: Decadal change in GPP and ratio of negative carbon cycle extremes to GPP ($L : GPP$) for the CanESM5. The negative extremes are calculated with respect the extremes of the period 1850–60.

Figure C7 represents the change in the $L : GPP$ for the period 2081–93 relative to the period 2001–13. It shows that the increase in negative carbon cycle extremes grow at least in proportion to increase in GPP (e.g. CESM2 and CNRM-ESM2-1 as $L : GPP$ remains similar) relative to period 2001–13 (Figure C7) or increase at a higher rate (more than 20% for other models) with respect to total change in GPP.

While the change in mean and maximum $L : GPP$ ratio per decade is similar for all models, the patterns are very different of models CESM2 and CNRM-ESM2-1 and other models. The decadal change in $L : GPP$ ratio has in increasing trend from 1850 to 2020 followed by a slight reduction till 2100. Hence the overall increase in negative carbon cycle extremes in CESM2 is proportional to increase in GPP (Figure C8). However, CanESM5 shows the increase of negative carbon cycle extremes at a rate higher than the rate of increase of GPP (Figure C9), which implied the expected losses in CanESM5 is accelerating over time.

Figure C10: Shows that the negative extremes are driven mostly by dry and hot events.

Figure C11 shows that as the dominance of dry climate conditions increases in driving negative carbon cycle extremes, especially when pr-tas attribution is analyzed. The attribution to climate drivers is exclusive.

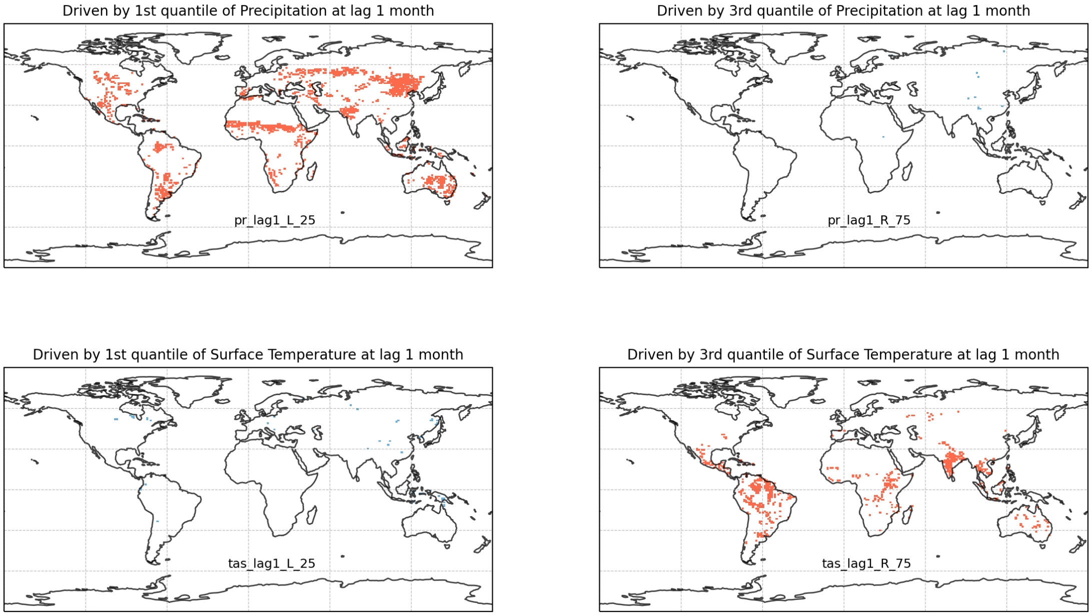

Driven by 1st quantile of Precipitation at lag 1 month

Driven by 3rd quantile of Precipitation at lag 1 month

Driven by 1st quantile of Surface Temperature at lag 1 month

Driven by 3rd quantile of Surface Temperature at lag 1 month

Figure C10: Spatial distribution of climate drivers, precipitation and surface temperature, causing negative carbon cycle extremes in CESM2 model at lag of 1 month.

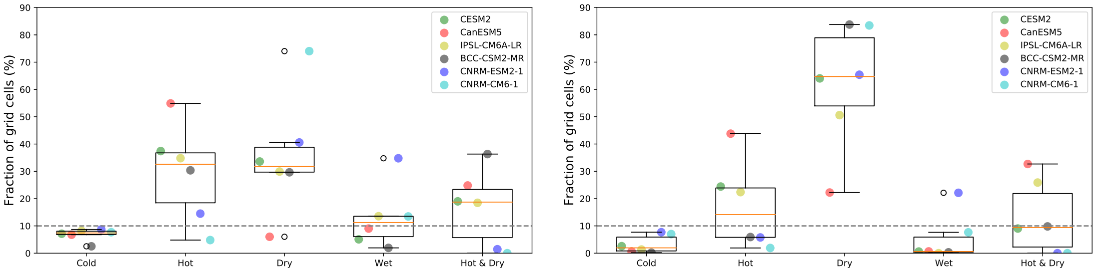

(a) Pr-TAS, no-lag (b) Pr-TAS, 1 month lag

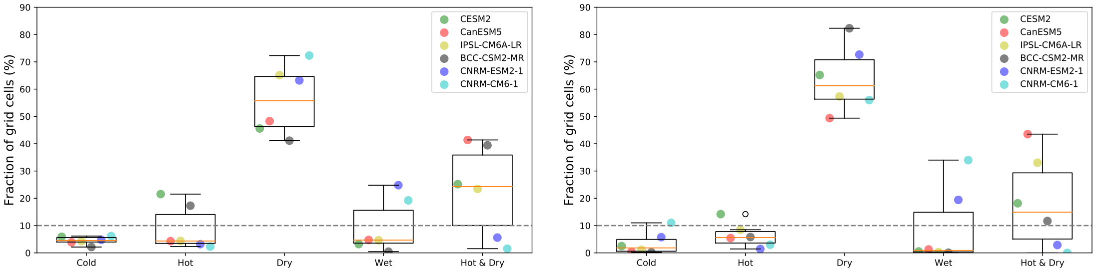

(c) SM-TAS, no-lag (d) SM-TAS, 1 month lag

Figure C11: Attribution of negative carbon cycle extremes to precipitation and soil moisture at no-lag and 1-month lag, exclusively. Left panel shows no-lag and right panel shows lag 1. top shows pr-tas attribution bottom shows sm-tas attr. Cold and wet conditions rarely drive a negative carbon cycle extreme event as they lie below the horizontal dashed line at 10%.

## Open Research

### Data Availability Statement

The CESM1(BGC) model output used for detection and attribution of carbon cycle extremes in the study are available at https://doi.org/10.5281/zenodo.5548153. The selected variables from CESM2 were downloaded from ESGF using the link: https://esgf-node.llnl.gov/projects/esgf-llnl/. The details of the data used in Chapter 4 is mentioned in Section 4.2. Data analysis was performed in Python, and all analysis codes are publicly available on GitHub at https://github.com/sharma-bharat/Codes_Carbon_Extremes_2300 and archieved at https://doi.org/10.5281/zenodo.6147120. The analysis codes will be available on GitHub at https://github.com/sharma-bharat/Codes_NBP_Extremes and at https://github.com/sharma-bharat/Sharma_Codes_Multimodel_Obs upon acceptance of manuscript for Chapter 3 and Chapter 4, respectively.